Modeling the Electrohydrodynamics of Three-Dimensional Vesicles

Mohammad Ebrahim Kolahdouz

February 2015

A Dissertation submitted to the
Faculty of the Graduate School of
the University at Buffalo, State University of New York
in partial fulfillment of the requirements for the
degree of
Doctor of Philosophy

Department of Mechanical & Aerospace Engineering

UMI Number: 3683048

UMI

Dissertation Publishing

UMI 3683048

ProQuest®

Abstract

In this work a numerical method is presented to model the electrohydrodynamics of a three-dimensional vesicle. The objective of this study is to develop robust numerical algorithms to solve the physical governing equations of the vesicle in the presence of fluid flow and DC electric fields. Furthermore the model will be able to predict the fast dynamics of the vesicle exposed to strong fields for a wide range of material properties and deformations that cannot be easily captured in experimental settings.

The vesicle membrane is modeled as an infinitesimally thin capacitive interface. The electric field calculations explicitly take into account the capacitive interface by an implicit Immersed Interface Method formulation, which computes the electric potential field and the trans-membrane potential simultaneously. The interface is tracked through the use of a semi-implicit, gradient-augmented level set method. The enclosed volume and surface area are conserved both locally and globally by a new Navier-Stokes projection method.

The valdiation of the hydrodynamic model was examined in the light of experimental data and observations. The two major modes of the vesicle motion in the linear shear flow namely the tank-treading and tumbling regimes, were studied. Simulation results show a very good agreement between the present results and the experimental data.

The electrohydrodynamic results also match well with previously published experimental, analytic and two-dimensional computational works and the model is capable of capturing the type of topological changes previously observed in experiments. A parameter study of different important material properties is carried out for the transition between oblate and prolate ellipsoidal shapes in order to estimate the critical parameter tresholds for this transition to happen. In addition, investigation of the vesicle behavior under the combined effects of shear flow and weak DC electric fields

reveals the remarkable influence of the electric field in changing the standard behaviors of tank-treading and tumbling vesicles. If the electric field is strong enough the induced resistance caused by the electric field may alter the behavior of a tumbling vesicle into a tank-treading motion.

This research is a step in the path to understand the complex physics of multi-component lipid membranes and predict more challenging interfacial phenomena such as electroporation in the context of their biological applications.

Acknowledgements

First and foremost, I would like to express my sincere appreciation to my Ph.D. advisor, Dr. David Salac for his invaluable help and support during my research. I would also like to thank Professors Paul DesJardin and Susan Hua for sitting on my dissertation committee and taking the time to go through this dissertation. I also take this occasion to thank Dr. Jae-Hun Jung from Department of Mathematics for the useful discussions I had with him.

Lastly, my sincere thanks and gratitude go to my beloved parents, brothers and sisters for their unwavering support at every stage of my life. Without them, my accomplishments would not be possible.

To my parents.

Contents

List of Tables

List of Figures

Chapter 1

Introduction and Motivation

Biological cells act as the basic structural unit of most living creatures and it is obvious to focus on understanding the behavior of cell when trying to understand the function and properties of organisms. In studying the cell the membrane is perhaps the most essential component. For example, it plays a critical rule in regulating the transport of molecules in and out of cells. In general, the cell membrane is not a simple homogeneous interface. It is normally composed of lipid molecules, proteins, cholesterol and ion channels. A schematic of cellular membrane is depicted in Fig. 1.1. Despite the apparent complex structure, studies show the double-layer of lipid molecules is the most primary element of the membrane and occupies over 50% of the mass in the membrane of eukaryotic cells (cells with nucleus) [5].

Giant unilamellar vesicles are enclosed bag-like membranes solely composed of the above-mentioned lipid bilayers. Hence they form a basic model for actual biological cells. It is quite easy to artificially create these soft particles in a laboratory setting. In an aqueous solution, the two-dimensional phospholipid bilayer sheets fold and curve in three-dimensional space and self-assemble into a fluid-filled vesicle due to their strong tendency to minimize the free energy [39] (Fig. 1.2). This behavior is attributed to the amphipathic nature of phospholipids. A single phospholipid consists
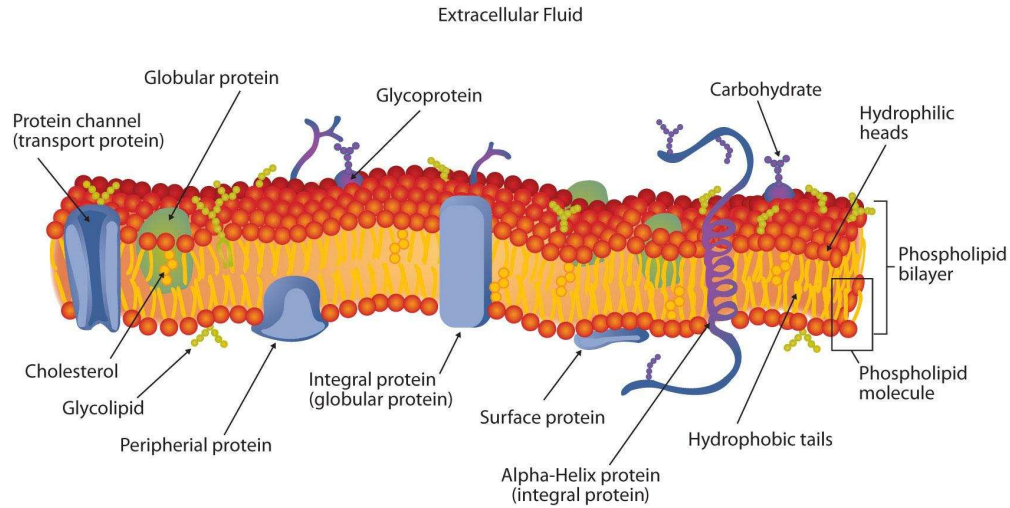
Figure 1.1: The schematic of the cell membrane

of a hydrophilic (or water-loving) phosphate head group, and a hydrophobic (or water hating) fatty-acid tail. The amphipathic nature of phospholipids basically means that the phospholipids arrange themselves into a bilayer, with hydrophobic tails on the inside and hydrophilic heads on the outside.

Vesicles share remarkable similarities in composition and size with other biological cells such as red blood cells. Experimental observations have demonstrated that lipid vesicles exhibit a striking resemblance to more complicated biological cells in terms of their equilibrium shapes and non-equilibrium behavior in various fluid conditions [2, 97]. All of these properties make the vesicle a robust model system to mimic the behavior of more complicated non-nucleated biological cells. Aside from the important insight studying vesicles provides in understanding the rheology of biofluids and biological cells, lipid vesicles of organic and artificial kinds have been also proposed in various biomedical technologies such as directed drug and gene delivery [6, 26] or biological microreactions [59, 17].

For all the above-mentioned reasons, the study of lipid vesicles has gained great attention in the past two decades. Particularly, the interaction of vesicles with exter-
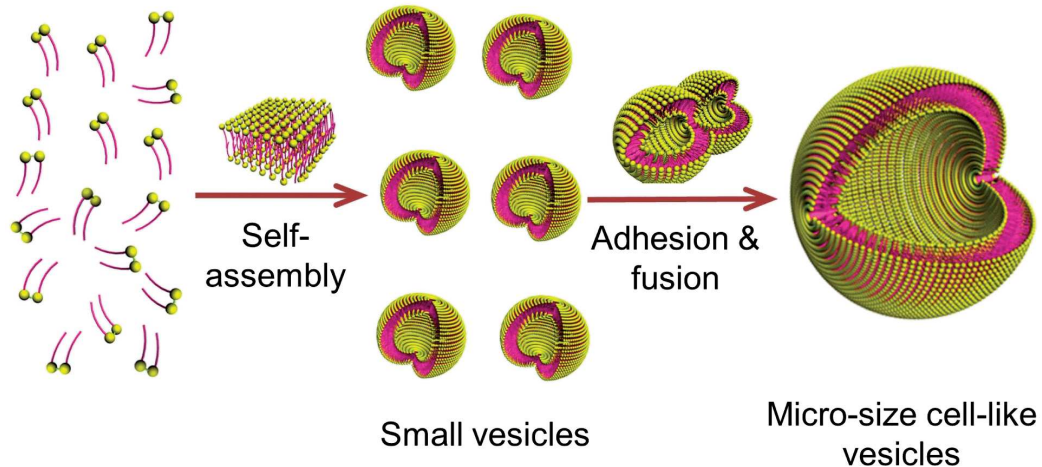
Figure 1.2: Self assembly of the phospholipid bilayers into a cell-like vesicle.

nal flows has been of major interest. The dynamics of the vesicle is determined as a result of competition between the hydrodynamic forces of the fluid and the bending and tension forces of the vesicle membrane. In shear flow, these topological changes depend on three major parameters: the viscosity ratio between the enclosed and surrounding fluids, the imposed shear rate and the reduced volume defined as the ratio of the volume of the vesicle to the volume of sphere with the same surface area as the vesicle [8]. The most well-known regimes in shear flow are tank-treading, tumbling and a transient state called trembling or vacillating breathing [51, 28]. Tank-treading happens when the viscosity ratio between the interior and exterior fluids is below a critical value. The vesicle then reaches an equilibrium inclination angle with respect to the flow direction and stays at that position permanently (Fig 1.3(a)). A viscosity ratio above the critical viscosity ratio results in a change in behavior, from tank-treading to tumbling in which the vesicle undergoes a periodic flipping motion (Fig 1.3(b)). Trembling is an unsteady state between the tank-treading and tumbling regions in which the vesicle undergoes large oscillations while doing trembling-like motion around the flow direction (Fig 1.3(c)). These behaviors have been extensively studied in both theory [24, 41, 55, 83, 95] and experiments [1, 18, 28]. Also, several

numerical simulations have appeared in the literature. Among the numerical studies in two dimensions are modelings using the boundary integral method [8, 93], phase field approach [9, 52, 4], coupled level set and projection method [72, 74], coupled level set and finite-element method [21, 36] and lattice Boltzmann method [29]. A few three-dimensional studies have been also reported using phase-field approach [11], boundary integral method [10, 104, 94] and front-tracking method [101].

(a) Tank-treading [27]

(b) Tumbling [28]

(c) Trembling [28]
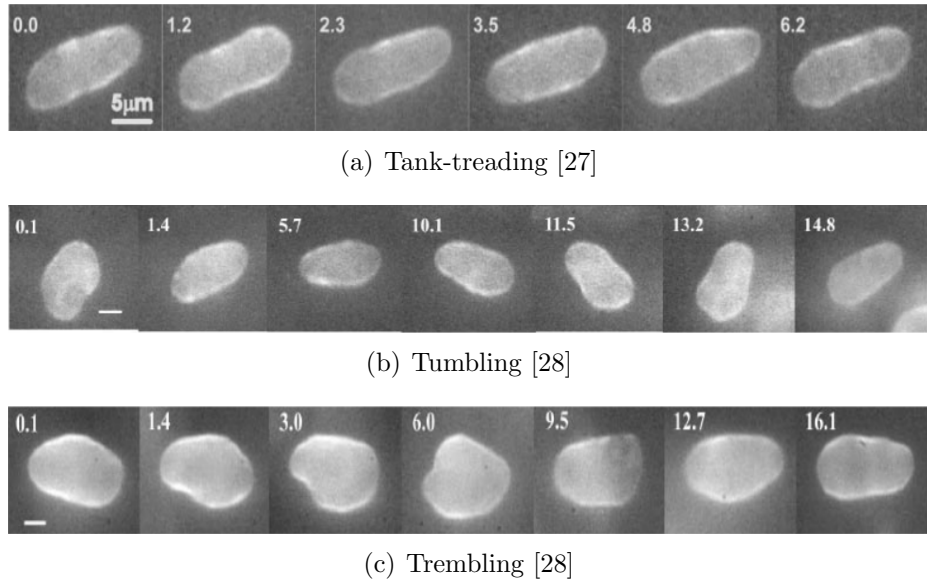
Figure 1.3: Snapshots of a vesicle under imposed shear flow. Different regimes of motion are observed depends on the reduced volume, dimensionless shear rate and the viscosity ratio between the inner and outer fluids.

Apart from all the available works on hydrodynamics of vesicles, of even greater interest is studying the electrohydrodynamic response of vesicles in various types and strengths of electric fields. In the presence of an external electric field the thin vesicle membrane acts as an electric capacitor and barrier to ion transport. This gives the vesicle a capacitive property which is very important in the dynamic response of the vesicle and the surrounding electric potential [84, 105]. A wide range of biotechnological applications have been reported using electric fields of both strong and weak forms. Weak fields have been applied in cell manipulation techniques such

as electrofusion [98], tissue ablation[12], wound healing [30], and treating tumors [86]. Strong electric fields induce electro-poration through formation of transient pores in the membrane. If the electric field is too strong, membrane collapses and cell death may occur [30]. However, a reversible poration process can be achieved through the application of a controlled electric field [31, 34, 68]. This is of a huge biotechnological interest for delivering substances such as drugs and DNA into living cells [58, 91]. Controlled electroporation remains a challenge and is the subject matter of ongoing research as the underlying physical mechanism of the membrane's response to strong electric fields is not well understood.

Experiments have been reported on the topological behavior of vesicles subjected to either a DC or AC electric field with different intensity, frequency or duration of exposure to the field [20, 66, 67, 75]. The time evolution of the vesicle in the electric field is described by the general terms of oblate and prolate shapes. In this context, the oblate shape (hamburger-like ellipsoid) happens when the two major axes of the ellipsoidal vesicle are perpendicular to the direction of applied electric field while in a prolate shape (egg-like ellipsoid), the only major axis of the ellipsoidal vesicle is colinear with the external electric field, see Fig. 1.4. Experiments show that depending on the conductivity and permittivity differences of the enclosed and surrounding fluids the vesicle may undergo a prolate or oblate transition.

One of the very interesting phenomena in this context is the dynamics of an initially prolate vesicle in a strong DC field with the conductivity of the enclosed fluid being smaller than the conductivity of the surrounding fluid. It is theoretically expected that as the membrane charges, the vesicle transitions to an oblate shape first, then eventually evolves back into the prolate shape. In other words, a prolate shape will always be the final equilibrium shape in such situations. However, possible formation of pores can short circuit the membrane capacitor along the way and this may sometimes cause the vesicle to remain in the oblate shape permanently. In a

5
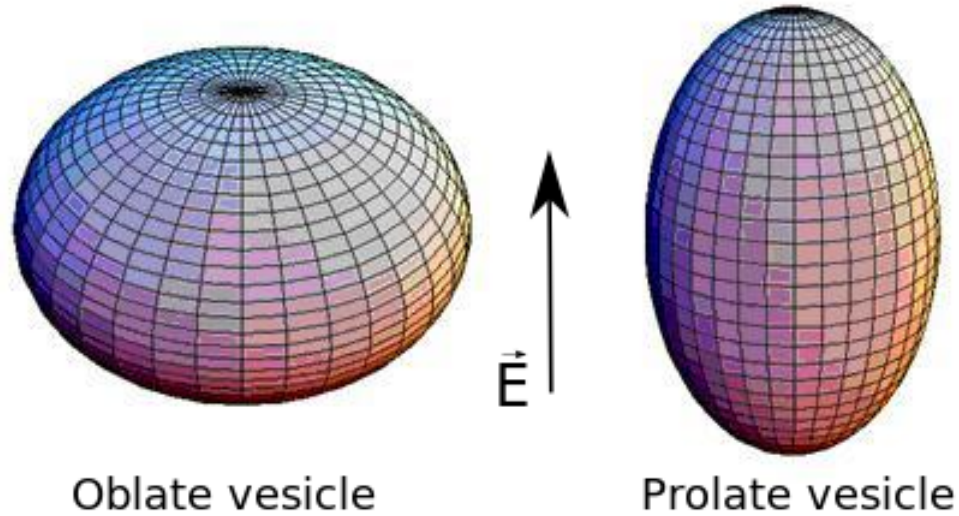
Figure 1.4: The prolate and oblate vesicles and their orientations with regard to the direction of the field.

more recent experiment, this Prolate-Oblate-Prolate (POP) transition was observed for a nearly spherical vesicle using a two-pulse technique [75]. A strong pulse with short duration is applied first to obtain the oblate deformation. This is followed by a weak long pulse to get the oblate-prolate transition (Fig 1.5(a)). Nearly cylindrical shapes with high-curvature edges were also observed for a vesicle subjected to strong pulses (Fig 1.5(b)) [67]. This behavior was claimed to be due to the presence of salt in the solution and not strictly the membrane characteristics. However, in a more recent study the vesicle poration was proposed as possible explanation for both vesicle collapsing and cylindrical deformations [76].

In addition to the experimental works, recent theoretical models have also investigated the electrohydrodynamics of nearly-spherical vesicles. Leading-order perturbation analysis has been employed to obtain reduced models in the form of ordinary differential equations [78, 79, 84, 96]. In another work, a spheroidal shell model is used to investigate the morphological change of the vesicle in AC electric field [102].

Despite numerous theoretical investigations, numerical studies of the vesicle electrohydrodynamics are quite rare. In a recent work, the boundary integral method
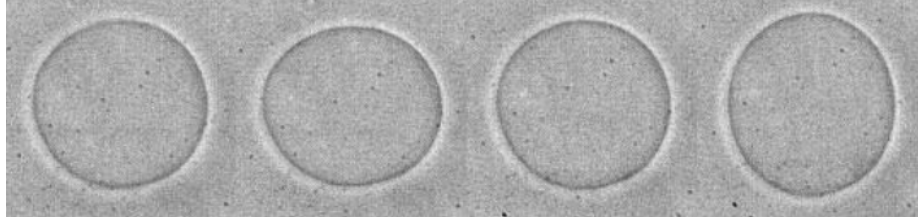
(a) Oblate to prolate transition using a two-pulse technique[75]
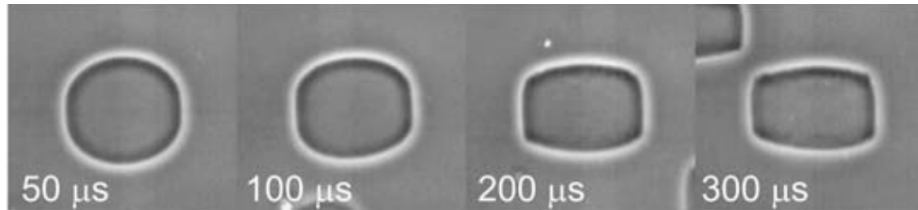
(b) Cylindrical deformation observed using strong electric field[67]

Figure 1.5: Different snapshots of a vesicle in the presence of strong DC fields.

was employed to study different equilibrium states of a two-dimensional vesicle in the presence of a uniform DC electric field [53]. The POP transition was captured for a vesicle with conductivity of the inner fluid being smaller than the surrounding region. However a direct comparison with available experimental data and physical parameters was not conducted. Also a two-fold reflection symmetry was enforced at each time step to avoid computer round-off errors and keep the vesicle symmetric in the direction perpendicular to the external electric field.

More recently, an Immersed Interface Method (IIM) was developed by the author which solves for both the electric potential and trans-membrane potential around a three-dimensional vesicle [32]. The jump conditions for the electric potential and its first and second derivatives on the interface are determined and utilized in the IIM to obtain accurate electric potential field solutions for a three-dimensional vesicle with an arbitrary shape. The details of algorithm, implementation and preliminary results using this method are discussed in Chapter 3.

Nevertheless, there is still a gap between the morphological changes observed in experiments, what theoretical models predict and what is yet to be learned from

vesicle behavior in electric fields. All these are deemed as essential prerequisites for building and developing reliable EHD microfluidic systems. Part of the difficulty arises from modeling the complex physics of the vesicle electrohydrodynamics and challenging phenomena such as membrane poration or fusion. Compared to hydrodynamics investigations, the electrohydrodynamics of the vesicle has substantially faster dynamics with much larger deformations which makes the numerical modeling nontrivial. Hence a lack of thorough numerical investigation with different material properties and electric field parameters still remains.

In this thesis the recently developed electric field model is combined with a projection-based hydrodynamics solver and a semi-implicit jet scheme for capturing the interface. This model is used to study the electrohydrodynamics of three dimensional vesicles in general flow. Ultimately, the dynamics of the vesicle is determined by the interplay between the hydrodynamics, bending, tension and electric field stresses on the membrane. To the best of the author's knowledge, this is the first attempt at investigating the electrohydrodynamics of vesicles in three-dimensions. As one may expect, for this kind of physics a three dimensional model will result in a much richer and wider range of topological changes than a two dimensional model. In addition to this, a full Navier-Stokes system of equations is considered here, unlike all the previous models which investigate the problem in the Stokes region. For vesicles in strong DC field, the approximate velocity may sometimes exceed $0.01 m/s$ [76] and therefore, the Stokes assumption for the fluid flow might be slightly simplistic. Moreover, the model here allows for studying highly deflected vesicles with small reduced volumes and is able to predict the type of deformations observed in experiments.

The three-dimensional parallel coding framework is developed in C programming language and parallelized using MPI. The code makes extensive use of high performance libraries including PETSc, Zoltan and HDF5. Different numerical experiments have been performed to determine the best solvers and preconditioners for the result-

ing linear systems. This framework has been used for running all the subsequent numerical work on massively parallel computer systems at the Center for Computational Research at SUNY Buffalo (UB CCR).

The rest of this dissertation is organized as follows. In Chapter 2 the physical picture and formulation behind the electrohydrodynamics of the vesicle is described. Chapter 3 focuses on the development of a numerical methodology for the implicit solutions of the electric potential and trans-membrane voltage. This includes a new implementation of the augmented IIM to compute the potential and electric field around a three-dimensional vesicle. Chapter 4 explores the numerical solution of the moving interface problem. A new semi-implicit formulation of the original gradient augmented level set method is presented and this is followed by a note on possible extension of the semi-implicit algorithm for the level set jet schemes. Chapter 5 details the development of a novel projection method to solve for the velocity field, pressure and tension. The volume incompressibility and surface in-extensibility conditions are being satisfied both locally and globally through applications of pressure and tension as two sets of Lagrange multipliers. This chapter finishes by giving the overall algorithm for the electrohydrodynamic simulation of the vesicle using all the above-mentioned proposed methods. Chapter 6 is devoted to sample results of the vesicle hydrodynamics in both quiescent flow and under linear shear flow in the context of experimental observations. The robustness of the method is tested by investigating different regimes of motions and comparing the results against experimental and other available numerical works. The major findings of this work is presented in Chapter 7 where the electrohydrodynamics of the vesicle in strong electric fields is vastly investigated. The success of the method in predicting the behaviors observed in experiments is justified. Also, a comprehensive investigation of the important parameter space is given for the POP transition. As another interesting example, the combined effects of DC fields with linear shear flow is investigated in this chapter.

The mixed effects of conductivity and viscosity ratios are studied in the context of causing tank-treading, tumbling or other yet unknown behaviors. Ultimately, Chapter 8 presents the final remarks including the implication of this analysis in the light of its biological applications and possible future work.

Chapter 2

Theory and Formulation

To gain physical insight into the problem a good understanding of the innate properties of the vesicle membrane is required. A vesicle in an aqueous solution may bear a qualitative resemblance to droplets in the sense that they are both deformable and a fluid-fluid interface is present in both situations. However, the structure of lipid bilayers in vesicles bring about more complex features which are not normally present in the modeling of drops and bubbles. The membrane fluidity, inextensibility, stretching and bending resistance are all important factors and the interplay between them determine the dynamics of the vesicle in fluid flow. Furthermore, application of an external electric field gives rise to another interesting yet complex behavior which is solely pertinent to vesicles; that is the impermeability of the vesicle membrane to ions and its function as an electric barrier to ion transport. This ion separation leads to a capacitive membrane with charges being stored on its surface. In this chapter, the physical picture for modeling the electrohydrodynamics of vesicles is presented and the relevant constitutive relations and governing equations are provided.

2.1 The mechanics of the membrane

Let a three-dimensional vesicle of encapsulated volume V have a surface area of A. The deviations from perfect sphericity is then measured by a reduced volume parameter, v, defined as the ratio of the vesicle volume to the volume of a sphere with the same surface area as the vesicle,

$$v = 3V/(4\pi a^3) \tag{2.1}$$

where $a = \sqrt{A/4\pi}$ is the characteristic length scale. The typical size of the vesicle is $a \approx 10 - 20\mu m$ while the thickness of the bilayer membrane is $d \approx 5nm$ [82]. Due to the three-orders of magnitude difference between the vesicle size and the membrane thickness the membrane can be treated as an infinitesimally thin interface separating the inner and outer fluids. The vesicle membrane is also assumed to be impermeable to the solvent molecules and the number of lipids on the membrane does not change over time. These two conditions result in an inextensible membrane with constant enclosed volume and local surface area. The resulting elastic properties are expressed in terms of the bending and tension traction forces of the membrane. These two forces together constitute the total membrane force per unit area and are calculated by taking the variational derivative from total energy of the membrane

$$\boldsymbol{\tau}_m + \boldsymbol{\tau}_\gamma = \frac{\delta \mathcal{E}}{\delta \Gamma} \tag{2.2}$$

where $\boldsymbol{\tau}_m$ is the bending traction and $\boldsymbol{\tau}_\gamma$ is the tension traction of the membrane, Γ is the vesicle surface area and $\mathcal{E}$ is the energy of the membrane. This energy is calculated using Helfrich model of surface energy [24]

$$\mathcal{E} = \int_\Gamma \left(\kappa_c \left(H - C_0 \right)^2 /2 + \kappa_g K + \gamma \right) dA. \tag{2.3}$$

12

In this relation, $H = \kappa_1 + \kappa_2$ is twice the mean curvature (the total curvature), κ_1 and κ_2 are the principle curvatures, $K = \kappa_1 \kappa_2$ is the Gaussian curvature, κ_c is the bending rigidity, κ_g is the Gaussian bending rigidity and C_0 is the intrinsic spontaneous curvature. According to the Gauss-Bonnet theorem, for a vesicle with unchanging topology the integral $\int_\Gamma \kappa_g K dA$ is constant [7]. Also in the absence of any asymmetry of the bilayer across the membrane one can set C_0 to zero. After taking the derivative and simplifying the terms, the bending and tension stresses are ultimately found to be

$$\boldsymbol{\tau}_m = \kappa_c(\frac{H^3}{2} - 2HK + \nabla_s^2 H)\boldsymbol{n}, \qquad \boldsymbol{\tau}_\gamma = \gamma H \boldsymbol{n} - \nabla_s \gamma, \qquad (2.4)$$

where ∇_s and ∇_s^2 are the surface gradient and surface Laplacian operators, γ is the tension and $\boldsymbol{n}$ is the outward unit normal on the interface. The total and Gaussian curvatures can be also formulated in terms of the the unit normal vector $\boldsymbol{n}$ such that

$$K = \nabla \cdot [\boldsymbol{n}\nabla \cdot \boldsymbol{n} + \boldsymbol{n} \times (\nabla \times \boldsymbol{n})], \qquad (2.5)$$

$$H = \nabla \cdot \boldsymbol{n}. \qquad (2.6)$$

Another important feature of the membrane is its insulating property and impermeability against ionic transfer. Consider a vesicle with electric conductivity of the interior region being smaller than the electric conductivity of the surrounding fluid. By applying an external electric field the charges in both regions start migrating towards the interface. However, accumulation of charges on the membrane happens at different rates due to the difference in the electric conductivity, see Fig. 2.1. This gives rise to a charge density imbalance on the two sides of the bilayer. With a zero thickness assumption for the membrane, this appears as an induced surface charge and makes the membrane acts as a capacitor in the presence of an external electric field. Therefore rather than having a continuous potential across the interface which

13

is the case for drops, a jump in the potential field is predicted on the vesicle membrane. The resulting capacitive property plays an important role in the dynamics of vesicles exposed to electric fields.
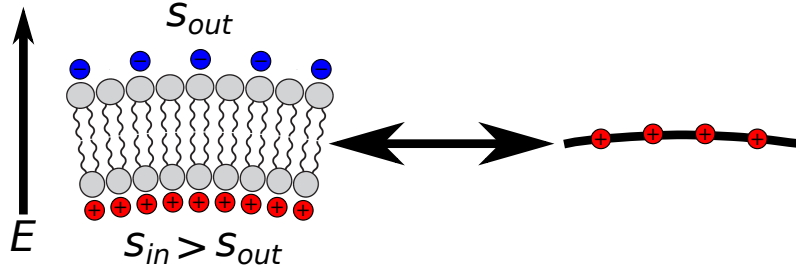
Figure 2.1: Part of the vesicle membrane subjected to external electric field. Under infinitesimally thin assumption, ion impermeability of the membrane and difference between electrical conductivity of the inner fluid, s_{in} versus conductivity of the outer fluid, s_{out}, the vesicle appears as an induced surface charge and acts as an electrical capacitance.

2.2 Electric field equations

A schematic of the vesicle exposed to an external electric field is illustrated in Fig. 2.2. Different properties inside$(-)$ and outside$(+)$ of the membrane are shown in the figure. The embedded region (Ω^-) is separated from the surrounding region (Ω^+) by the vesicle membrane represented as Γ. This membrane is assumed to be made of charge-free lipid bilayers with a capacitance C_m and conductivity G_m. The vesicle suspended in a media of conductivity s^+ and dielectric constant ϵ^+. The enclosed region is assumed to have a different conductivity s^- and dielectric constant ϵ^-. Both fluids are treated as leaky dielectrics and thus are weakly conducting.

Since there is no local free charge density in the domain, the electric field $(\boldsymbol{E})$ is irrotational and given as the negative gradient of the electric potential (Φ),

$$\boldsymbol{E}^k = -\nabla \Phi^k. \tag{2.7}$$
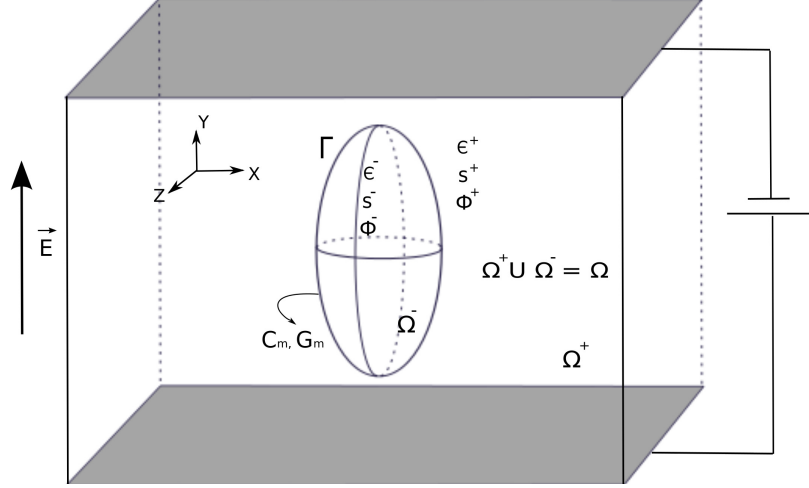
Figure 2.2: Schematic of a vesicle subjected to external electric field

Equation (2.7) implies that the electric potential is a solution of Laplace equation in each domain

$$\nabla^2 \Phi^k = 0. \tag{2.8}$$

However, the presence of the capacitive interface leads to a discontinuity in the potential across the membrane

$$\Phi^+ - \Phi^- = -V_m(t), \tag{2.9}$$

where $V_m(t)$ is the time-varying trans-membrane potential and can be obtained from the conservation of current density across the membrane [85, 84, 19],

$$C_m \frac{\partial V_m}{\partial t} + G_m V_m = s^\pm (\boldsymbol{n} \cdot \boldsymbol{E}^\pm) + \epsilon^\pm \frac{\partial (\boldsymbol{E}^\pm)}{\partial t} \cdot \boldsymbol{n} + \nabla_s \cdot \left(\boldsymbol{u} Q^\pm \right), \tag{2.10}$$

where $Q^\pm$ is the induced charge densities on the top and bottom side of the membrane and $\boldsymbol{n}$ is the outward facing normal vector on the interface. In the limit of fast bulk charge relaxation and negligible charge convection the time evolution of $\boldsymbol{E}^\pm$ and the convection of charges can be ignored [84]. If the response of the system in the

15

presence of AC electric fields is desired then these terms must be kept. Under these assumptions the simplified version of Eq. (2.11) is ultimately given as

$$C_m \frac{dV_m}{dt} + G_m V_m = \boldsymbol{n} \cdot (s^\pm \boldsymbol{E}^\pm). \tag{2.11}$$

Assuming that the membrane conductance and capacitance have uniform and constant values on the interface, the trans-membrane potential will only depend on changes in the surrounding domain electric potential and the interface shape. Furthermore, the continuity of the Ohmic current $\boldsymbol{J} = s\boldsymbol{E}$ in the normal direction across the membrane can be written as

$$\boldsymbol{n} \cdot (\boldsymbol{J}^+ - \boldsymbol{J}^-) = \boldsymbol{n} \cdot (s^+ \boldsymbol{E}^+ - s^- \boldsymbol{E}^-) = 0. \tag{2.12}$$

The net charges density Q induced on the membrane as a result of external electric field is expressed as the jump in the normal component of displacement field $D = \epsilon \boldsymbol{E}$

$$\boldsymbol{n} \cdot (\epsilon^+ \boldsymbol{E}^+ - \epsilon^- \boldsymbol{E}^-) = Q. \tag{2.13}$$

This net charge imbalance across the interface occurs due to the fact that charges from inside and outside of the vesicle accumulate on the interface at different rates. This itself is because of the difference in electrical conductivities of the internal and external regions. The electric stress $\boldsymbol{\tau}_{el}$ acting on the membrane is obtained from the Maxwell tensor $\boldsymbol{T}_{el}$:

$$\boldsymbol{\tau}_{el} = \boldsymbol{n} \cdot (\boldsymbol{T}_{el}^+ - \boldsymbol{T}_{el}^-), \quad \boldsymbol{T}_{hd} = \epsilon(\boldsymbol{E}\boldsymbol{E} - \frac{1}{2}\boldsymbol{E} \cdot \boldsymbol{E}\boldsymbol{I}) \quad \text{on} \quad \Gamma. \tag{2.14}$$

2.3 Fluid flow equations

Assume that both fluids are Newtonian and incompressible with a matched density ρ. Consequently they both satisfy the Navier-Stokes equations,

$$\rho\frac{D\boldsymbol{u}^\pm}{Dt} = \nabla \cdot \boldsymbol{T}^\pm_{hd} \ \ \text{and} \ \ \nabla \cdot \boldsymbol{u}^\pm = 0 \ \ \text{in} \ \ \Omega^\pm. \tag{2.15}$$

where $\boldsymbol{u}$ is the velocity vector and $\boldsymbol{T}_{hd}$ is the bulk hydrodynamic stress tensor defined as

$$\boldsymbol{T}^\pm_{hd} = -p^\pm\boldsymbol{I} + \mu^\pm(\nabla\boldsymbol{u}^\pm + \nabla^T\boldsymbol{u}^\pm) \ \ \text{in} \ \ \Omega^\pm. \tag{2.16}$$

The fluid flow in each region is coupled via the conditions on the inextensible membrane. The velocity is assumed to be continuous on the surface, $[\boldsymbol{u}] = 0$. However, the hydrodynamic stress undergoes a jump across the interface of the two fluids. This condition is obtained by balancing the hydrodynamic and electric stresses with bending traction, $\boldsymbol{\tau}_m$, and in-extension traction, $\boldsymbol{\tau}_\gamma$ of the membrane

$$\boldsymbol{\tau}_{hd} + \boldsymbol{\tau}_{el} = \boldsymbol{\tau}_m + \boldsymbol{\tau}_\gamma \ \ \text{on} \ \ \Gamma. \tag{2.17}$$

where $\boldsymbol{\tau}_{hd}$ is defined as $\boldsymbol{\tau}_{hd} = \boldsymbol{n} \cdot (\boldsymbol{T}^+_{hd} - \boldsymbol{T}^-_{hd})$.

The last but not least is the local area incompressibility constraint on the membrane. This condition is enforced by ensuring that the velocity is surface-divergence free on the membrane

$$\nabla_s \cdot \boldsymbol{u} = 0 \ \ \text{on} \ \ \Gamma. \tag{2.18}$$

2.4 Description of the interface

The motion of the interface is tracked using a gradient-augmented level set method. First developed by Osher and Sethian [61] the level set method is based upon an

implicit representation of an interface as the zero level set of a higher dimensional function. This was later extended to explicitly include information about the gradients of the level set [56]. The use of gradient information allows for the accurate determination of the interface location and curvature information away from grid node locations [56].

Using the same notation for the interface as Fig. 2.2 the level set function ϕ is defined as

$$\Gamma(t) = \{\boldsymbol{x} : \phi(\boldsymbol{x}, t) = 0\}, \tag{2.19}$$

while the level set gradient field is defined as

$$\boldsymbol{\psi} = \nabla \phi. \tag{2.20}$$

The level set value is chosen to be negative in the Ω^- and positive in the Ω^+ domain. This representation has the advantages of treating any topological changes naturally without complex remeshing, and the ability to calculate geometric quantities from the level set function and its derivatives. For example, the unit normal to the surface, $\boldsymbol{n}$, can be easily computed as

$$\boldsymbol{n} = \frac{\boldsymbol{\psi}}{\|\boldsymbol{\psi}\|}. \tag{2.21}$$

The motion of the interface under the flow field $\boldsymbol{u}$ is modeled by a standard advection equation

$$\frac{\partial \phi}{\partial t} + \boldsymbol{u} \cdot \nabla \phi = 0. \tag{2.22}$$

The evolution of the gradient field is obtained by taking the gradient of the level set advection equation,

$$\frac{\partial \boldsymbol{\psi}}{\partial t} + \boldsymbol{u} \cdot \nabla \boldsymbol{\psi} + \nabla \boldsymbol{u} \cdot \boldsymbol{\psi} = 0. \tag{2.23}$$

Using the level set function one is able to define the viscosity at any location in the computational domain, $\boldsymbol{x}$, with a single relation,

$$\mu(\boldsymbol{x}) = \mu^- + (\mu^+ - \mu^-)H(\phi(\boldsymbol{x})), \tag{2.24}$$

where H is the Heaviside function. Different first and second order accurate regularization formulations have been proposed to approximate Heaviside and Dirac delta functions [65, 88, 22]. Here an accurate method based on an integral calculation [90] is used. The Heaviside is defined as

$$H(\phi(\boldsymbol{x})) = \frac{\nabla\Im(\phi(\boldsymbol{x})) \cdot \nabla\phi(\boldsymbol{x})}{\|(\nabla\phi(\boldsymbol{x}))\|^2} \tag{2.25}$$

where

$$\Im(z) = \int_0^z \bar{H}(\zeta)d\zeta \qquad \text{and} \qquad \bar{H}(\zeta) = \begin{cases} 0 & \text{if } \zeta < 0 \\ 1 & \text{if } \zeta > 0 \end{cases}.$$

Similarly the Dirac delta function is expressed as

$$\delta(\phi(\boldsymbol{x})) = \frac{\nabla H(\phi(\boldsymbol{x})) \cdot \nabla\phi(\boldsymbol{x})}{\|(\nabla\phi(\boldsymbol{x}))\|^2}. \tag{2.26}$$

The Dirac delta function will be used to localize the contributions of interface forces in Navier-Stokes equations.

2.5 Continuous Surface Force Model

Through utilization of the level set properties and definitions given for Heaviside and Dirac delta functions one is able to rewrite the hydrodynamic equations of binary fluids with different properties into one single formulation [13]. Another interesting

aspect of this formulation is that the singular forces of the membrane can be embedded into a body force term and included in the momentum equation. Therefore the contributions due to the electric field, bending and surface tension of the vesicle can be localized over a small region near the interface using the Dirac delta function. This is accomplished by writing the singular contributions of the bending, tension, and electric field forces as localized body force terms, similar to what has been done for two dimensional vesicles [72, 74]. Putting together this representation with the governing equations in (2.15) and surface conditions in (2.17) we write the hydrodynamic equation of the vesicle in the single-fluid form for the entire domain as (See appendix A for the proof)

$$
\begin{aligned}
\rho \frac{D\boldsymbol{u}}{Dt} = &-\nabla p + \nabla \cdot (\mu(\nabla \boldsymbol{u} + \nabla^T \boldsymbol{u})) \\
&+ \delta(\phi)\bigg(\mid \nabla\phi \mid \nabla_s\gamma - \gamma H \nabla\phi\bigg) \\
&+ \kappa_c \delta(\phi)\bigg(\frac{H^3}{2} - 2KH + \nabla_s^2 H\bigg)\nabla\phi \\
&+ \delta(\phi)\mid \nabla\phi \mid \boldsymbol{n} \cdot \bigg[\epsilon(\boldsymbol{EE} - \frac{1}{2}\boldsymbol{E} \cdot \boldsymbol{EI})\bigg]
\end{aligned}
\tag{2.27}
$$

with

$$
\nabla \cdot \boldsymbol{u} = 0 \quad \text{in} \quad \Omega.
\tag{2.28}
$$

$$
\nabla_s \cdot \boldsymbol{u} = 0 \quad \text{on} \quad \Gamma.
\tag{2.29}
$$

As it will be explained in the Level Set Reinitialization and Closest Point Calculations in Chapter 4, all surface quantities in the above formulation such as tension or the jump of the Maxwell stress tensor, are calculated on the interface and extended such that they are constant in the direction normal to the interface.

2.6 Dimensionless Parameters

There are several physical time scales associated with the electrohydrodynamics of the vesicle. When an electric field is applied to the system charges from inside and outside of the membrane start migrating to the interface at different rates which causes inhomogeneous redistribution of bulk charge density. The time scale associated with this migration process is given by the bulk charge relaxation time [77, 54],

$$t_c^{\pm} = \frac{\epsilon^{\pm}}{s^{\pm}}. \tag{2.30}$$

For an ion-impermeable membrane the characteristic time scale associated with the charging process is given by [91, 31]

$$t_m = aC_m \left(\frac{1}{s^-} + \frac{1}{2s^+} \right), \tag{2.31}$$

where a is the characteristic length scale previously defined in Sec.2.1. The applied electric stresses act to deform the vesicle membrane on the electrohydrodynamics time scale given by

$$t_{ehd} = \frac{\mu^+(1+\eta)}{\epsilon^+ E_0^2}, \tag{2.32}$$

where the applied electric field has a strength of E_0 and $\eta = \mu^-/\mu^+$ is the viscosity ratio. The bending forces act to restore the membrane to an equilibrium configuration on the bending time scale,

$$t_\kappa = \frac{\mu^+ a^3 (1+\eta)}{\kappa_c}. \tag{2.33}$$

Finally, the response time of a vesicle to any externally applied shear flow is simply the inverse of the shear rate, $\dot{\gamma}_0$,

$$t_{\dot{\gamma}} = \frac{1}{\dot{\gamma}_0}. \tag{2.34}$$

21

In order to choose a proper simulation time scale, it is beneficial to estimate the order of magnitude for the times at which different physical processes occur. Typical experimental values of the physical properties have been reported as $a \approx 20~\mu$m, $\kappa_c \approx 10^{-19}$ J, $s^+ \approx 10^{-3}$ S/m, $s^- = s^+/10$, $\epsilon^+ \approx 10^{-9}$ F/m, $C_m \approx 10^{-2}$ F/m^2, $\rho \approx 10^3$ kg/m^3, $\dot{\gamma}_0 \approx 1~s^{-1}$ and $\mu^- = \mu^+ \approx 10^{-3}$ Pa s [67, 75, 57, 70]. Using these values the bulk charge relaxation time is $t_c \approx 10^{-6}$ s, the bending time scale is $t_{\kappa_c} \approx 160$ s, the membrane charging time scale is $t_m \approx 2 \times 10^{-3}$ s, the time scale for shear is $t_{\dot{\gamma}} = 1$ s and for an electric field of $E_0 = 10^5$ V/m the electrohydrodynamic time scale will be $t_{ehd} \approx 10^{-4}$ s.

The first thing to notice is that the bulk charge accumulation on the interface happens in a much faster time than any other events. Therefore, it can be concluded that the electric field adjusts to a new configuration of the vesicle and fluid almost instantaneously and the quasi-static assumption for the electric field in Eq (2.7) is valid. It is also important to note that with this parameter set the electrohydrodynamics time scale, t_{ehd}, is faster than the membrane charging time scale, t_m. If this is not the case then the vesicle membrane will not be able to respond quickly enough to the applied forces, and only small deformations will be observed [75, 79].

2.7   Nondimensional Model

Given a characteristic length a and time t_0 the characteristic velocity is given by $u_0 = a/t_0$. Material quantities such as viscosity and permittivity are normalized by their counterparts in the (outer) bulk fluid (*i.e.* $\hat{\mu} = \mu/\mu^+$ and $\hat{\epsilon} = \epsilon/\epsilon^+$). The

dimensionless fluid equations are written as

$$\frac{D\hat{\boldsymbol{u}}}{D\hat{t}} = -\hat{\nabla}\hat{p} + \frac{1}{Re}\hat{\nabla} \cdot (\hat{\mu}(\hat{\nabla}\hat{\boldsymbol{u}} + \hat{\nabla}^T\hat{\boldsymbol{u}}))$$

$$+ \delta(\phi)\|\hat{\nabla}\phi\| \left(\hat{\nabla}_s\hat{\gamma} - \hat{\gamma}\hat{H}\hat{\nabla}\phi \right)$$

$$+ \frac{1}{Ca\,Re}\delta(\phi) \left(\frac{\hat{H}^3}{2} - 2\hat{K}\hat{H} + \hat{\nabla}_s^2\hat{H} \right) \hat{\nabla}\phi \qquad (2.35)$$

$$+ \frac{Mn}{Re}\delta(\phi)\|\hat{\nabla}\phi\| \left[\hat{\epsilon} \left(\hat{\boldsymbol{E}}\hat{\boldsymbol{E}} - \frac{1}{2} \left(\hat{\boldsymbol{E}} \cdot \hat{\boldsymbol{E}} \right) \boldsymbol{I} \right) \right] \cdot \boldsymbol{n}$$

where dimensionless quantities are denoted by a hat. The velocity at the boundary of the domain is given as $u_\infty = \chi\hat{y}$ where $\chi = \dot{\gamma}t_0$ is the normalized applied shear rate. The uniform DC electric field at the boundary is imposed as $\Phi_\infty = \hat{E}\hat{y}$ where $\hat{E}$ is the normalized strength of the applied electric field. The dimensionless parameters are defined as follows. The Reynolds number is taken to be $Re = \rho u_0 a/\mu^+$, while the strength of the bending is given by a capillary-like parameter, $Ca = t_\kappa/t_0$ and the strength of the electric field is given by the Mason number, $Mn = t_0/t_{ehd}$.

The time-evolution equation of the transmembrane potential is nondimensional-ized in a similar manner:

$$\hat{C}_m\frac{\partial\hat{V}_m}{\partial\hat{t}} + \hat{G}_m\hat{V}_m + \hat{\boldsymbol{u}} \cdot \nabla \left(\hat{C}_m\hat{V}_m \right) = \lambda\hat{\boldsymbol{n}} \cdot \hat{\boldsymbol{E}}^- = \hat{\boldsymbol{n}} \cdot \hat{\boldsymbol{E}}^+, \qquad (2.36)$$

where the dimensionless membrane capacitance is given as $\hat{C}_m = (C_m a)/(t_0 s^+)$, the dimensionless membrane conductivity is $\hat{G}_m = (G_m a)/s^+$ and the conductivity ratio is expressed as $\lambda = s^-/s^+$.

The most appropriate time scale would be the one that enables us to capture all the important physics in the problem. For electrohydrodynamic simulations in the absence of shear flow the most appropriate time scale is the membrane-charging time, t_m [75]. This is due to the significantly faster dynamics of the vesicle in electric fields than the hydrodynamic problem. Hence for all the electrohydrodynamic

computations with no imposed shear flow ($\chi = 0$) the simulation time scale is set to $t_0 = t_m$ and the dimensionless parameters Re, Ca and Mn are calculated accordingly. However, using the membrane charging time scale for the hydrodynamic simulations ($Mn = 0$) will lead to abnormally huge number of iterations. On the other hand, the CFL limitations do not allow for taking larger time steps in this situation. Therefore for the hydrodynamic computations the simulation time scale is set to the time scale associated with shear flow ($t_0 = t_{\dot{\gamma}}$). This time scale has been also used for the investigation of the vesicle dynamics under combined shear flow and weak electric field. This seems to be a rational choice as the time scale of the applied weak electric field is in the same range as the one for the shear flow.

Using the typical experimental values of the physical parameters discussed earlier in Sec. 2.6 the non-dimensional numbers for simulations in the absence of shear are $t_0 = t_m = 2.1 \times 10^{-3}$ s, $\hat{C}_m = 0.095$, $\hat{G}_m = 0$, $Re = 0.19$, $Ca = 3.8 \times 10^4$, $Mn = 18$, $E_0 = 1$, and $\chi = 0$. Clearly, at this time scale the Reynolds number is not small enough to justify the Stokes approximation while the bending contribution is almost negligible. Despite the small contribution from the bending in this situation it is kept in the formulation as it may become important during other time-scales, such as when shear is applied.

For simplicity the hat notation in the equations henceforth dropped. All the above mentioned parameters along with the viscosity ratio, η, and reduced volume, v, will be used to investigate the dynamics of a three-dimensional vesicle in different flow conditions and strength of electric field.

Chapter 3

The Solution of the Electric Field

Consider solving for the potential in the entire domain, $\nabla^2 \Phi = 0$, using a finite difference method. Large errors are introduced into the solution near the interface due to the discontinuous electrical conductivity and potential field. A simplified augmented Immersed Interface Method is used in this work to address the issue of solving discontinuous PDEs across an embedded interface. To produce accurate solutions the jump of the solution across the interface is included in the numerical discretization.

In this chapter the Immersed Interface Method is briefly described. This is followed by the derivation of the electric potential jump conditions and the specific numerical implementation. Lastly, various numerical experiments are presented to illustrate the convergence, accuracy and robustness of the present method. Investigations verify the second-order accuracy of the underlying discretization even in the presence of solution discontinuities. The content of this chapter is published in *Applied Mathematics Letters* [33].

3.1 The Immersed Interface Method

First introduced by Leveque and Li [42], the Immersed Interface Method is a finite difference method used to solve discontinuous PDE fields across an embedded interface. To produce accurate solutions the jump conditions of the solution are explicitly included in the numerical scheme. This method has been used extensively to solve elliptic problems with interfaces [42, 43, 44] and later was extended to model the Stokes or Navier-Stokes equations with singular forces and discontinuous viscosity [47, 40]. Furthermore, this method is able to handle sharp interfaces with discontinuities and singularities in the coefficients and the solutions [45].

In the Immersed Interface Method grid points can be classified as either regular or irregular points, schematically shown in Fig. 3.1. Regular nodes are defined as those nodes where the interface does not cross the discretization of the PDE. These nodes are treated normally upon discretization, meaning that no modification needs to be applied to the stencil. Irregular nodes, on the other hand, are the ones where the interface crosses the stencil. Modifications need to be made to take into account the discontinuity of the solution at such nodes.

Consider the solution of the electric potential from Eq. (2.8). For the irregular node $\boldsymbol{\chi}_{i,j}$, shown in Fig. 3.1, a second-order central finite difference discretization of the Laplace operator results in

$$\frac{\Phi^+_{i,j-1} + \Phi^+_{i-1,j} - 4\Phi^+_{i,j} + \Phi^+_{i+1,j} + \Phi^+_{i,j+1}}{h^2} = 0, \tag{3.1}$$

where we have made the assumption that the whole stencil exists in the Ω^+ domain. However, in reality the point $\boldsymbol{\chi}_{i,j-1}$ resides in the Ω^- domain, not the Ω^+ domain. To account for this mismatch in the discretization we define a jump in a quantity f
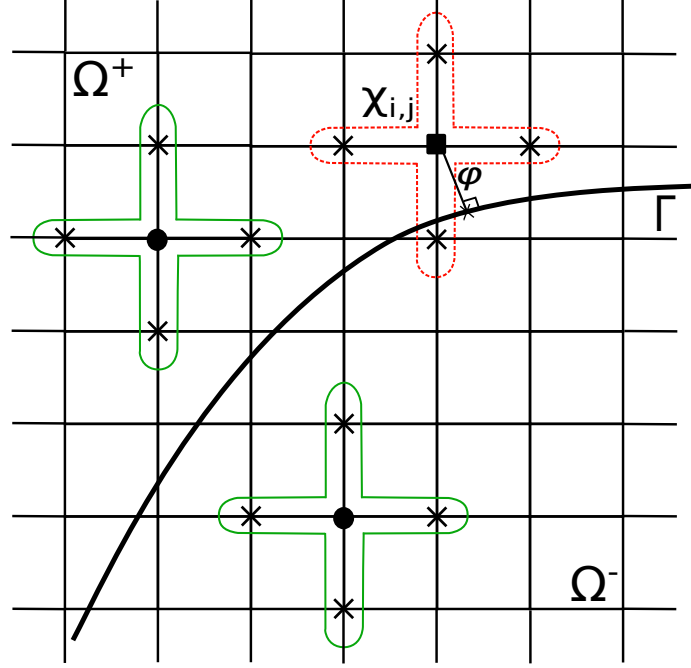
Figure 3.1: Sample stencils for regular node (circle) and irregular node (square). The stencil in dashed-red crosses the interface and corrections need to be applied. Here φ is the signed distance function to the closest point on the interface from a grid point.

across the interface as

$$[f] = \lim_{\epsilon \to 0^+} f(\boldsymbol{\chi}_\Gamma + \epsilon \boldsymbol{n}) - \lim_{\epsilon \to 0^+} f(\boldsymbol{\chi}_\Gamma - \epsilon \boldsymbol{n}), \tag{3.2}$$

where $\boldsymbol{\chi}_\Gamma$ is the closest-point location on the interface to the grid point $\boldsymbol{\chi}$ and $\boldsymbol{n}$ is the outward normal vector (Fig. 3.2). Quantities on the interface can be defined based on the direction from which the interface is approached,

$$f^- = \lim_{\epsilon \to 0^+} f(\boldsymbol{\chi}_\Gamma - \epsilon \boldsymbol{n}), \tag{3.3}$$

$$f^+ = \lim_{\epsilon \to 0^+} f(\boldsymbol{\chi}_\Gamma + \epsilon \boldsymbol{n}). \tag{3.4}$$

Assume that the physics of the problem provides enough information to derive the jumps in the solution, $[\Phi]$, the first normal derivative, $[\partial\Phi/\partial n]$, and the second normal derivative, $[\partial^2\Phi/\partial n^2]$, on the interface. Consequently the jump can be extended to a

27
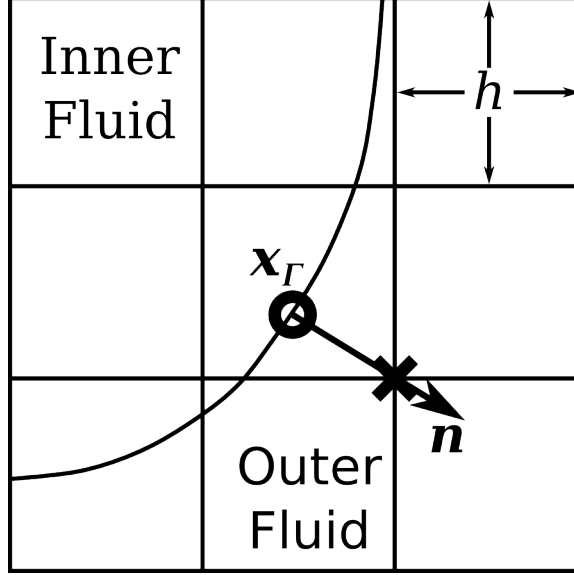
Figure 3.2: Sample grid showing interface and outward facing normal. The grid node denoted by the cross requires corrections due to discontinuities in the stencil. The corrections are calculated at the circle and extended out to the grid node.

grid point by applying a Taylor Series expansion in the normal direction about the closest point location [23, 38],

$$[\Phi]_{i,j} = [\Phi] + \varphi_{i,j}\left[\frac{\partial \Phi}{\partial n}\right] + \frac{\varphi_{i,j}^2}{2}\left[\frac{\partial^2 \Phi}{\partial n^2}\right] + O(h^3), \qquad (3.5)$$

where $\varphi_{i,j}$ is the signed distance function from the grid point $\boldsymbol{\chi}_{i,j}$ to the corresponding location on the interface. By extending the solution jumps from the interface to the grid points it can be written that $\Phi_{i,j-1}^+ = \Phi_{i,j-1}^- - [\Phi]_{i,j-1}$. Using this expression in Eq. (3.1) results in the corrected discretization,

$$\frac{\Phi_{i,j-1}^- + \Phi_{i-1,j}^+ - 4\Phi_{i,j}^+ + \Phi_{i+1,j}^+ + \Phi_{i,j+1}^+}{h^2} + \frac{[\Phi]_{i,j-1}}{h^2} = 0. \qquad (3.6)$$

The known jump value, $[\Phi]_{i,j-1}$, is obtained from Eq. (3.5) and can be moved to the right-hand side of the linear system as an explicit correction term,

$$\frac{\Phi_{i,j-1}^- + \Phi_{i-1,j}^+ - 4\Phi_{i,j}^+ + \Phi_{i+1,j}^+\Phi_{i,j+1}^+}{h^2} = C_{i,j}, \qquad (3.7)$$

28

where $C_{i,j} = -[\Phi]_{i,j-1}/h^2$ is the total correction needed to discretize the Laplace operator over the irregular node $\chi_{i,j}$. The extension of this method to irregular nodes on either side of the interface and to three-dimensional systems is straight-forward.

3.1.1 The electric potential jump conditions

By including the corrections the governing equation for the electric potential is written over the entire domain as,

$$\nabla^2 \Phi = \boldsymbol{C}, \tag{3.8}$$

where the total correction $\boldsymbol{C}$ is only non zero for irregular nodes. To obtain second-order spatial accuracy in the solution the jumps in the electric potential and up to the second normal derivative are needed across the interface [38]. The first jump condition is obtained directly from the time-varying trans-membrane voltage, Eq. (2.9),

$$[\Phi] = -V_m, \tag{3.9}$$

where V_m is a time-varying quantity with the evolution being described by Eq. (2.11). To discretize this equation, first make use of Eq. (2.7) to express the electric field in terms of the electric potential. This results in the expression

$$C_m \frac{dV_m}{dt} + G_m V_m = -s^{\pm} \frac{\partial \Phi^{\pm}}{\partial n}. \tag{3.10}$$

Using a second-order in time discretization and treating the term $G_m V_m$ implicitly results in

$$C_m \frac{3V_m^{n+1} - 4V_m^n + V_m^{n-1}}{2\Delta t} + G_m V_m^{n+1} = -s^{\pm} \frac{\partial \Phi^{\pm}}{\partial n}. \tag{3.11}$$

Solving for the trans-membrane potential V_m^{n+1} gives the jump of the electric potential across the interface in Eq.(3.9),

$$[\Phi] = \frac{1}{3C_m + 2\Delta t G_m}(2\Delta t s^{\pm}\frac{\partial\Phi^{\pm}}{\partial n} - 4C_m V_m^n + C_m V_m^{n-1}).$$

(3.12)

To derive the jump condition for the first normal derivative of electric potential the continuity of current density across the interface is used:

$$0 = s^+\frac{\partial\Phi^+}{\partial n} - s^-\frac{\partial\Phi^-}{\partial n},$$

(3.13)

$$0 = s^+\frac{\partial\Phi^+}{\partial n} - s^-\frac{\partial\Phi^-}{\partial n} + s^-\frac{\partial\Phi^+}{\partial n} - s^-\frac{\partial\Phi^+}{\partial n},$$

(3.14)

$$0 = (s^+ - s^-)\frac{\partial\Phi^+}{\partial n} + s^-\left(\frac{\partial\Phi^+}{\partial n} - \frac{\partial\Phi^-}{\partial n}\right),$$

(3.15)

$$0 = [s]\frac{\partial\Phi^+}{\partial n} + s^-\left[\frac{\partial\Phi}{\partial n}\right].$$

(3.16)

Similarly it can be shown that

$$0 = [s]\frac{\partial\Phi^-}{\partial n} + s^+\left[\frac{\partial\Phi}{\partial n}\right].$$

(3.17)

Solving for the jump in the normal electric field yields

$$\left[\frac{\partial\Phi}{\partial n}\right] = -\frac{[s]}{s^+}\frac{\partial\Phi^-}{\partial n} = -\frac{[s]}{s^-}\frac{\partial\Phi^+}{\partial n}.$$

(3.18)

For the jump in the second normal derivative, start with the relation between the Laplacian and the surface Laplacian of an arbitrary scalar function,

$$\nabla^2\Phi \equiv \nabla_s^2\Phi + H\frac{\partial\Phi}{\partial n} + \frac{\partial^2\Phi}{\partial n^2}.$$

(3.19)

where $\nabla_s^2 = [(\boldsymbol{I} - \boldsymbol{n}\otimes\boldsymbol{n})\,\nabla]\cdot[(\boldsymbol{I} - \boldsymbol{n}\otimes\boldsymbol{n})\,\nabla]$ is the surface Laplacian and $H = \nabla\cdot\boldsymbol{n}$ is the total curvature. As there is no jump in the curvature applying the jump operator

30

results in

$$[\nabla^2\Phi] = [\nabla_s^2\Phi] + H[\frac{\partial\Phi}{\partial n}] + [\frac{\partial^2\Phi}{\partial n^2}], \qquad (3.20)$$

Previous work has shown that the jump condition commutes with differentiation along the interface, $[\nabla_s^2\Phi] = \nabla_s^2[\Phi]$, see Ref. [100]. Also note that the jump in the Laplacian of the electric potential is zero, $[\nabla^2\Phi] = 0$. It is thus possible to write the jump in the second normal derivative as

$$\left[\frac{\partial^2\Phi}{\partial n^2}\right] = -\nabla_s^2[\Phi] - H\left[\frac{\partial\Phi}{\partial n}\right], \qquad (3.21)$$

where the expressions for $[\Phi]$ and $[\partial\Phi/\partial n]$ are already given in Eq. (2.9) and Eq. (3.18), respectively.

The jumps are calculated on the interface and extended to the surrounding nodes by extrapolating in the normal direction. The extended jumps at grid points, $[\Phi]_{gp}$, are given by

$$[\Phi]_{gp} = [\Phi] + d\left[\frac{\partial\Phi}{\partial n}\right] + \frac{d^2}{2}\left[\frac{\partial^2\Phi}{\partial n^2}\right], \qquad (3.22)$$

where d is the signed distance from the grid point to the interface. Using these extended jumps the corrections can be calculated, see Ref. [38] for more information on the Immersed Interface Method.

3.1.2   Implementation details

The goal is to solve for the electric potential field in a rectangular domain discretized using a Cartesian grid with uniform grid spacing h. Let the Ω^{min} domain contain the fluid with the *smaller* electrical conductivity. To proceed with the numerical implementation define the normal electric field in the Ω^{min} domain as $r = \partial\Phi^{min}/\partial n$. Note that this quantity is only defined on the embedded interface. With the new

definition the complete set of jump conditions in Sec. 3.1.1 can be rewritten as

$$[\Phi] = \frac{1}{3C_m + 2\Delta t G_m}(2\Delta t s^{min}r - 4C_m V_m^n + C_m V_m^{n-1}), \qquad (3.23)$$

$$[\frac{\partial \Phi}{\partial n}] = -\frac{[s]}{s^{max}}r, \qquad (3.24)$$

$$[\frac{\partial^2 \Phi}{\partial n^2}] = \nabla_s^2[\Phi] - H\left[\frac{\partial \Phi}{\partial n}\right], \qquad (3.25)$$

where s^{max} is the larger of the two fluid conductivities. If r is known then the jump conditions are fully defined. It would then be possible to use the Immersed Interface Method to solve for Φ in the entire domain. Unfortunately, the value of r is not explicitly known but must be determined as part of the problem. Here a technique first introduced for the solution of the Stokes equations [46] is used to determine Φ^{n+1} and r simultaneously.

All the electric potential jump conditions are linear. Hence, all the Immersed Interface corrections will be linear near the interface. Therefore, the resulting linear system from the field equation in Eq. (3.8) can be written in operator form as

$$\boldsymbol{L}\Phi = \boldsymbol{C}, \qquad (3.26)$$

where $\boldsymbol{L}$ is the Laplacian operator and $\boldsymbol{C}$ is the vector containing the required corrections. The total correction $\boldsymbol{C}$ can be split into corrections due to $\boldsymbol{r}$ and transmembrane potential at time t^{n-1} and t^n,

$$\boldsymbol{C} = \boldsymbol{A_0}\boldsymbol{r} + \boldsymbol{B_0} \qquad (3.27)$$

where $\boldsymbol{A_0}$ is a linear operator and $\boldsymbol{B_0}$ contains the known contribution from the previous voltages. By combining (3.27) and (3.26), it is possible to solve for electric potential,

$$\Phi = \boldsymbol{L}^{-1}\boldsymbol{A_0}\boldsymbol{r} + \boldsymbol{L}^{-1}\boldsymbol{B_0}. \qquad (3.28)$$

Let $\boldsymbol{M_n}$ be the one-sided normal derivative operator such that $\boldsymbol{M_n}\boldsymbol{\Phi} = \boldsymbol{r}$. It is now possible to write

$$\boldsymbol{M_n}\boldsymbol{\Phi} = \boldsymbol{r} = \boldsymbol{M_n}\boldsymbol{L}^{-1}\boldsymbol{A_0}\boldsymbol{r} + \boldsymbol{M_n}\boldsymbol{L}^{-1}\boldsymbol{B_0}. \tag{3.29}$$

Equation (3.29) clearly shows that the normal electric field, $\boldsymbol{r}$, has two linear contributions. These is a contribution from the trans-membrane potential at previous times and a contribution from the normal electric field itself. As the quantity $\boldsymbol{B_0}$ is known, that particular contribution can be explicitly calculated as

$$\boldsymbol{r}_0 = \boldsymbol{M_n}\boldsymbol{L}^{-1}\boldsymbol{B_0}, \tag{3.30}$$

which is simply the solution of the electric potential field using only the contribution to the jump conditions from $\boldsymbol{V}_m^n$ and $\boldsymbol{V}_m^{n-1}$ (*i.e.* the jump conditions in Eqs. (3.23)-(3.25) are computed with $\boldsymbol{r} = 0$). This electric potential solution is then projected onto the normal electric field space through the $\boldsymbol{M_n}$ operator.

The second contribution is from the still-unknown normal electric field, $\boldsymbol{r}$. This contribution, though, can be written as $\boldsymbol{M_n}\boldsymbol{L}^{-1}\boldsymbol{A_0}\boldsymbol{r} = \boldsymbol{A}\boldsymbol{r}$, where $\boldsymbol{A}\boldsymbol{r}$ is the solution of the electric potential projected onto the normal electric field space by only considering the $\boldsymbol{r}$ contributions to the jump conditions.

Using this simplified notation it can be stated that $\boldsymbol{r}$ is the solution to the following linear system,

$$(\boldsymbol{A} - \boldsymbol{I})\boldsymbol{r} = -\boldsymbol{r_0}. \tag{3.31}$$

As this linear system can not be written in explicit form, a matrix-free iterative linear system solution method is needed to obtain the solution. The quantity $\boldsymbol{r}$ is only defined on the interface and is thus a lower dimension than the computational domain. Therefore a solver such as GMRES proves to be an excellent choice.

To complete this section a word needs to be said about computing the normal electric potential derivative, $r = M\Phi$, and the calculation of surface Laplacian,

33

$\nabla_s^2 [\Phi] = -\nabla_s^2 V_m$, at a point on the interface. First consider the surface Laplacian of the trans-membrane potential. The trans-membrane voltage is only given on the interface. To facilitate calculations V_m is extended in the normal direction into the embedding region near the interface. It has been shown that standard Cartesian derivatives are equal to surface derivatives if the quantity of interest is constant in the normal direction, see the Closest Point Method for more details [49].

Next, let I_3^Φ be a bi-cubic (in 2D) or tri-cubic (in 3D) interpolant of the electric potential for the cell containing the interface point of interest, see Fig. 3.2. The normal derivative operator M can be calculated as appropriate derivatives of the interpolant and the outward unit normal, $M := \boldsymbol{n} \cdot \nabla I_3^\Phi$. To calculate a normal derivative in a particular fluid it is simply necessary to apply the corrections to the *opposite* fluid's nodes, *e.g.* if $r = \partial\Phi^+/\partial n$ the corrections would be applied to all nodes in the Ω^- fluid. In this way a particular fluid's normal electric field can be calculated and discontinuities in the field can be taken into account.

It should be noted that a similar scheme to model the electrohydrodynamics of a leaky dielectric drop has recently been presented [25]. Unlike a vesicle, a drop in the presence of an electric field does not have an electric potential jump across the interface. Thus the jump in electric potential is not evolving in time and is set to zero.

To sum up, assuming that the electric potential at the previous two time-steps are known the overall algorithm is given as:

Step I: Solve for the electric potential field only using corrections due to V_m^n and V_m^{n-1}: $\boldsymbol{\Phi_0} = \boldsymbol{L^{-1} B_0}$ using the given physical boundary conditions.

Step II: Compute the constant contribution to the normal electric field as $\boldsymbol{r_0} = \boldsymbol{M \Phi_0}$.

Step III: Use a matrix-free iterative solver such as GMRES to solve

$(\boldsymbol{A} - \boldsymbol{I})\,\boldsymbol{r} = -\boldsymbol{r}_0$. Each matrix-vector product $(\boldsymbol{A} - \boldsymbol{I})\,\boldsymbol{r}$ requires the following steps:

Step 1: Solve for the electric potential using the given $\boldsymbol{r}$: $\boldsymbol{\Phi}_r = \boldsymbol{L}^{-1}\boldsymbol{A_0}\boldsymbol{r}$ using uniform boundary conditions of $\boldsymbol{\Phi}_r|_{bc} = 0$.

Step 2: Calculate the normal electric field as $\boldsymbol{A}\boldsymbol{r} = \boldsymbol{M}\boldsymbol{\Phi}_r$.

Step 3: Return the quantity $\boldsymbol{A}\boldsymbol{r} - \boldsymbol{r}$ as the matrix-vector product.

Step IV: The electric potential field in the computational domain is $\boldsymbol{\Phi}^{n+1} = \boldsymbol{\Phi}_0 + \boldsymbol{\Phi}_r$.

Step V: The new trans-membrane potential is updated using Eq. (3.11).

3.2   Sample results

In this section the convergence, accuracy and robustness of the novel Immersed Interface method is investigated through various numerical experiments. In particular, convergence results are presented demonstrating the accuracy of the method. Both single time-step and multi-time-step convergence are considered. Additionally, the number of GMRES iterations needed to obtain convergence is also investigated. In the next step to validate the code, the method is compared to an analytic solution based on spherical harmonics and verifies the second-order accuracy of the underlying discretization even in the presence of solution discontinuities. Finally, a qualitative study is presented to illustrate the change of domain and trans-membrane potentials over time for an ellipsoidal vesicle in the presence of a uniform DC electric field.

3.2.1 Convergence results

Time-Varying Convergence

Consider a spherical vesicle of radius one centered at the origin. The physical domain is a $[-2, 2]^3$ cube. The conductivities of the regions are set to be $s^- = 50.0$ in the inner region and $s^+ = 1.0$ in the outer region. For simplicity, the membrane capacitance and conductance are both set to $C_m = G_m = 1.0$. The relative convergence tolerance for all iterative linear system solvers is set to 10^{-5}. To examine the accuracy of the underlying discretization of the problem, a well-behaved time-dependent solution of the electric potential field is developed. This analytic solution was created to satisfy the field equations and all jump conditions. The exact solution of the electric potential and trans-membrane potential are taken to be

$$\Phi^- = \frac{exp(-t)}{s^-}(3x^2 - y^2 - 2z^2), \tag{3.32}$$

$$\Phi^+ = exp(-t)(3x^2 - y^2 - 2z^2), \tag{3.33}$$

$$V_m = \frac{exp(-t)}{s^-}(3x^2 - y^2 - 2z^2) - exp(-t)(3x^2 - y^2 - 2z^2). \tag{3.34}$$

The initial trans-membrane potential is given as

$$V_0 = V_m(t = 0) = \frac{(3x^2 - y^2 - 2z^2)}{s^-} - (3x^2 - y^2 - 2z^2). \tag{3.35}$$

A Dirichlet boundary condition of $\Phi_{bc} = \phi^+$ is imposed on the domain boundaries. The errors at a final time of 0.375 are shown in Tables (3.1) and (3.2). Overall the domain electric potential observes second-order convergence in the L_∞-norm error while the trans-membrane potential has a slightly higher accuracy. This matches the underlying second-order finite difference approximation of the spatial derivatives. It is important to note that the extension of the jumps need to be calculated to third order accuracy to ensure that irregular nodes have a local truncation error of O(h).

Table 3.1: Domain Potential (Φ) error for a sphere on the domain $[-2, 2]^3$ for a time-varying function. The time step is $\Delta t = h$ while the final time is $T_{final} = 0.375$.

N	L_2	Order	L_∞	Order
33	2.53×10^{-6}	-	4.52×10^{-3}	-
65	2.39×10^{-7}	3.40	1.19×10^{-3}	1.98
129	2.26×10^{-8}	3.40	3.15×10^{-4}	1.99
257	1.98×10^{-9}	3.51	8.08×10^{-5}	2.01

Table 3.2: Trans-membrane potential(V_m) error for a sphere on the domain $[-2, 2]^3$ for a time-varying function. The time step is $\Delta t = h$ while the final time is $T_{final} = 0.375$.

N	L_2	Order	L_∞	Order
33	5.38×10^{-6}	-	5.81×10^{-3}	-
65	3.56×10^{-7}	3.92	1.36×10^{-3}	2.81
129	2.31×10^{-8}	3.94	3.34×10^{-4}	2.84
257	1.48×10^{-9}	3.96	8.56×10^{-5}	2.26

Despite this lower local truncation error, the overall method will retain the second-order accuracy of the underlying discretization. If the second-normal derivative jump is not taken into account, the local truncation error for irregular nodes will be reduced to O(1) and the overall scheme would only be first-order [43, 23, 3].

One possible limitation of the method is the number of GMRES iterations. As each matrix-vector product requires the solution of a linear system, a large number of GMRES iterations would result in an extremely computationally expensive method. In Fig (3.3) the number of GMRES iterations versus the time step for the example in this section are provided. In all cases the number of GMRES iterations remains between three and six, regardless of the grid size. While this is not a complete test it appears that the number of GMRES iterations slightly decreases as the mesh size decreases.

Validation of the method

Consider a spherical vesicle placed in an electric field in the absence of membrane conductivity, $G_m = 0$. In this simple case an analytic solution exists for the electric
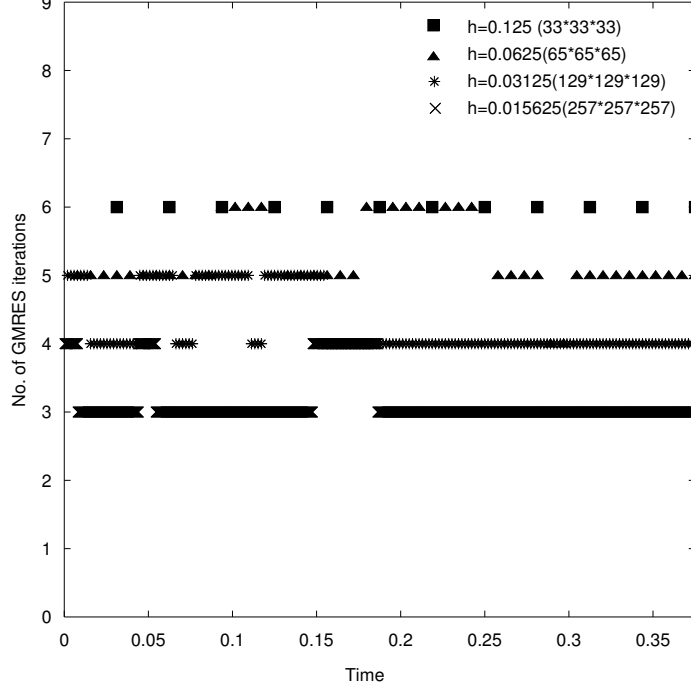
Figure 3.3: The number of GMRES iterations versus time for different mesh sizes.

potential and trans-membrane potential [79]. Let the electric field far from the vesicle be given by $\boldsymbol{E}^{\infty} = E_0\hat{\boldsymbol{y}}$. The electric potential can be written in terms of spherical harmonics: $\Phi^{\pm} = -E_0 \left(Y_1^{-1} + Y_1^1\right) P^{\pm}$, where $Y_1^{\pm 1}$ are the first-order spherical harmonic modes and $P^{\pm}$ is a function of the membrane capacitance C_m, the conductivity ratio between the inner and outer fluids, $\Lambda = s^-/s^+$, and time, t. The trans-membrane potential has a solution of $V_m = \bar{V}(t)E_0 \left(Y_1^{-1} + Y_1^1\right)$ where $\bar{V}(t) \sim 1 - exp(-t)$. See Ref. [79] for details of solution.

Using a conductivity ratio of $\Lambda = 0.1$, membrane capacitance of $C_m = 1$, and an external electric field strength of $E_0 = 1$ the time-evolution of the electric potential field and trans-membrane potential in $\Omega = \Omega^- \cup \Omega^+$ for a spherical vesicles of radius 1 has been calculated up to a time of $t = 20$. The domain spans the region $[-4, 4]^3$ and Dirichlet boundary conditions are imposed on the computational domain boundary. Convergence results for grid spacing ranging from $h = 0.0313$ to $h = 0.125$ using a time step of $\Delta t = h$ are reported in Table 3.3. The electric potential, trans-membrane

potential, and normal electric field (r in the numerical method) are all consistently second-order accurate in the L_∞-norm error.

Table 3.3: Convergence results for the electric potential, trans-membrane potential, and electric field normal to the interface for a spherical vesicle of radius 1. The normalized inner fluid conductivity is 0.1 while the outer fluid conductivity is set to 1. The membrane capacitance is set to $C_m = 1$ while the conductivity is $G_m = 0$. The external electric field has strength of $E_0 = 1$. The vesicle is placed in a $[-4,4]^3$ domain while the time step is fixed as $\Delta t = h$. All errors are computed at a time of $t = 20$. Comparison is done against analytical results of Schwalbe *et al.* [79]

	Electric Potential		Trans-Membrane Potential		Normal Electric Field	
h	L_∞	Order	L_∞	Order	L_∞	Order
0.1250	4.5134×10^{-3}	-	3.9191×10^{-3}	-	8.8146×10^{-4}	-
0.0833	2.0335×10^{-3}	1.89	1.7681×10^{-3}	1.93	3.8786×10^{-4}	2.4
0.0625	1.1690×10^{-3}	1.82	1.0209×10^{-3}	1.86	2.0215×10^{-4}	2.22
0.0417	5.1347×10^{-4}	1.89	4.4380×10^{-4}	1.93	8.6623×10^{-5}	2.34
0.0313	3.0121×10^{-4}	1.85	2.6004×10^{-4}	1.88	5.1190×10^{-5}	2.25

Ellipsoidal vesicle in presence of uniform DC field

As an example of solving the system for a non-spherical shape consider an ellipsoidal shape with an axis length of 3.7 in the $\hat{y}$-direction and an axis lengths of 1.33 in the $\hat{x}$- and $\hat{z}$-directions. The electric field is in the $\hat{y}$-direction and has a far-field strength of 1. The membrane capacitance is set to $C_m = 1$ while the conductivity is set to a small, but non-zero value, $G_m = 0.001$.

In this case the inner fluid conductivity is set to $s^- = 0.05$ while the outer conductivity is unity, $s^+ = 1$. The time-evolution of the electric potential on the $z = 0$ plane and the evolution of the trans-membrane potential are shown in Fig. 3.4. Over time the trans-membrane saturates between values of -2 and +2 and the potential of the inner fluid flattens out, which matches what is expected for vesicles [79].

t=0   t=46.875   t=187.5
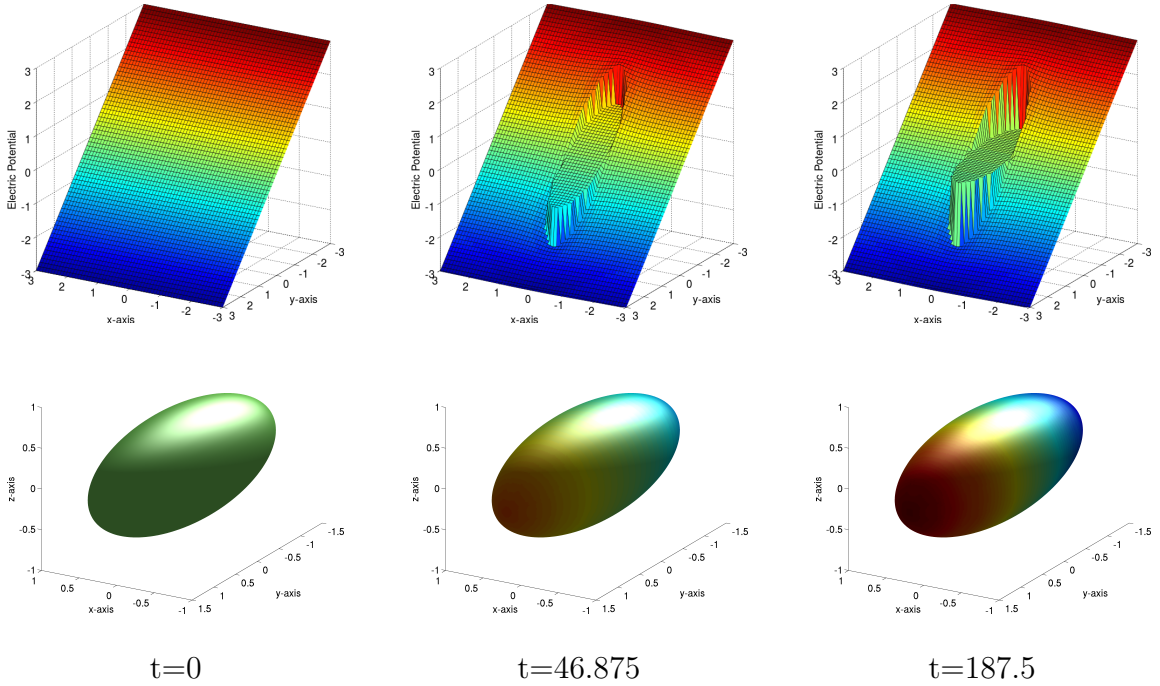
Figure 3.4: Sample results for an elliptic interface in an electric field. The top row are for the $z = 0$ plane while the bottom row is the trans-membrane potential. The trans-membrane potential has values between -2 (blue) to +2 (red).

Chapter 4

Interface Tracking

Many of the equations given in Chapter 2 require high order geometric quantities, such as the curvature. To ensure that surface quantities are smooth a semi-implicit level set advection scheme is utilized. This chapter outlines the numerical implementation of the level set method for the evolution of the stiff interface in the vesicle simulation. First the standard semi-implicit level set method and the original gradient augmented level set method are separately described. The proposed combination of these two methods then follows. This includes the complete algorithm of the novel semi-implicit gradient augmented level set method along with sample results of mean curvature and surface diffusion flows in both two and three dimensions. The content of this chapter was published in the *SIAM Journal on Scientific Computing* [32].

The original third-order gradient augmented method has been recently generalized to an arbitrary order under the name of jet schemes [80]. The possibility of extending the idea of using the semi-implicit formulation for the generalized formulation of jet schemes is discussed at the end of this chapter.

4.1 The Original Semi-Implicit Formulation

The level set advection equation previously given in Eq. (2.22), can be written as a Hamilton-Jacobi equation,

$$\frac{\partial \phi}{\partial t} + H\left(\boldsymbol{x}, t, \phi, \nabla \phi\right) = 0. \tag{4.1}$$

A Hamilton-Jacobi equation can be semi-discretized in time in a semi-implicit fashion one of two ways. The first is to extract the linear portion of the Hamiltonian, $H\left(\boldsymbol{x}, t, \phi, \nabla \phi\right)$, and treat it implicitly,

$$\frac{\partial \phi}{\partial t} + L\left(\boldsymbol{x}, t^{n+1}, \phi^{n+1}, \nabla \phi^{n+1}\right) + N\left(\boldsymbol{x}, t^n, \phi^n, \nabla \phi^n\right) = 0, \tag{4.2}$$

where L is the linear portion and N is the nonlinear portion such that $H = L + N$. If it is not possible to explicitly extract the linear portion one can always determine an approximation to the linear portion and solve the following semi-implicit equation,

$$\frac{\partial \phi}{\partial t} + H\left(\boldsymbol{x}, t^n, \phi^n, \nabla \phi^n\right) - \widetilde{L}\left(\boldsymbol{x}, t^n, \phi^n, \nabla \phi^n\right) + \widetilde{L}\left(\boldsymbol{x}, t^{n+1}, \phi^{n+1}, \nabla \phi^{n+1}\right) = 0, \quad (4.3)$$

where $\widetilde{L}$ is the approximate linear portion. For mean curvature based flows it is typical to take $\widetilde{L} = \beta \nabla^2 \phi$ while for surface diffusion based flows $\widetilde{L} = -\beta \nabla^4 \phi$, where β is a constant. Previous works with the semi-implicit level set method have shown that a value of $\beta = 1/2$ results in a stable scheme for many different situations and time steps [73, 87]. This additional smoothing allows the semi-implicit level set method to utilize larger time steps than is possible with an explicit scheme [87]. For example, the motion by surface diffusion of a seven-lobed star was demonstrated using an explicit scheme [16] with a CFL condition of $\Delta t / h^4 \approx 0.25$ compared to a CFL condition of $\Delta t / h^4 \approx 2 \times 10^4$ for a semi-implicit scheme [87].

4.2 The Original Gradient Augmented Method

The gradient augmented level set method, first introduced by Nave, Rosales and Seibold [56], is an extension of the standard level set method which advects both the level set function, ϕ, and the gradient vector field, $\boldsymbol{\psi} = \nabla\phi = (\psi^x, \psi^y, \psi^z)$, see Eqs. (2.22) and (2.23). The inclusion of gradient information allows for the determination of sub-grid information. Take as an example two grid points, $x_0 = 0$ and $x_1 = 1$, on a one dimensional grid with $\phi(x_0) = \phi(x_1) = 0.1$ with $\phi_x(x_0) = 1$ and $\phi_x(x_1) = -1$. The exact level set, the signed distance function, gives an interface ($\phi = 0$) at points $x = 0.1$ and 0.9. Using only the level set values linear interpolation does not return any interface points in this domain. The additional gradient information allows for the determination of a Hermite interpolant giving interface locations of $x \approx 0.112$ and $x \approx 0.887$. See Fig. 4.1 for a graphical representation.
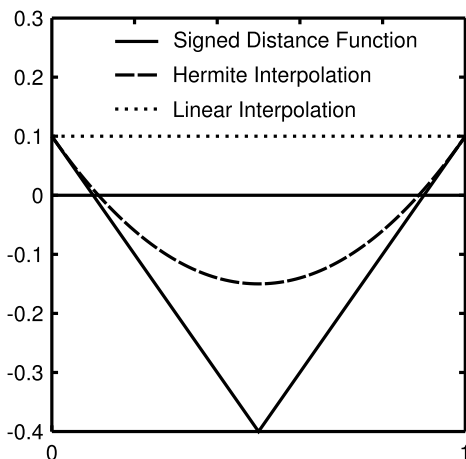
Figure 4.1: A one-dimensional grid with data provided at grid points $x = 0$ and $x = 1$. The linear interpolant misses the interface existing between the two grid points. The Hermite interpolant determined using the additional gradient information finds two interfaces close to the true interface locations.

To ensure that the level set function and gradient field remain coupled throughout time Eqs. (2.22) and (2.23) are advanced in a coherent and fully coupled manner [56].

$$
\begin{cases}
\frac{\partial \phi}{\partial t} + \boldsymbol{u} \cdot \nabla \phi = 0. \\
\frac{\partial \boldsymbol{\psi}}{\partial t} + \boldsymbol{u} \cdot \nabla \boldsymbol{\psi} + \nabla \boldsymbol{u} \cdot \boldsymbol{\psi} = 0.
\end{cases}
\tag{4.4}
$$

Lagrangian techniques are used to trace characteristics back in time to determine departure locations. Using the available information a Hermite interpolating polynomial is calculated and utilized to determine the departure values for the level set function and gradient functions. To first-order in time this results in the following scheme,

$$
\boldsymbol{x}_d = \boldsymbol{x} - \Delta t \, \boldsymbol{u}\left(\boldsymbol{x}, t\right),
\tag{4.5}
$$

$$
\nabla \boldsymbol{x}_d = \boldsymbol{I} - \Delta t \, \nabla \boldsymbol{u}\left(\boldsymbol{x}, t\right),
\tag{4.6}
$$

$$
\phi\left(\boldsymbol{x}, t\right) = P\left(\boldsymbol{x}_d, t - \Delta t\right),
\tag{4.7}
$$

$$
\boldsymbol{\psi}\left(\boldsymbol{x}, t\right) = \nabla \boldsymbol{x}_d \cdot \boldsymbol{G}\left(\boldsymbol{x}_d, t - \Delta t\right),
\tag{4.8}
$$

where $P(\boldsymbol{x}, t)$ is the Hermite interpolating polynomial of ϕ at a time t, $\boldsymbol{G} = \nabla P$ is the gradient of the Hermite interpolant defined for the level set function, while $\boldsymbol{x}_d$ and $\nabla \boldsymbol{x}_d$ are the departure location and "departure" gradient, respectively. It is important to note that since the solutions of the underlying PDE are sufficiently smooth here, the first order approximation of characteristic curves in time is consistent. However a similar splitting for equations with shocks may lead to wrong entropy solutions and therefore use of high resolution methods such as high order TVD schemes will be needed [60].

Implementing a third-order version of the method Nave, Rosales and Seibold demonstrated that for analytic flow fields the gradient augmented method is of com-

parable quality to weighted essential non-oscillatory (WENO) schemes but with optimally local stencils. A more recent work by Chidyagwai *et. al.* demonstrates that for a given grid size a WENO scheme is less computationally expensive than a gradient augmented scheme [14]. However, the overall grid size to achieve a particular accuracy level is larger for a gradient augmented level set method than a WENO scheme. It was demonstrated that for a given accuracy the gradient augmented level set method is less computationally expensive than a WENO scheme. In general gradient augmented schemes are more computationally efficient than comparable WENO schemes. In both of these gradient augmented works results for flows depending on derivatives of the level set function where not presented.

4.3   A semi-implicit gradient augmented level set method

The original gradient augmented level set method is only applicable to linear advection equations. For nonlinear curvature-based flows such as vesicle simulation, it is not possible to take time steps on the order of the grid spacing, as it is with general semi-implicit methods. This issue is addressed by introducing a semi-implicit gradient augmented level set method. This method is a combination of the methods explained in Secs. 4.1 and 4.2. The goal is to combine the additional accuracy afforded by explicitly tracking gradient information with the stability properties of a semi-implicit scheme. The system of equations in Eq.(4.4) is rewritten as

$$
\begin{cases}
\frac{D\phi}{Dt} + \beta L\phi - \beta L\phi = 0, \\
\frac{D\boldsymbol{\psi}}{Dt} + \nabla \boldsymbol{u} \cdot \boldsymbol{\psi} + \beta L\boldsymbol{\psi} - \beta L\boldsymbol{\psi} = 0.
\end{cases}
\tag{4.9}
$$

where D/Dt is the material (Lagrangian) derivative, L is a linear operator, and β is a constant. To first-order in time this can be written as

$$\boldsymbol{x}_d = \boldsymbol{x} - \Delta t \, \boldsymbol{u}\left(\boldsymbol{x}, t\right), \tag{4.10}$$

$$\nabla \boldsymbol{x}_d = \boldsymbol{I} - \Delta t \, \nabla \boldsymbol{u}\left(\boldsymbol{x}, t\right), \tag{4.11}$$

$$\widetilde{\phi} = P\left(\boldsymbol{x}_d, t - \Delta t\right), \tag{4.12}$$

$$\widetilde{\boldsymbol{\psi}} = \nabla \boldsymbol{x}_d \cdot \boldsymbol{G}\left(\boldsymbol{x}_d, t - \Delta t\right), \tag{4.13}$$

$$\frac{\phi_{n+1} - \widetilde{\phi}}{\Delta t} = \beta L \phi_{n+1} - \beta L \phi_n, \tag{4.14}$$

$$\frac{\boldsymbol{\psi}_{n+1} - \widetilde{\boldsymbol{\psi}}}{\Delta t} = \beta L \boldsymbol{\psi}_{n+1} - \beta L \boldsymbol{\psi}_n, \tag{4.15}$$

The linear operator L is based on the underlying flow field. For mean curvature flow $L = \nabla^2$ while for surface diffusion $L = -\nabla^4$. If $\beta = 0$ the method results in the standard gradient augmented method. If instead of Eqs. 4.10 to 4.13 values are set as $\widetilde{\phi} = \phi_n$ and $\widetilde{\boldsymbol{\psi}} = \boldsymbol{\psi}_n$ the method gives the standard semi-implicit level set scheme.

The location $\boldsymbol{x}_d$ is obtained by tracing characteristics backwards in time. In general this location will not lie on a grid point and thus the use of an interpolant, P and $\boldsymbol{G} = \nabla P$, is required. In two dimensions let $\boldsymbol{x}_d$ lie within a grid cell $\Omega_{i,j}$ enclosing the region given by four grid points: $\boldsymbol{x}_{i,j}$, $\boldsymbol{x}_{i+1,j}$, $\boldsymbol{x}_{i,j+1}$, and $\boldsymbol{x}_{i+1,j+1}$. Using the value of the level set function, ϕ, and the gradient field, $\boldsymbol{\psi} = (\psi^x, \psi^y)$, at time $t - \Delta t$ it is possible to define the Hermite interpolant over the grid cell by requiring that $P(\boldsymbol{x}_{m,n}) = \phi_{m,n}$, $\partial_x P(\boldsymbol{x}_{m,n}) = \psi^x_{m,n}$, $\partial_y P(\boldsymbol{x}_{m,n}) = \psi^y_{m,n}$, and $\partial_{xy} P(\boldsymbol{x}_{m,n}) = \phi_{xy}$ for $m = i, i+1$ and $n = j, j+1$. In contrast to the gradient augmented method the inclusion of the smoothing term $\boldsymbol{L}$ in the semi-implicit formulation does not allow for a purely cell-based method. The derivative ϕ_{xy} is therefore chosen to enforce C^1 continuity across cell boundaries by setting $\phi_{xy} = (\partial_x \psi^y_{m,n} + \partial_y \psi^x_{m,n})/2$. The gradient interpolant is then defined as $\boldsymbol{G} = \nabla P$.

4.4 Level Set Reinitialization

A distance-based reinitialization procedure is done in each time step. This algorithm is employed here for two main reasons: first, the point on the interface with the shortest distance to a given grid point, called the closest-point, is required for the extension of surface quantities off the interface. Second, it has been shown that reinitialization aids in the conservation of mass in level set-based simulations [89]. The method employed here uses a variant of Newton's method and a tricubic interpolation to find the closest point on the interface from an arbitrary grid location in the neighborhood, see Ref. [15] for more details. Once the closest points are determined the level set function is replaced by the corresponding signed distance value while the gradient field is set to the unit outward normal vector, which is the normalized vector pointing from the closest point to the grid point, corrected so that it points outward. This procedure does not need to be done everywhere in the domain, but only near the interface. For the purpose of vesicle simulations all nodes within five grid points of the interface have their closest point calculated and explicitly reinitialized, see Fig. 4.2. The remaining nodes in the domain are reinitialized using a first-order PDE based reinitialization scheme [73, 87, 64],

$$\frac{\partial \phi}{\partial \tau} + \mathrm{sign}(\phi^0)(1- \mid \nabla \phi \mid) = 0, \tag{4.16}$$

where τ is a fictitious time, ϕ^0 is the original level set value which defines the interface and $\mathrm{sign}(x)$ is the standard sign function. The particular discretization chosen in this work is a first-order in time upwind scheme, see [64] for more details. For surface properties such as curvature, tension or values of trans-membrane potential in the electrohydrodynamic simulations which are normally defined only on the interface, an extension is needed to define the quantity at nodes in the vicinity of the interface. To determine smooth values of a surface quantity in a neighborhood of the interface,
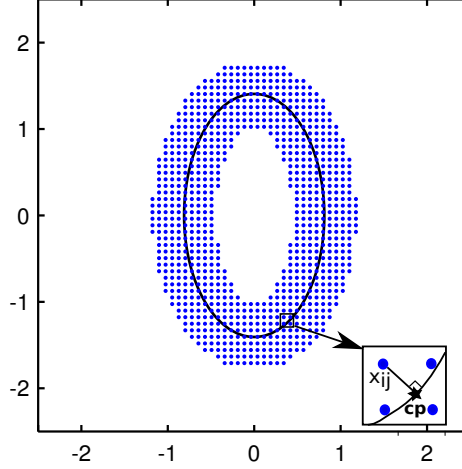
Figure 4.2: The closest point on the interface (cp) is the shortest distance to a given grid point. These values are calculated for all the nodes within $5h$ where h is the grid spacing.

values are extended away from the interface using the closest point values and the tri-cubic interpolat. Ultimately, given a velocity field, $\boldsymbol{u}$, the semi-implicit gradient augmented level set scheme described above can be summarized in the following algorithm:

Algorithm 1 Advance the Level Set function and Gradient Fields
---
Require: ϕ_n and $\boldsymbol{\psi}_n$.
  for every grid point in the domain **do**
    Compute the departure point $\boldsymbol{x}_d$ using Eq. 4.10.
    Compute the departure gradient $\nabla \boldsymbol{x}_d$ using Eq. 4.11
    Evaluate the tentative Lagrangian solutions $\widetilde{\phi}$ and $\widetilde{\boldsymbol{\psi}}$ by Eqs. (4.12) and (4.13).
  end for
  if velocity field is the surface diffusion $(vecv = (\nabla_s^2 \kappa)\,\boldsymbol{n})$ **then**
    Set $L = -\nabla^4$
  else
    Set $L = \nabla^2$
  end if
  Solve $(\boldsymbol{I} - \Delta t \beta L)\,\phi_{n+1} = \widetilde{\phi} - \Delta t \beta L \phi_n$.
  Solve $(\boldsymbol{I} - \Delta t \beta L)\,\boldsymbol{\psi}_{n+1} = \widetilde{\boldsymbol{\psi}} - \Delta t \beta L \boldsymbol{\psi}_n$.
  Reinitialize the level set and recalculate the closest point data
  return ϕ_{n+1} and $\boldsymbol{\psi}_{n+1}$.

4.5 Sample results

Before using the proposed method for the vesicle simulations, the robustness and the reliability of the algorithm is extensively tested for both two and three dimensional problems. Two different velocity field types are considered here. The first one is the mean curvature flow given by $u_n = -\kappa$ or $\boldsymbol{u} = -\kappa\boldsymbol{n}$, where the mean curvature, κ, is equal to half of the total curvature, H, defined in chapter 2 and $\boldsymbol{n}$ is the unit normal vector. Volume-preserving mean curvature flow given by $\boldsymbol{u} = (\kappa - \kappa_{ave})\boldsymbol{n}$, where κ_{avg} is the average curvature in the domain, will also be considered.

The unit normal vector is simply given as the normalized gradient vector:

$$\boldsymbol{n} = \frac{\boldsymbol{\psi}}{\|\boldsymbol{\psi}\|}. \tag{4.17}$$

In two dimensions the curvature is computed as

$$\kappa = \frac{\phi_{xx}(\psi^y)^2 + \phi_{yy}(\psi^x)^2 - 2\phi_{xy}\psi^x\psi^y}{\left((\psi^x)^2 + (\psi^y)^2 + \epsilon\right)^{3/2}} \tag{4.18}$$

while for three-dimensional flows

$$
\begin{aligned}
\kappa = & \left(\phi_{xx}\left((\psi^y)^2 + (\psi^z)^2\right) + \phi_{yy}\left((\psi^x)^2 + (\psi^z)^2\right) + \phi_{zz}\left((\psi^x)^2 + (\psi^y)^2\right)\right. \\
& \left. - 2\phi_{xy}\psi^x\psi^y - 2\phi_{xz}\psi^x\psi^x - 2\phi_{yz}\psi^y\psi^z\right) / \left((\psi^x)^2 + (\psi^y)^2 + (\psi^z)^2 + \epsilon\right)^{3/2}, \quad \tag{4.19}
\end{aligned}
$$

where $\epsilon = 10^{-8}$ is added to the denominator to ensure that no division by zero will occur. The second-order derivatives are obtained by first derivatives of the $\boldsymbol{\psi}$ vector, i.e. $\phi_{xx} = \partial_x\psi^x$. Any cross derivatives are averages of the two possible first derivatives of the gradient vector, i.e. $\phi_{xy} = (\partial_x\psi^y + \partial_y\psi^x)/2$. It is worthwhile to mention that in the original gradient augmented level set method analytic differentiation of interpolant is proposed as a method to calculate differential quantities such as curvature [56]. This has the advantage of optimal locality when it comes to calculation of differential

quantities inside grid cells. However, in this work curvature-dependent quantities are only calculated at grid points. Therefore values can be obtained by finite difference approximations of function values and gradient information. Indeed, one can easily show that analytical differentiation of a bi-cubic interpolant determined using the ϕ_{xy} given above and second-order finite difference approximations provide the same result when the calculation is performed at grid points.

The second velocity field considered is that of surface diffusion, given by $u_n = \nabla_s^2 \kappa$ or $\boldsymbol{u} = (\nabla_s^2 \kappa)\, \boldsymbol{n}$ where ∇_s^2 is the surface Laplacian. Assume that the curvature is known in the vicinity of the interface. In two dimensions the surface Laplacian of the curvature can then be calculated as

$$S = \nabla_s^2 \kappa = \frac{\kappa_{xx}(\psi^y)^2 + \kappa_{yy}(\psi^x)^2 - 2\kappa_{xy}\psi^x\psi^y}{(\psi^x)^2 + (\psi^y)^2 + \epsilon} - \kappa \frac{\kappa_x \psi^x + \kappa_y \psi^y}{\sqrt{(\psi^x)^2 + (\psi^y)^2 + \epsilon}}, \qquad (4.20)$$

while for the three-dimensional case

$$\begin{aligned}
S = \nabla_s^2 \kappa =& (\kappa_{xx}\left((\psi^y)^2 + (\psi^z)^2\right) + \kappa_{yy}\left((\psi^x)^2 + (\psi^z)^2\right) + \kappa_{zz}\left((\psi^x)^2 + (\psi^y)^2\right) \\
& - 2\kappa_{xy}\psi^x\psi^y - 2\kappa_{xz}\psi^x\psi^z - 2\kappa_{yz}\psi^y\psi^z)/((\psi^x)^2 + (\psi^y)^2 + (\psi^z)^2 + \epsilon) \\
& - \kappa(\kappa_x\psi^x + \kappa_y\psi^y + \kappa_z\psi^z)/\sqrt{(\psi^x)^2 + (\psi^y)^2 + (\psi^z)^2 + \epsilon}. \qquad (4.21)
\end{aligned}$$

The results are obtained by a first-order in time discretization. Spatial derivatives are calculated using second-order isotropic finite differences [35, 63]. The linear systems in Eqs. (4.14) and (4.15) are solved using a standard Bi-CGSTAB method [92, 69]. In each case periodic boundary conditions are assumed. Based on experience and previous works a constant of $\beta = 1/2$ is used [73]. Further justification of $\beta = 1/2$ is provided in Sec. 4.5.5. The curvature and surface Laplacian of curvature are first calculated near the interface and then extended to the rest of the domain using the closest point calculations. The time step is given by Δt while the uniform grid spacing is given by h.

Every simulation begins with an interface described by a signed distance function. To obtain some of the interfaces it is necessary to begin with either a non-signed distance function or a parametric representation. If the initial shape is described by a non-signed distance level set function $\tilde{\phi}$ an equivalent signed distance level set is obtained by doing the reinitialization process.

4.5.1 Mean Curvature Flow

Here the evolution of two- and three-dimensional interfaces under mean-curvature flow is shown. For all cases in this section the velocity of the interface is given by $\boldsymbol{u} = -\kappa\boldsymbol{n}$.

First consider a circular interface. With mean curvature flow a circular interface beginning with an initial radius of r_0 will collapse uniformly. A sample result is presented in Fig. 4.3 for a grid spacing of $h = 0.0625$ and a time step of $\Delta t = 4h^2 = 0.015625$.
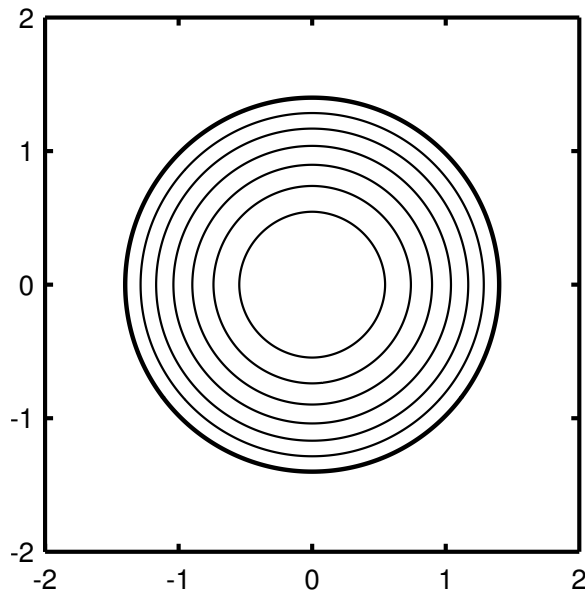
Figure 4.3: A circle collapsing due to mean curvature flow. The initial interface is represented by the thick line. The the grid spacing is $h = 0.0625$ and the time step is $\Delta t = 4h^2 = 0.015625$. The interface is shown in time increments of $10\Delta t$.

The collapse of a circular interface under mean curvature flow is a situation with a known analytic solution and thus allows for the investigation of the accuracy of the semi-implicit gradient augmented scheme. At time t the radius of the circle is given by

$$r(t) = \sqrt{r_0^2 - 2t}, \tag{4.22}$$

where r_0 is the initial radius. The interface is allowed to evolve until a time of $t = 0.375$ with various grid spacings and a time step set to $\Delta t = 8h^2$. To measure error the level set function and the gradient field values for the region defined by $0.375 \leq \sqrt{x^2 + y^2} \leq 0.625$ is compared to the analytic signed distance function for a circle with the radius given by Eq. (4.22).

The resulting errors are shown in Tables 4.1 and 4.2. Overall both the level set function and gradient field observe third-order L_2-norm and second-order L_∞-norm convergence. This should be expected as the smoothing term, L in Eqs. (4.14) and (4.15), is discretized using second-order finite differences. Additionally, the time step scales as h^2 to match the spatial discretization. Thus it should not be expected that the third-order convergence in the L_∞-norm, as observed in the original gradient augmented level set method [56, 80], be obtainable using the current discretization. In fact, let the order of the time discretization be $\mathcal{O}(\Delta t^m)$, the order of the smoothing term be $\mathcal{O}(h^L)$, and the order of the interpolant used for the Lagrangian step Eqs. (4.10) and (4.11) be $\mathcal{O}(h^p)$. It should then be expected that the overall error will scale as $\mathcal{O}(\Delta t^m) + \mathcal{O}(h^L) + \mathcal{O}(h^p) = \mathcal{O}(h^{\min(L,p)})$ assuming that the temporal order m scales as $\min(L, p)$. Using higher-order approximations for the smoothing term and the time-derivative should result in the same accuracy as the original gradient augmented method.

Now consider the behavior of more complex interfaces. The collapse of a two-dimensional Cassini Oval given by $m = a^2 \cos 2\theta + \sqrt{b^4 - a^4 + a^4 \cos^2(2\theta)}$, $x(\theta) = \sqrt{m} \cos \theta$, and $y(\theta) = \sqrt{m} \sin \theta$ where $0 \leq \theta < 2\pi$ with $a = 1.29$ and $b = 1.3$ is shown

Table 4.1: Level set error for a circle on the domain $[-2, 2] \times [-2, 2]$ with $v_n = -\kappa$ using $\Delta t = 8h^2$.

N	L_2	Order	L_∞	Order
65	8.40×10^{-4}		1.19×10^{-2}	
129	1.02×10^{-4}	3.04	2.98×10^{-3}	1.99
193	2.94×10^{-5}	3.07	1.26×10^{-3}	2.12
257	1.11×10^{-5}	3.39	6.35×10^{-4}	2.38
385	3.51×10^{-6}	2.84	3.11×10^{-4}	1.76
513	1.40×10^{-6}	3.19	1.99×10^{-4}	1.55

Table 4.2: Gradient error for a circle with $v_n = -\kappa$ using $\Delta t = 8h^2$.

N	L_2	Order	L_∞	Order
65	2.19×10^{-4}		5.85×10^{-3}	
129	3.53×10^{-5}	2.63	1.55×10^{-3}	1.92
193	9.73×10^{-6}	3.18	8.08×10^{-4}	1.61
257	4.14×10^{-6}	2.97	4.55×10^{-4}	2.00
385	1.10×10^{-6}	3.26	2.20×10^{-4}	1.79
513	5.65×10^{-7}	2.32	1.33×10^{-4}	1.75

in Fig. 4.4. For this example the CFL condition is $\Delta t/h^2 \approx 30$. Initially the interface has regions of both positive and negative curvature. The positive curvature regions move towards the center of the domain while those with negative curvature move away from the center. After some time an ellipse-like interface is obtained. From this point forward the interface collapses to a point.
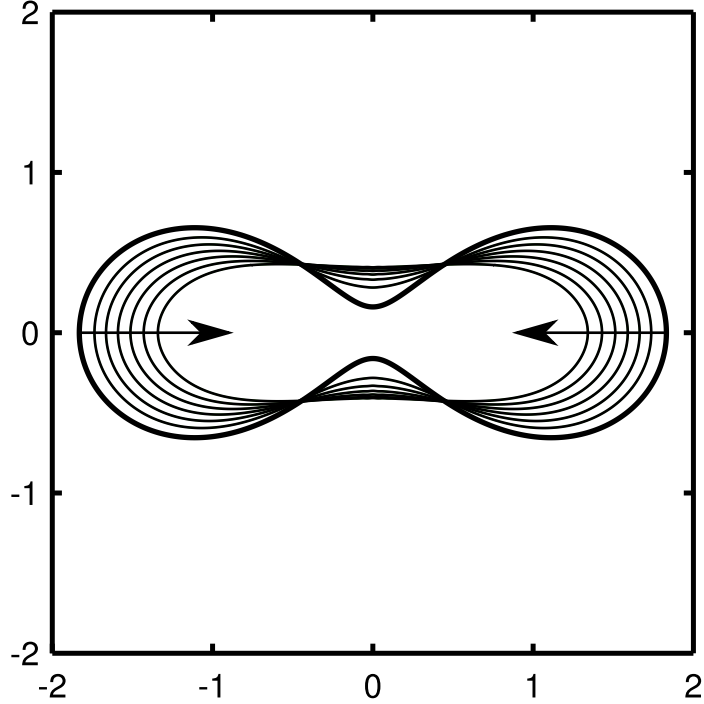
Figure 4.4: Motion by mean curvature for a Cassini oval at different times on a 128×128 grid. The grid spacing is $h = 0.03125$ while the time step is $\Delta t = 0.03 \approx 30h^2$. The thick line represents the initial interface while the arrow indicates the direction of motion. Subsequent interface locations are shown in time increments of $3\Delta t$. Eventually the interface collapses to a point.

Next consider a four-lobed star, Fig. 4.5. The initial shape is given by

$$r = r_0 + \Delta r \cos n\theta, \tag{4.23}$$

$$x(\theta) = r \cos \theta, \tag{4.24}$$

$$y(\theta) = r \sin \theta, \tag{4.25}$$

with $r_0 = 1.16$, $\Delta r = 0.55$, and $n = 4$. For this example $\Delta t/h^2 \approx 20$. As in the Cassini oval result shown above the interface evolves until the curvature is strictly positive at which point the shape collapses to a point.
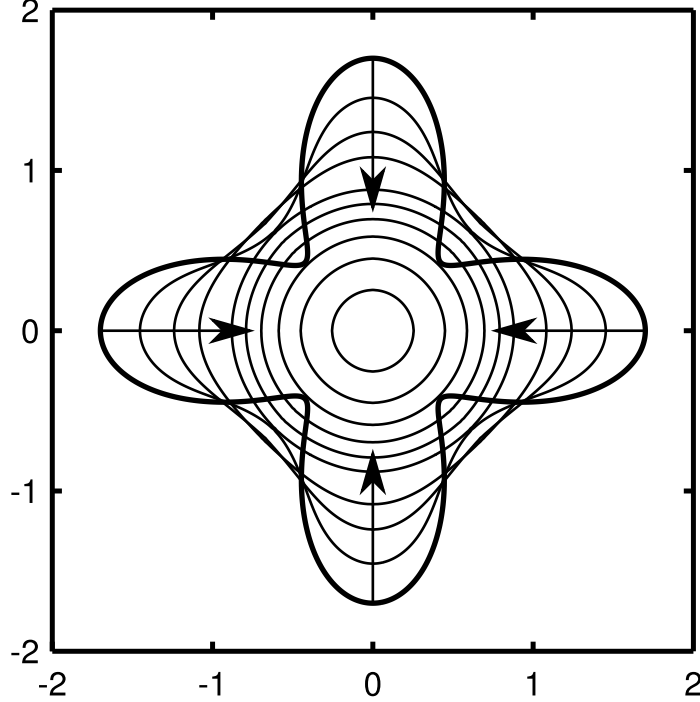
Figure 4.5: Evolution of a 4-lobe star under mean curvature flow. The grid size 256×256 giving a grid spacing of $h = 0.015625$. The time step is $\Delta t = 0.005 \approx 20h^2$. The thick line is the initial interface with subsequent interface locations shown in increments of $20\Delta t$. The arrows indicate the direction of motion.

To demonstrate the added stability properties of the semi-implicit gradient augmented scheme as compared to a fully explicit (*i.e.* $\beta = 0$) adaptation of the original gradient augmented level set method the evolution of a five-lobe star is shown in Fig. 4.6. The initial shape is provided by Eqs. (4.23)-(4.25) with $r_0 = 0.58$, $\Delta r = 0.28$ and $n = 5$. A common grid spacing of $h = 0.03125$ and time step $\Delta t = 5 \times 10^{-4}$ is used for both cases. This results in a CFL condition of $\Delta t / h^2 \approx 0.5$.

Over time the fully explicit adaptation of the GALS method begins to demonstrate numerical instabilities. The semi-implicit gradient augmented method does not demonstrate any instability and shows the expected behavior.
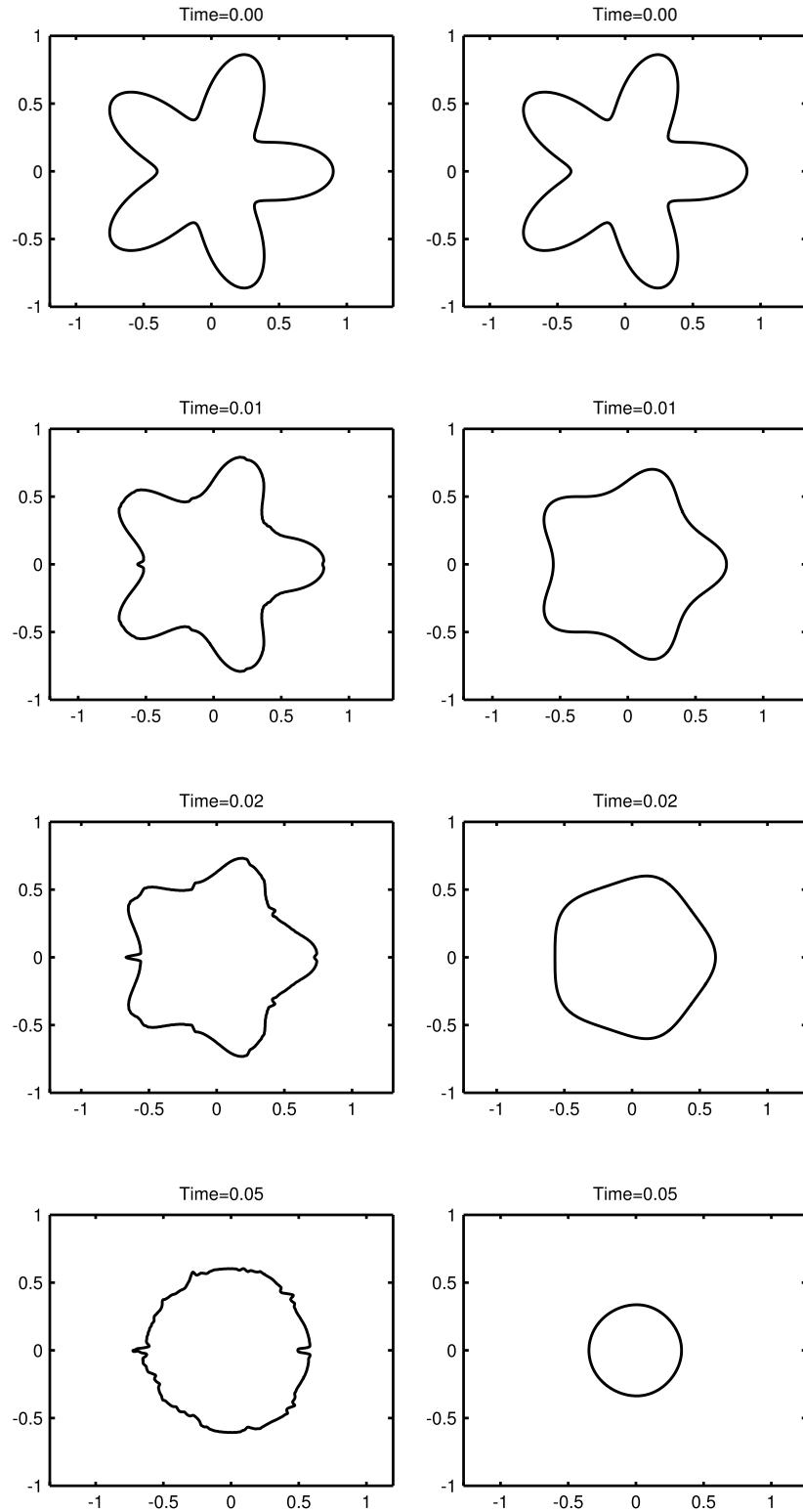
Figure 4.6: A comparison of the original gradient augmented method (left figures) with the semi-implicit augmented method (right figures) The 5-lobe star is collapsing under mean curvature flow, $u_n = -\kappa$, for $\Delta t = 5 \times 10^{-4}$, $h = 0.03125$ giving $\Delta t / h^2 \approx 0.5$. The domain size is $[-2, 2]^2$

56

The extension of the semi-implicit gradient augmented method to three dimensions is demonstrated in Fig. 4.7, which shows the collapse of a three-dimensional Cassini oval with mean-curvature flow. The initial shape of the interface is given by $\tilde{\phi} = ((x-a)^2 + y^2 + z^2)((x+a)^2 + y^2 + z^2) - b^4$ with $a = 1.29$ and $b = 1.3$. As mentioned above this initial level set function is replaced by a signed distance function using an initialization procedure.

(a) $t = 0$

(b) $t = 0.025$

(c) $t = 0.04$

(d) $t = 0.075$
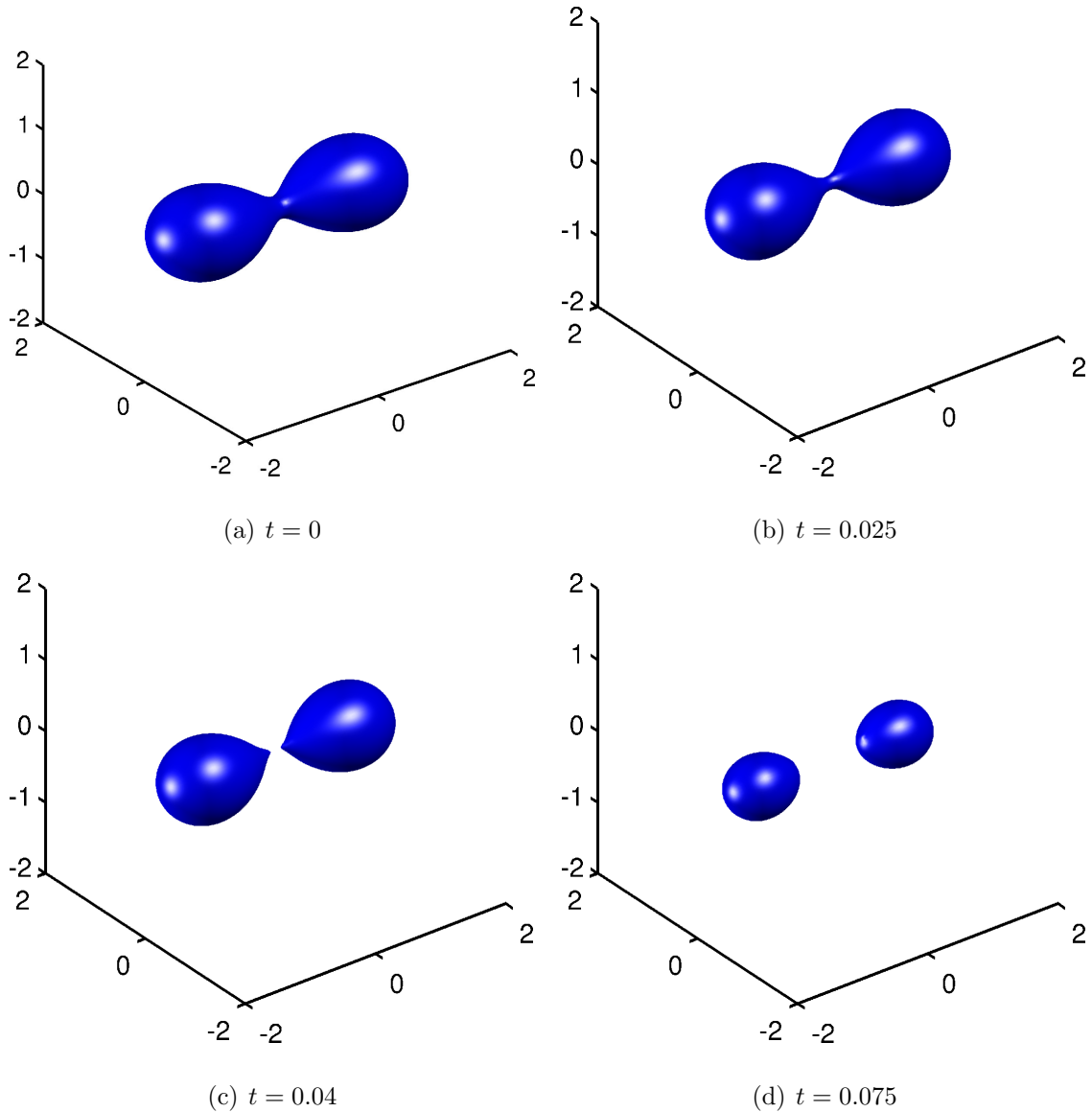
Figure 4.7: Collapse of a three dimensional Cassini oval under mean curvature flow for $h = 0.0625$ and $\Delta t = 0.005 = 1.28h^2$.

Due to the additional curvature the neck region does not thicken as in the two-dimensional Cassini oval case, instead the surface collapses with the body splitting into two separate interfaces. Clearly the semi-implicit gradient augmented method can handle this topological change without difficulty. Note that the CFL condition in this case is $\Delta t/h^2 = 1.28$ is chosen for accuracy and not for stability reasons.

4.5.2   Area Conserving Mean Curvature Flow

An extension of standard mean curvature flow is mass-conserving mean curvature flow. In this type of motion the velocity of interface is given by $\boldsymbol{u} = (\kappa - \kappa_{avg})\boldsymbol{n}$ where κ is the mean curvature, $\boldsymbol{n}$ is the outward normal to the interface and κ_{avg} is the average of all interfacial curvature in the domain. The average curvature is calculated using the underlying level set function:

$$\kappa_{avg} = \frac{\int_\Omega \kappa \delta(\phi)|\nabla \phi|\mathrm{d}\boldsymbol{x}}{\int_\Omega \delta(\phi)|\nabla \phi|\mathrm{d}\boldsymbol{x}}, \tag{4.26}$$

where Ω is the computational domain. The function $\delta(\phi)$ is a smoothed Dirac delta function [62]. The final interface for this motion is given by a circle in two-dimensions, which corresponds to the constant curvature case.

Here the motion of a circle and two ellipses, as shown in Fig. 4.8, is considered. The circle has a radius of 0.4 and is centered at (0, 1.2) while both ellipses have a semi-major axis of 1.2 and a semi-minor axis of 0.35. The centers of the two ellipses are (0, 0) and (0, -1). Initially the average curvature is large due to the two ellipses. The circle has a smaller curvature than the average curvature and thus disappears. Over time the two ellipses grow and eventually merge. The final result is a single circle.

The total interfacial length and the enclosed area is also tracked, Fig. 4.9. The total interfacial length is given by $L_{total} = \int_\Omega \delta(\phi)|\nabla \phi|\mathrm{d}\boldsymbol{x}$ while the total enclosed

area is $A_{total} = \int_{\Omega} H(-\phi) \mathrm{d}\boldsymbol{x}$, where $H(\phi)$ is a smooth Heaviside function [62]. The total enclosed area changes by 1.2%, with the bulk of the errors in enclosed area introduced when the circle disappears and when the two ellipses merge.

(a) $t = 0$ (b) $t = 0.095$ (c) $t = 0.140$

(d) $t = 0.225$ (e) $t = 0.460$ (f) $t = 0.950$
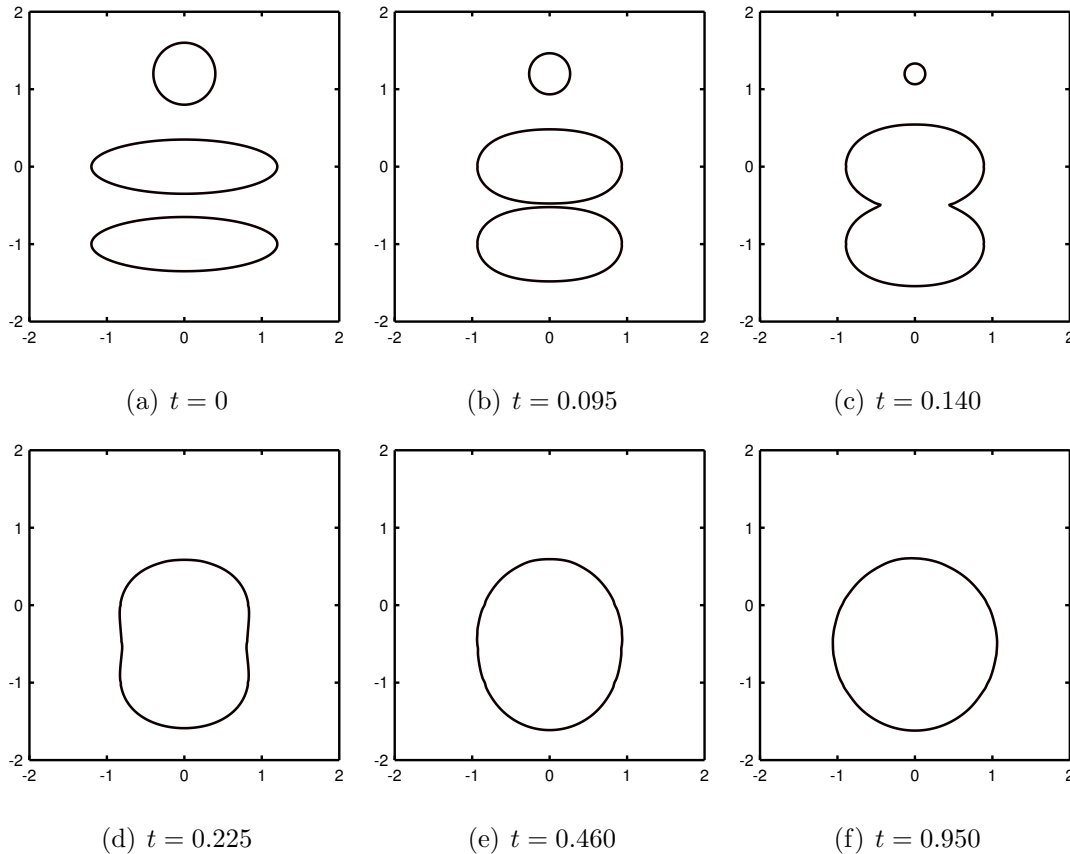
Figure 4.8: Area conserved mean curvature flow. $h = 0.0625$ while the time step is $\Delta t = 0.005 = 1.28h^2$. The overall change in the volume is 1.2%.

4.5.3   Surface Diffusion

This section considers the motion of interfaces due to the intrinsic variation of the curvature along the interface, or simply called surface diffusion. In this case the velocity of an interface is given by $\boldsymbol{v} = (\nabla_s^2 \kappa) \, \boldsymbol{n}$, where ∇_s^2 is the surface Laplacian. The final result for all surface diffusion cases will be a constant curvature interface: a circle in two dimensions and a sphere in three dimensions.
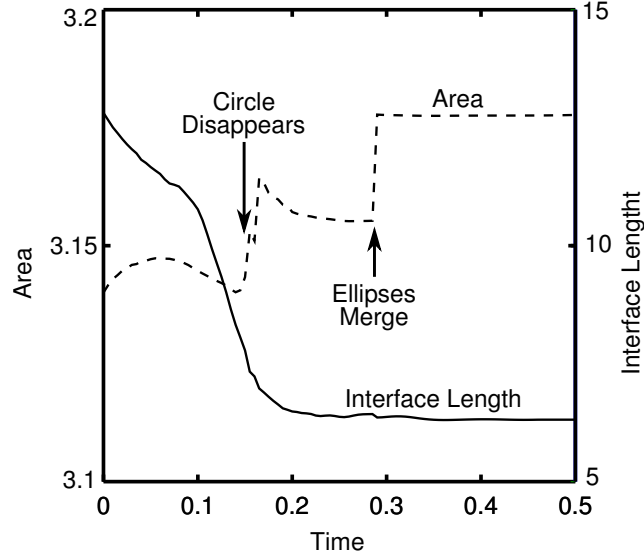
Figure 4.9: The enclosed area and interfacial length for area-preserving mean curvature flow from Fig. 4.8. The enclosed area changes by 1.2%. The bulk of the enclosed area error is introduced during topological changes.

The first shape considered is that of an inclined ellipse, Fig. 4.10, given by the parametric equation $x(\theta) = a\cos\theta + b\sin\theta$ and $y(\theta) = a\cos\theta - b\sin\theta$ with $a = 1.5$ and $b = 0.4$. As expected the high curvature regions move inward while the low curvature regions move outward. The end result is the expected circular interface.

This interface is also utilized as a qualitative check on the spatial and temporal convergence of the method. A grid study is performed by fixing the time step at $\Delta t = 10^{-4}$ and varying the grid spacing. The temporal study fixes the grid size at $h = 0.03125$ and varies the time step. The results for a time of 0.1 are seen in Fig. 4.11. As is seen in the detailed regions of Fig. 4.11 the solution consistently converges towards a particular shape given a value of Δt or h. This result indicates that h and Δt can be chosen independently according to either accuracy or stability constraints.
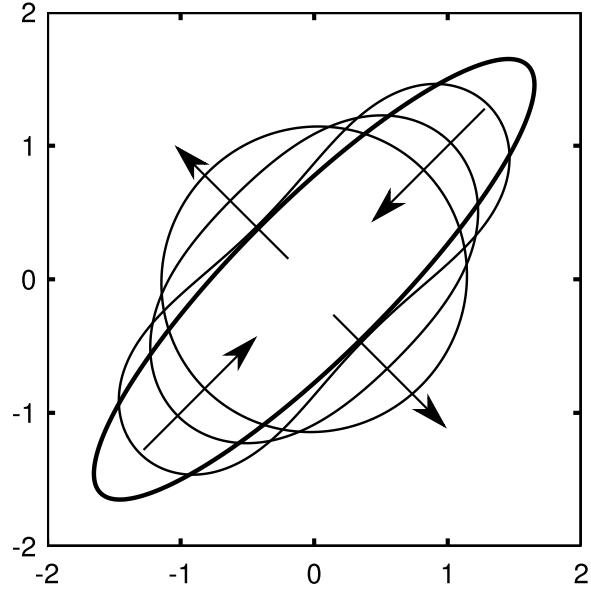
Figure 4.10: Motion by surface diffusion for an elliptical interface for a grid spacing of $h = 0.03125$ and a time step of $\Delta t = 0.001 \approx 1048h^4$. The thick line is the initial interface and the arrows indicate the direction of motion. Interfaces are shown for times of 0, 0.05, 0.2, and 0.6.
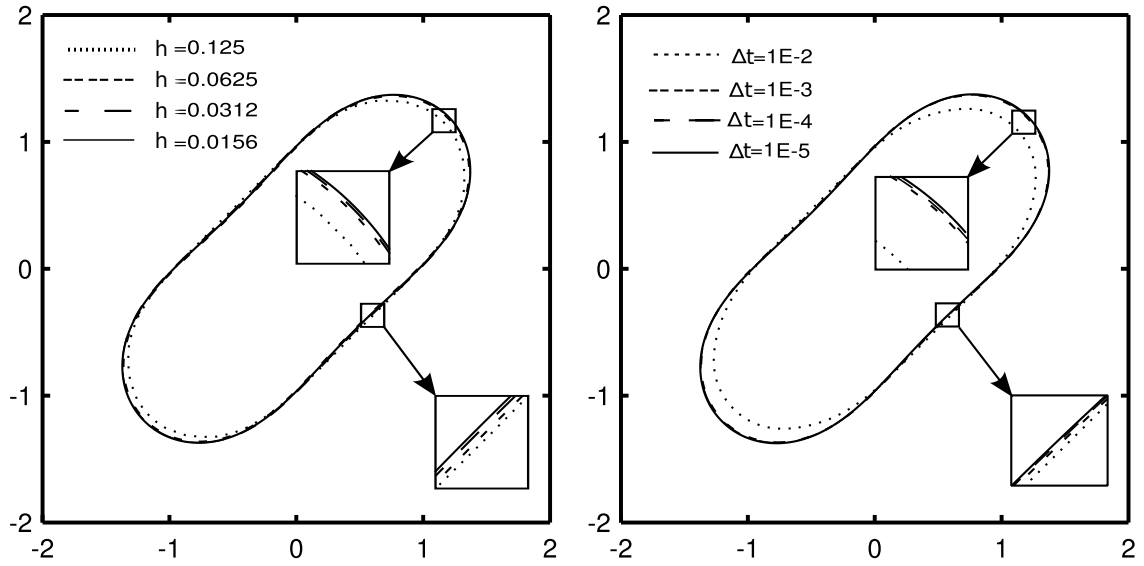
Figure 4.11: Qualitative convergence check for motion due to surface diffusion. For the spatial study the time step is fixed at $\Delta t = 10^{-4}$ while for the time study the grid spacing is fixed at $h = 0.015625$. All results are shown at a time of $t = 0.1$.

Next consider the evolution of a five-lobed star under surface diffusion. The equation of the star is given by Eqs. (4.23)-(4.25) with $r_0 = 1.1$, $\Delta r = 0.62$, and $n = 5$.

(a)   (b)
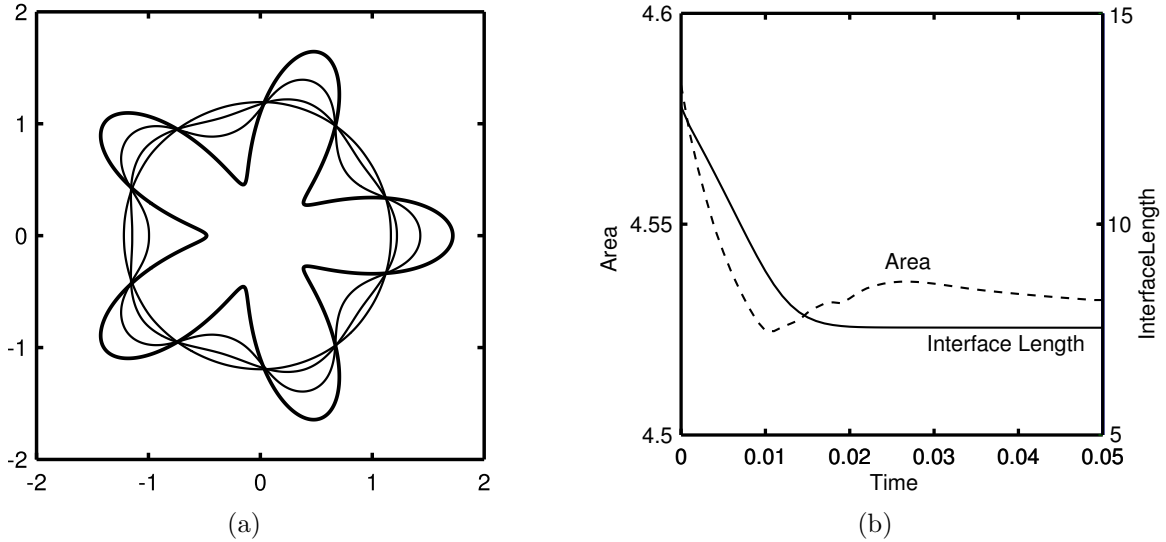
Figure 4.12: Motion by surface diffusion for a five-lobe star at using a grid spacing $h = 0.0625$ and a time step $\Delta t = 0.001 \approx 65h^4$. The motion of the interface is seen in (a) while the enclosed area and interface length are tracked in (b). The change in the enclosed area is 1.1%.

The result using a grid spacing of $h = 0.0625$ and a time step of $\Delta t = 0.001 \approx 65h^4$ is seen in Fig. 4.12. Unlike the inclined ellipse example of Fig. 4.10 this star has large curvature changes. The semi-implicit gradient augmented method is stable for this difficult case and reaches the equilibrium circular interface.

The enclosed area and total interface length of the five-lobed star are tracked and shown in Fig. 4.12. The initial area is 4.58 and changes by approximately 1.1% during the course of the simulation. Given the initial enclosed area it is expected that the final interface length should be 7.58. This compares to the actual final interface length of 7.54.

Now the extension to three-dimensional surfaces under surface diffusion is presented. The first is a dumbbell shape, Fig. 4.13. The interface consists of two spheres with a radius of 1.732 centered at (0, -0.9, 0) and (0., 0.9, 0). A cylinder of radius 0.06 connects the the spheres. This is a difficult interface to model due to the pinching of the center cylinder. Theoretically, as the center cylinder pinches off

the mean curvature increases to infinity. This results in the surface Laplacian of the curvature becoming singular. The semi-implicit gradient augmented level set method shown here handles this difficulty easily.

(a) $t = 0$

(b) $t = 0.0003$

(c) $t = 0.0005$

(d) $t = 0.005$
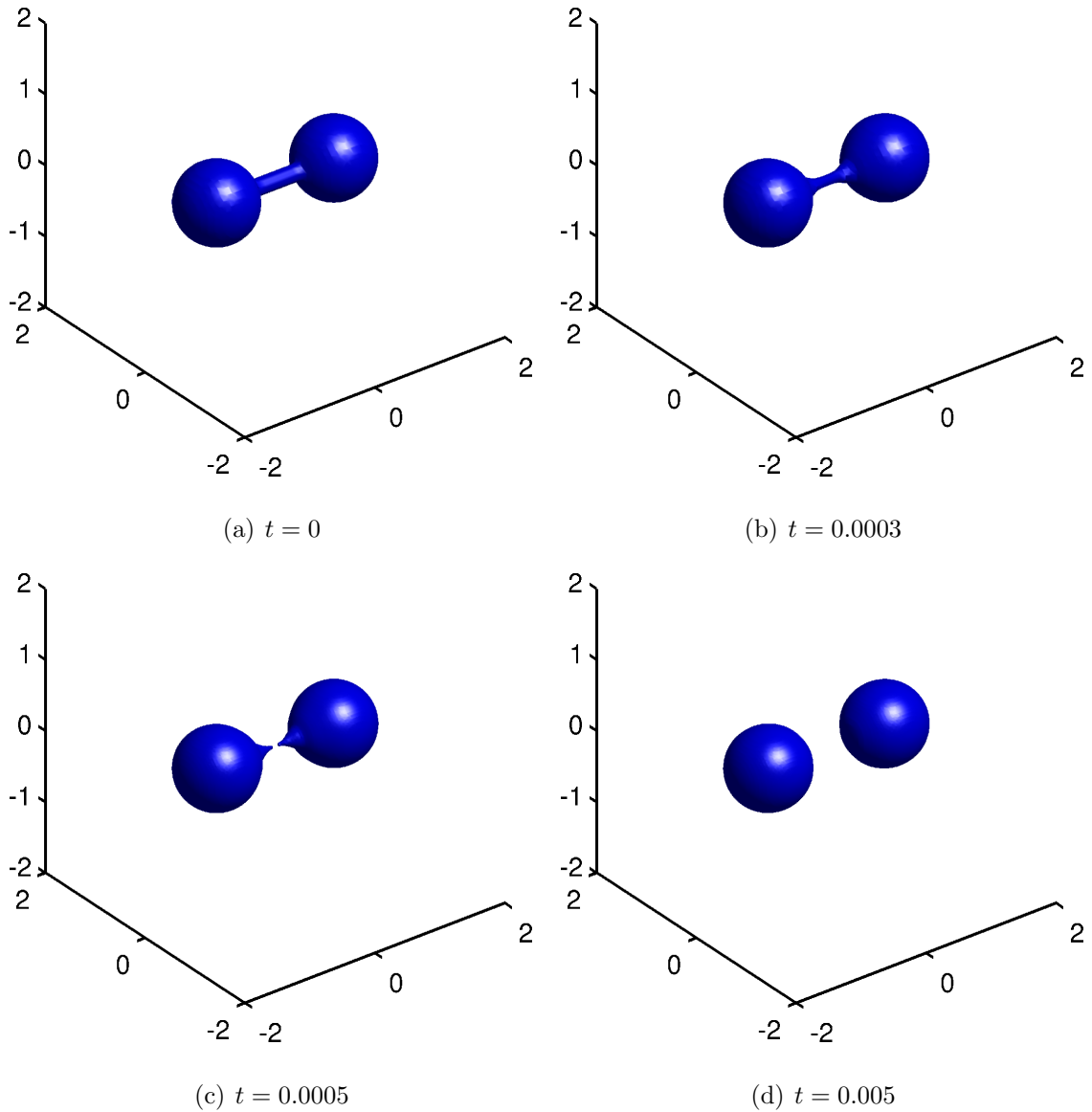
Figure 4.13: Motion by surface diffusion for a three-dimensional dumbbell surface. The grid spacing is $h = 0.0625$ and the time step is $\Delta t = 0.0001 \approx 6.5h^4$

Now consider a box-like shape with holes, Fig. 4.14. The interface is described by

$$\tilde{\phi} = \left((x^2 + y^2 - C^2)^2 + (z - 1)^2(z + 1)^2\right)\left((y^2 + z^2 - C^2)^2 + (x - 1)^2(x + 1)^2\right) \times$$

$$\left((x^2 + z^2 - C^2)^2 + (y - 1)^2(y + 1)^2\right) - 1 \tag{4.27}$$

where the parameter C is set to $C = 1.3$.

(a) $t = 0$ (b) $t = 0.05$

(c) $t = 0.09$ (d) $t = 0.3$
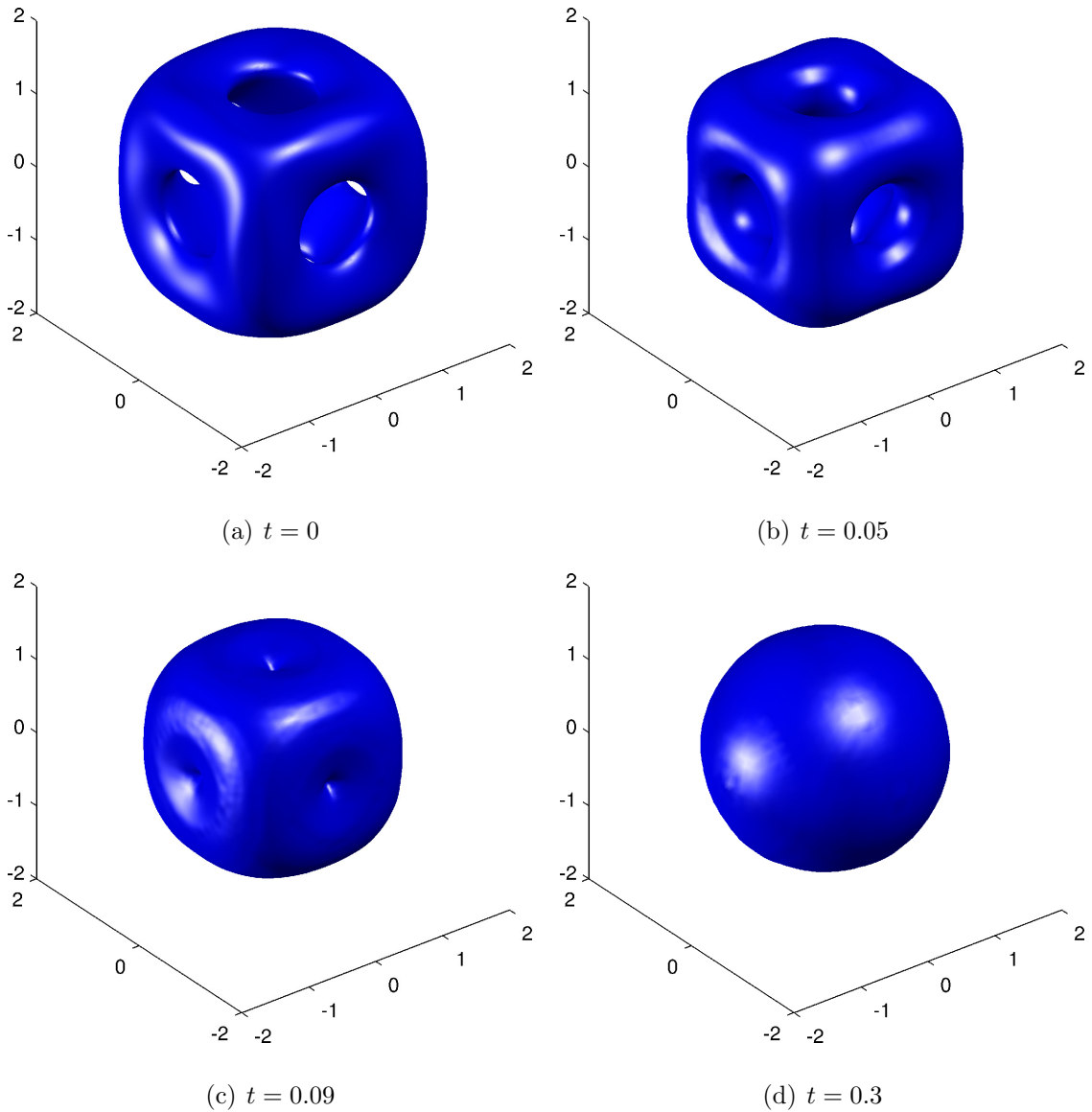
Figure 4.14: Evolution of a complex three-dimensional shape under surface diffusion. The grid spacing is $h = 0.0625$ and the time step is $\Delta t = 10^{-4} \approx 6.5h^4$

This particular surface has a large number of both negative and positive curvature regions. As the surface evolves portions of the interface merge, introducing large values for curvature and surface Laplacian of curvature. The SIGALS method handles these difficulties and the final result is the expected sphere.

4.5.4 The Non-Local Nature of the semi-implicit gradient augmented Method

The original semi-implicit level set method by Smereka demonstrated that the non-local nature of the smoothing term introduced errors as interfaces merge [87]. In this work similar results are seen but to a smaller degree than in the original semi-implicit level set method. To demonstrate this consider the the merging of a circle and an ellipse under surface diffusion, Fig. 4.15. Clearly it appears that the circle does in fact remain stationary until merging occurs. After merging the interface will eventually evolve into a single circle.

A more detailed look at the evolution demonstrates that the semi-implicit gradient augmented method does in fact introduce slight errors into the solution. In Fig. 4.16 the reference, original semi-implicit level set, and semi-implicit gradient augmented solutions are shown for two times slightly before merging. The reference solution is obtained by evolving the circle and ellipse on separate grids. In Fig. 4.16(a), shown at a time of $t = 0.0235$, the solutions appear very similar and both deviate very slightly from the reference solution. A short time later, at $t = 0.025$ (Fig. 4.16(b)), there is a noticeable error in the standard semi-implicit level set method. Upon investigating the curvatures of the circle (Fig. 4.16(c)) and the ellipse (Fig. 4.16(d)) at time $t = 0.0235$ oscillations can be observed.

(a) $t = 0$ (b) $t = 0.01$ (c) $t = 0.029$

(d) $t = 0.0304$ (e) $t = 0.032$ (f) $t = 0.035$
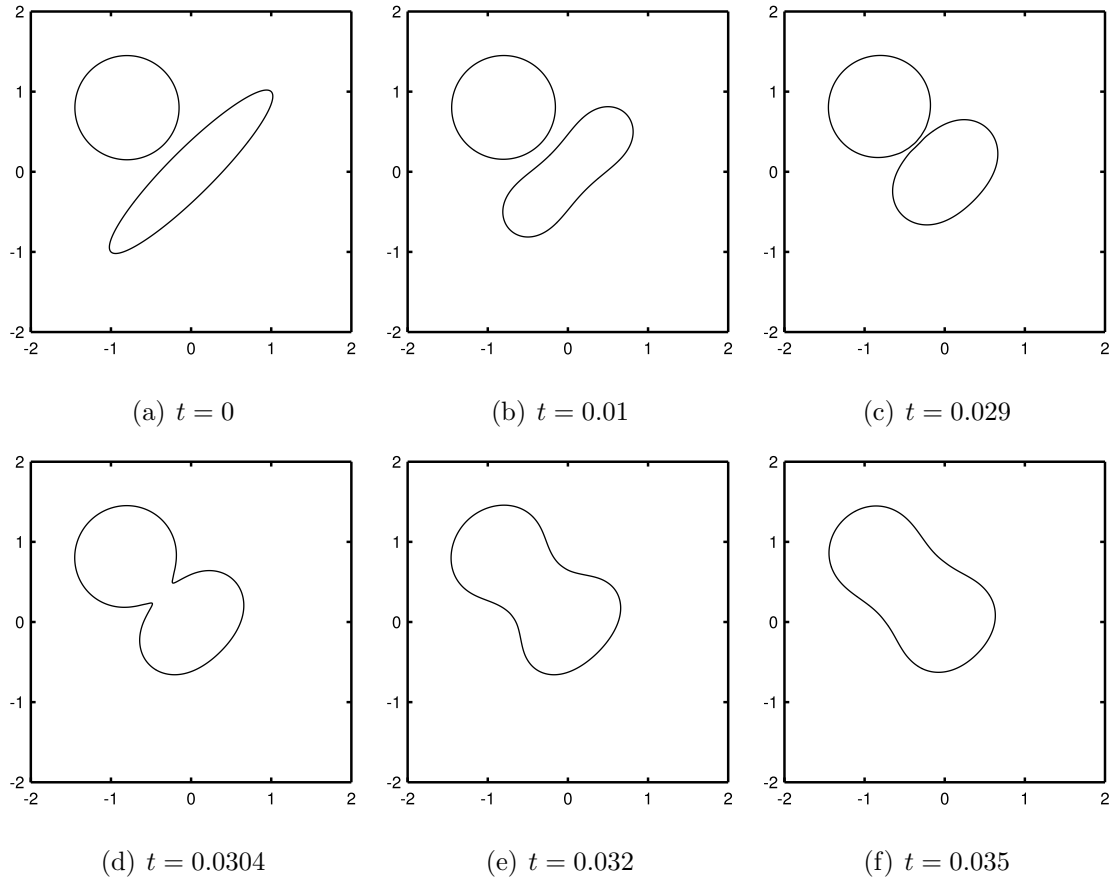
Figure 4.15: Coalescence of two bodies under surface diffusion flow. The time step is $\Delta t = 0.0001$ and while the grid spacing is $h = 0.03125$. There is minimal spurious motion of the circle before merging.

The oscillations for the semi-implicit gradient augmented method are smaller than for the original semi-implicit level set method. This is due to the additional information provided by tracking the gradient field. It might be possible to further reduce these oscillations by employing a more local version as suggested by the original gradient augmented level set method [56]. Even with a purely local curvature calculation, though, oscillations in the surface Laplacian of curvature field will still occur due to calculating the derivatives of the curvature field using finite difference approximations. It might be possible to use higher order interpolation schemes to approximate the level set function but this is not explored in this work.

(a) $t = 0.0235$ (b) $t = 0.025$
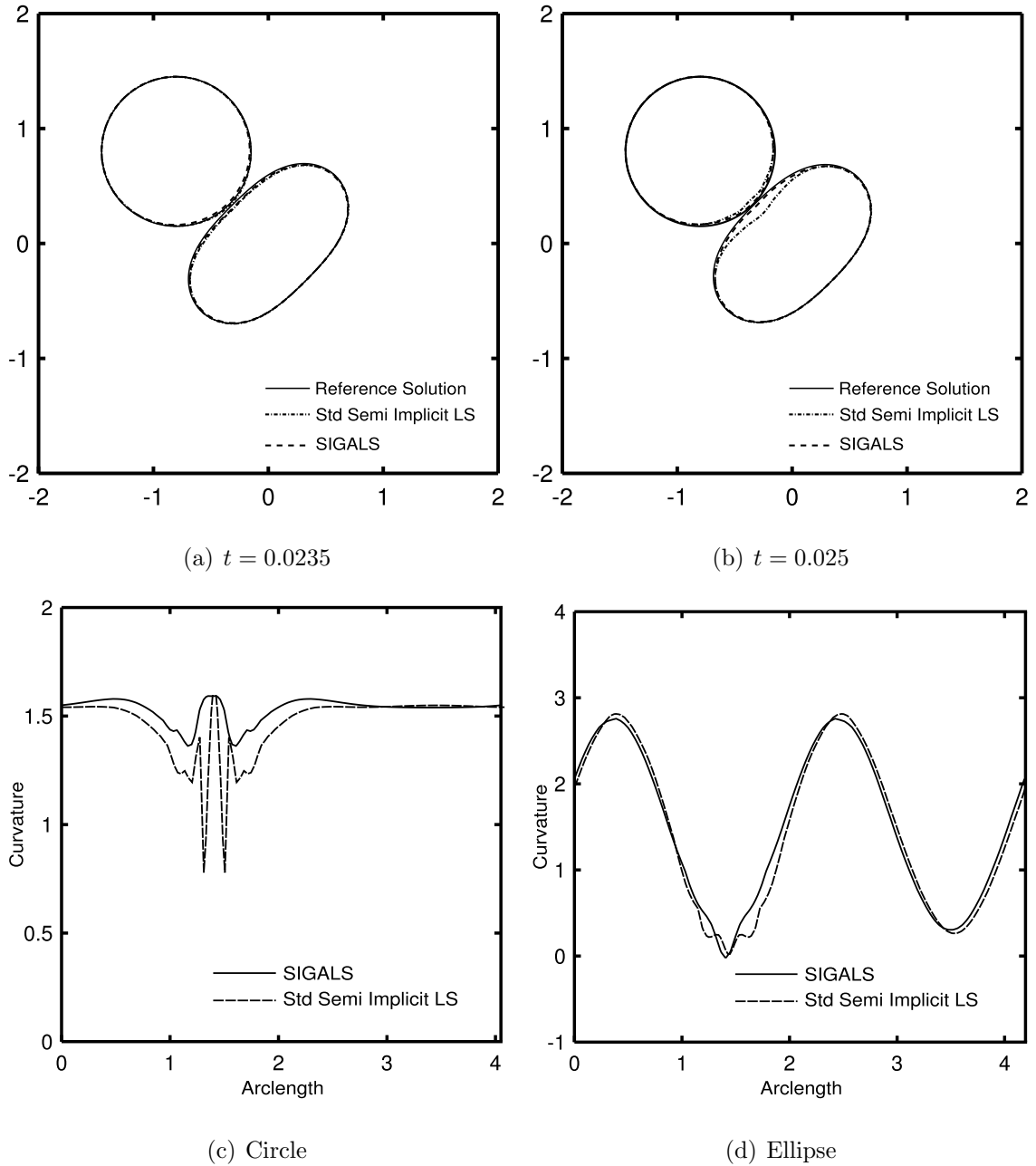
(c) Circle   (d) Ellipse

Figure 4.16: A comparison between the standard semi-implicit level set, the the semi-implicit gradient augmented method, and the reference solution for the case of a merging circle and ellipse. Two representative times are shown in (a) and (b). The curvature along the (c) circle and (d) ellipse are also shown for a time of $t = 0.0235$. The large curvature oscillations in the standard semi-implicit level set result in the incorrect behavior observed in (b).

4.5.5 Stability and Sensitivity Studies for β

Based on previous work and for simplicity a single value of $\beta = 0.5$ is chosen for the proposed method. While Smereka briefly explained that $\beta = 0.5$ is probably an optimal choice for semi-implicit schemes [87] the influence of β on the stability and accuracy of semi-implicit schemes has not yet been investigated.

To demonstrate the influence of β on the accuracy of a semi-implicit scheme consider the collapse of a three-dimensional Cassini oval under mean curvature flow (Fig. 4.7). As the smoothing term is artificially introduced it is expected that an increase in β will result in additional error begin introduced into the system. To demonstrate this the minimum neck radius of the Cassini oval is tracked over time for time steps of $\Delta t = 10^{-3}$ and $\Delta t = 10^{-4}$ and values of $\beta = 0, 0.1, 0.5, 1,$ and 5. Note that the speed at which the pinching occurs does not allow for larger time steps. The results are given in Fig. 4.17. Two main observations can be made. First, for a given time step even a large value of $\beta = 5$ introduces only small errors into the evolution of the neck radius. In fact, for the $\Delta t = 10^{-4}$ time step it is difficult to distinguish between the various β values. Second, the errors introduced by the smoothing are not solely controlled by the β parameters, but by the combination $\beta \Delta t$. Thus, if relatively small time steps are needed based on the underlying dynamics then even relatively large values of β will not adversely affect the accuracy. If on the other hand large time steps are used the use of a large smoothing parameter β may introduce large errors in the dynamical behavior of the system. This introduces are trade-off between accuracy and stability in the semi-implicit gradient augmented method.
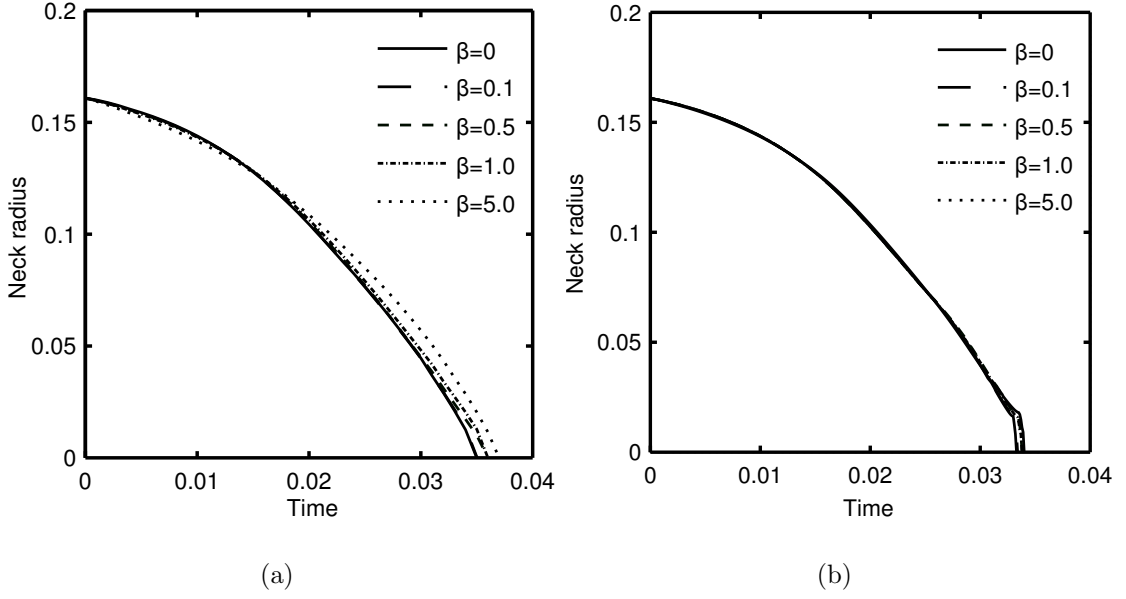
Figure 4.17: Influence of β on the dynamics and accuracy of a three-dimensional Cassini oval under mean curvature flow. (a) $\Delta t = 10^{-3}$. (b) $\Delta t = 10^{-4}$.

Next consider the minimum smoothing coefficient β needed for stability. Here the evolution due to surface diffusion of the two-dimensional five-lobed star in Fig. 4.12 is considered. Given a time step Δt the minimum β value needed for stability is experimentally determined. Let d_{max} represent the maximum distance from the center of the body to a location on the interface. Similarly let d_{min} represent the minimum distance from the center of the body to the interface. The difference, $d = d_{max} - d_{min}$, provides a measure that is used to qualitatively define stability. Stability is defined as the quantity d asymptotically approaching a value of zero. A demonstration of unstable behavior can be seen in Fig. 4.18(a) while stable behavior is seen in Fig. 4.18(b).

(a) $\beta = 0.1$: Unstable   (b) $\beta = 0.3$: Stable
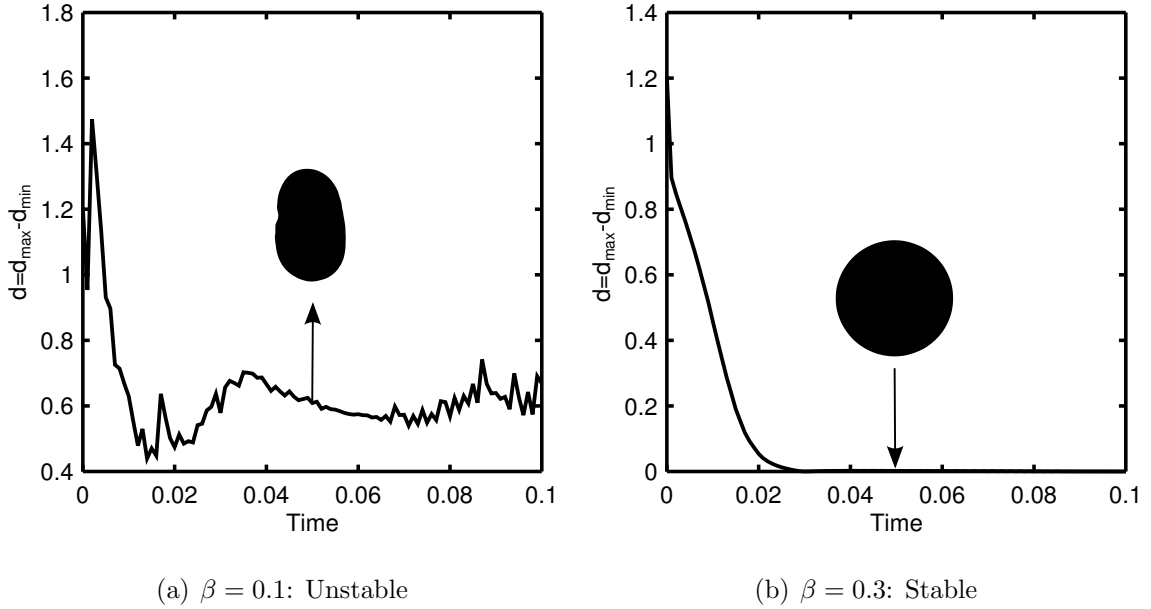
Figure 4.18: Examples of unstable and stable behavior for different β using $\Delta t = 10^{-3}$. Sample interfaces are also shown.

A systematic study has been performed using this qualitative stability measure for time step ranging from 10^{-5} to 10^{-2}, Fig. 4.19. As it is not possible to determine the precise minimum β value needed the uncertainty is noted in the figure. Please note that the fit is provided to aid the eye. As expected larger time steps require large smoothing coefficients. This result also indicates that, at least for this particular example, the choice of $\beta = 0.5$ is well justified. This smoothing parameter value is well in the stable region for the time step chosen in Fig. 4.12. The result in Fig. 4.17 demonstrated that for reasonable time steps the value of β has only a small influence on the accuracy of the result. While this result does not prove that $\beta = 0.5$ is the best choice in all situations, it is reasonable to assume that this choice of the smoothing parameter is a good first choice.
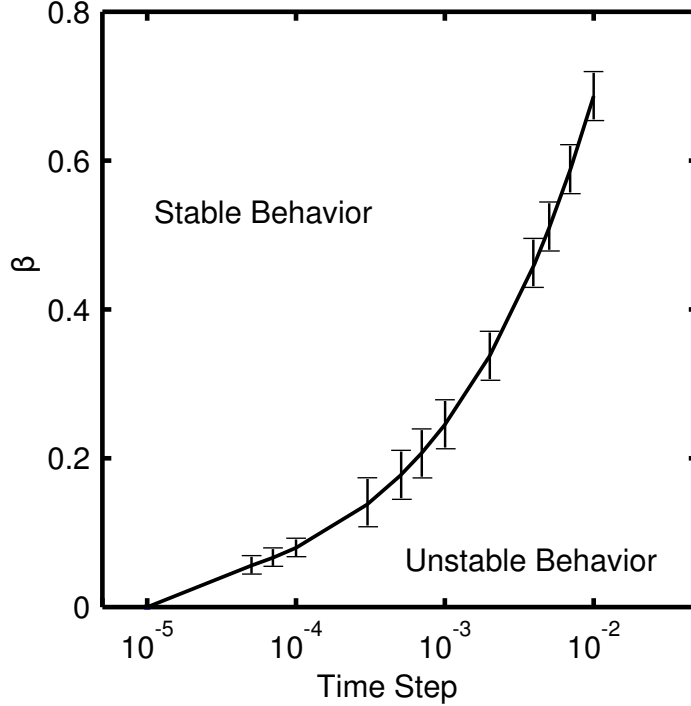
Figure 4.19: The minimum β parameter needed for the stable evolution of the five-lobed star shown in Fig. 4.12.

4.6   Evaluation/Advection of Surface Quantities

A word must be said about the solution of surface equations and advection of surface quantities. In the projection method the pressure is defined everywhere in the domain and thus standard techniques can be used. The tension, on the other hand, is only defined on the interface and must be handled using special methods. Unlike the immersed boundary method or other front-tracking techniques Lagrangian points are not tracked over the course of the simulation. Instead, all surface equations and quantities, such as the tension and trans-membrane potential, are evaluated using the Closest Point Method [48, 50]. The general idea is to replace surface equations by localized equations in the embedding space by extending quantities from the interface in a systematic way. This is done by replacing the value at a grid point in a

finite difference approximation by it's interpolated value at the closest point on the interface. Additional information can be found in References [48, 50].

All surface quantities, such as the tension and trans-membrane potential, are advected along side the interface (level set). After the level set is advected surface quantities are advected by using the total-derivative form of the advection equation for a material quantity f:

$$\boldsymbol{x}_d = \boldsymbol{x} - \Delta t \boldsymbol{u}^n, \tag{4.28}$$

$$\hat{f} = I_3 \left(f^n, \boldsymbol{x}_d \right), \tag{4.29}$$

where $I_3 \left(f^n, \boldsymbol{x}_d \right)$ is the evaluation of the cubic interpolant using the previous time-steps value evaluated at the departure location $\boldsymbol{x}_d$. The values are then replaced by the values at the closest point to a grid point,

$$f(\boldsymbol{x}) = I_3 \left(\hat{f}, \boldsymbol{x}_{cp} \right), \tag{4.30}$$

where $\boldsymbol{x}_{cp}$ is the closest point on the interface to grid point $\boldsymbol{x}$.

4.7 Semi-Jet Scheme

More recently Seibold *et al.* have generalized the third-order GALSM to arbitrary order under the name of Jet Schemes [81] . This method is essentially based on an advect-and-project formulation in function spaces. By carrying suitable portions of the jet of the solution, high-order numerical schemes can be easily constructed. Although the semi-implicit gradient augmented is stable and robust enough to handle the nonlinearities in the hydrodynamic and electrohydrodynamic equations and has been used as a powerful basis for tracking the interface in the vesicle simulations, still

an attempt has been made here to use the idea of the smoothing operator for the jet schemes as well. The method is briefly described here.

Consider the advection of the level set field, ϕ, and the associated gradient field, $\boldsymbol{\psi}$, due to an underlying flow field, $\boldsymbol{u}$. Seibold *et. al.* generalized this type of advection by considering a sub-grid of points centered on a grid point, which provides a *jet* of level set information [81]. It was shown that using a sub-grid spacing of $\mathcal{O}(\delta^{1/4})$, where δ is the floating point operation accuracy, provided the optimal accuracy for linear advection equations. In two dimensions and for every grid point (x_m, y_m) the level set and the higher derivatives, $(\phi, D\phi, \phi_{xy})$, are computed using approximate advection solution at the four points $(x_m + q_1\epsilon, y_m + q_2\epsilon)$ where $q \in \{-1, 1\}^2$. The procedure to find this advection solution is similar to the original gradient augmented method. Using these subgrid values of the level set, $\phi^{(-1,1)}$, $\phi^{(1,-1)}$, $\phi^{(-1,-1)}$ and $\phi^{(1,1)}$ one is able to obtain the desired derivatives at the grid point,

$$\phi = \frac{1}{4}\left(\phi^{(1,1)} + \phi^{(-1,1)} + \phi^{(1,-1)} + \phi^{(-1,-1)}\right), \tag{4.31}$$

$$\phi_x = \frac{1}{4\epsilon}\left(\phi^{(1,1)} - \phi^{(-1,1)} + \phi^{(1,-1)} - \phi^{(-1,-1)}\right), \tag{4.32}$$

$$\phi_y = \frac{1}{4\epsilon}\left(\phi^{(1,1)} + \phi^{(-1,1)} - \phi^{(1,-1)} - \phi^{(-1,-1)}\right), \tag{4.33}$$

$$\phi_{xy} = \frac{1}{4\epsilon}\left(\phi^{(1,1)} - \phi^{(-1,1)} - \phi^{(1,-1)} + \phi^{(-1,-1)}\right). \tag{4.34}$$

As the equations which model the electrohydrodynamics of vesicles require that a smooth level set field be maintained at all times, this high accuracy solution is relaxed. In the proposed formulation of the semi-jet scheme the jet of level-set information surrounding a grid point is in fact, the cell centers, Fig. 4.20(a). The advection of the level set jet proceeds with the following three steps: 1) advection of cell-centers, 2) smoothing at cell-centers, and 3) projection onto grid points. This method has the advantage of only requiring a single smoothing operation, as described below.

(a) *Advection*   (b) *Smoothing*   (c) *Interpolation*
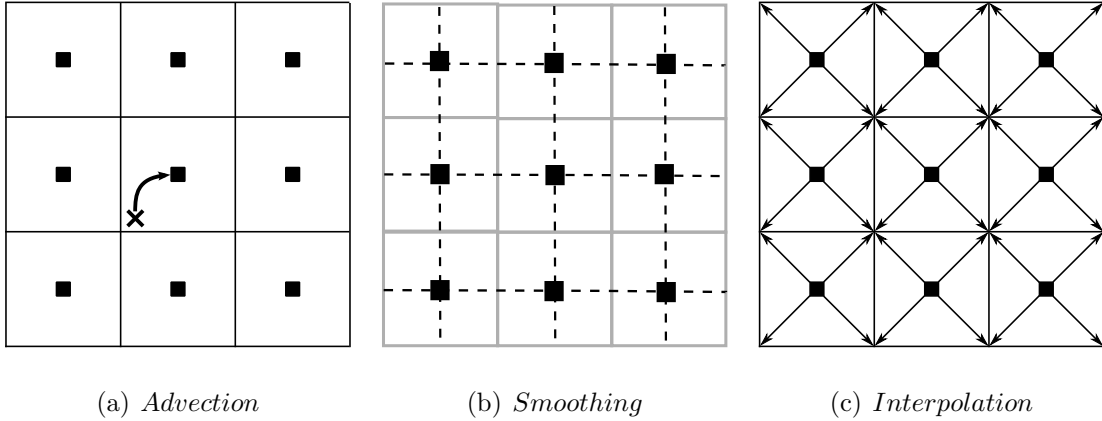
Figure 4.20: Schematic representation of the steps in Semi-implicit Jet Schemes.

The advection of cell-centers proceeds by using a Lagrangian advection scheme:

$$\boldsymbol{x}_d = \boldsymbol{x}_c - \Delta t \boldsymbol{u}_c^n, \tag{4.35}$$

$$\hat{\phi}^c = I_3 \left(\phi^n, \boldsymbol{x}_d \right), \tag{4.36}$$

where $\boldsymbol{x}^c$ is the cell-center location, $\hat{\phi}^c$ is the tentative level set value at the cell center, and $I_3 \left(\phi^n, \boldsymbol{x}_d \right)$ is a cubic interpolant of the previous time-steps level set values evaluated at the departure location, $\boldsymbol{x}_d$.

The values at cell-centers are then smoothed using a semi-implicit technique first introduced for standard level set advection [87]:

$$\frac{\phi^c - \hat{\phi}^c}{\Delta t} = \beta \nabla^2 \phi^c - \beta \nabla^2 \hat{\phi}^c, \tag{4.37}$$

where β is a user-parameter, typically chosen to be 0.5 [32, 87]. Note that the grid in this smoothing step is the cell-center (offset) grid. The boundary condition is the continuity of derivatives using the tentative level set values. For example, on the right

edge the boundary condition is

$$\left(\frac{\partial \phi^c}{\partial x}\right)_{N_x,j,k} = \frac{\hat{\phi}^c_{N_x-1/2,j,k} - \hat{\phi}^c_{N_x-3/2,j,k}}{h_x}, \tag{4.38}$$

where N_x and h_x are the the number of grid points and the grid-spacing in the x-direction, respectively.

Finally, the cell-center values are projected back onto the grid points by using second-order stencils. For example, the updated level set values at grid point (i, j, k) are given by

$$\phi_{i,j,k} = \frac{1}{8}\left(\phi^c_{i+1/2,j+1/2,k+1/2} + \phi^c_{i-1/2,j+1/2,k+1/2} + \phi^c_{i+1/2,j-1/2,k+1/2} \right. \tag{4.39}$$
$$+ \phi^c_{i-1/2,j-1/2,k+1/2} + \phi^c_{i+1/2,j+1/2,k-1/2} + \phi^c_{i-1/2,j+1/2,k-1/2}$$
$$\left. + \phi^c_{i+1/2,j-1/2,k-1/2} + \phi^c_{i-1/2,j-1/2,k-1/2}\right),$$

while the gradient in the x-direction is given by

$$\psi^x_{i,j,k} = \frac{1}{8h_x}\left(\phi^c_{i+1/2,j+1/2,k+1/2} - \phi^c_{i-1/2,j+1/2,k+1/2} + \phi^c_{i+1/2,j-1/2,k+1/2} \right. \tag{4.40}$$
$$- \phi^c_{i-1/2,j-1/2,k+1/2} + \phi^c_{i+1/2,j+1/2,k-1/2} - \phi^c_{i-1/2,j+1/2,k-1/2}$$
$$\left. + \phi^c_{i+1/2,j-1/2,k-1/2} - \phi^c_{i-1/2,j-1/2,k-1/2}\right).$$

The other gradient values can be similarly evaluated. The advantage of this method over the semi-implicit gradient augmented method is that only a single smoothing operation is required, versus one for the level set and three for the gradient fields. Work is currently underway investigating the full properties of this semi-implicit jet scheme.

Chapter 5

Discretization of Fluid Flow Equations

In this chapter a novel projection method is introduced to solve for the fluid flow equations. When considering the modeling of lipid vesicles, there are four total conservation conditions that must be satisfied during the course of the simulation: 1) local surface area, 2) total surface area, 3) local fluid volume, 4) total fluid volume. Vesicle dynamics are extremely sensitive to any changes in these quantities [72, 74, 11, 10] and thus high accuracy is required. In [72] an iterative four-step level-set projection method was employed to solve for the hydrodynamics of the vesicle. Pressure and tension were determined as two Lagrange multipliers to ensure both the incompressibility of the fluid and the surface inextensibility of the membrane. The algorithm explained in this chapter bears some resemblance to the above-mentioned method but there are some differences which will be addressed below.

Accumulation of error in the solution of the fluid equations over time, in addition to the non-conservation properties of the level set method, can induce large errors over the course of the simulation. To account for this, the fluid equations will be modified to explicitly correct any error accumulation. The idea presented here is

based on the work of Laadhari *et. al.* [36]. The difference is that in the previous work the corrections were not reflected in the fluid field, but instead modified the velocity used to advect the level set. Here, the corrections are included in the fluid field calculation and therefore a modified advection field is not required. Preliminary results for standard multiphase flow problems were presented in Ref. [71] and are extended here for vesicles.

A projection method is implemented to solve for the velocity, pressure and tension. First, a semi-implicit update is performed to obtain a tentative velocity field,

$$
\frac{\boldsymbol{u}^* - \boldsymbol{u}^n}{\Delta t} + \boldsymbol{u}^n \cdot \nabla \boldsymbol{u}^* = -\nabla p^n + \frac{1}{Re} \nabla \cdot \left(\nabla \boldsymbol{u}^* + (\nabla \boldsymbol{u}^n)^T \right) + \boldsymbol{f}_H^n + \boldsymbol{f}_\gamma^n + \boldsymbol{f}_{el}^n, \quad (5.1)
$$

where $\boldsymbol{f}_H$, $\boldsymbol{f}_\gamma$ and $\boldsymbol{f}_{el}$ are the bending, tension, and electric field forces localized around the interface, Eq. (2.27). The superscript n refers to the solution at the previous time step.

Next, the tentative velocity field is projected onto the divergence and surface-divergence free velocity space,

$$
\frac{\boldsymbol{u}^{n+1} - \boldsymbol{u}^*}{\Delta t} = -\nabla q + \delta(\phi) \|\nabla \phi\| \left(\nabla_s \xi - \xi H \nabla \phi \right), \quad (5.2)
$$

where q and ξ are the corrections needed for the pressure and tension, respectively. Finally, the pressure and tension are updated by including the corrections,

$$
p^{n+1} = p^n + q, \quad (5.3)
$$

$$
\gamma^{n+1} = \gamma^n + \xi. \quad (5.4)
$$

The four conservation conditions can be written as [36]

$$\nabla \cdot \boldsymbol{u}^{n+1} = 0 \qquad \text{(local volume conservation)}, \qquad (5.5)$$

$$\int_{\Gamma} \boldsymbol{n} \cdot \boldsymbol{u}^{n+1} \, dA = \frac{dV}{dt} \qquad \text{(global volume conservation)}, \qquad (5.6)$$

$$\nabla_s \cdot \boldsymbol{u}^{n+1} = 0 \qquad \text{(local area conservation)}, \qquad (5.7)$$

$$\int_{\Gamma} H\boldsymbol{n} \cdot \boldsymbol{u}^{n+1} \, dA = \frac{dA}{dt} \qquad \text{(global area conservation)}. \qquad (5.8)$$

The use of only the pressure and tension is not sufficient to satisfy all four conservation conditions. There, the pressure and tension fields are split into a constant and spatially-varying component:

$$p = \tilde{p} + (1 - H(\phi))p_0, \qquad (5.9)$$

$$\gamma = \tilde{\gamma} + \gamma_0, \qquad (5.10)$$

where $\tilde{p}$ and $\tilde{\gamma}$ are spatially varying while p_0 and γ_0 are constant. Note that $\tilde{p}$, $\tilde{\gamma}$, p_0, and γ_0 all vary in time. Conceptually, this splitting allows for the enforcement of local conservation through $\tilde{p}$ and $\tilde{\gamma}$ while global conservation is enforced through p_0 and γ_0.

The corresponding corrections are now $q = \tilde{q} + (1 - H(\phi))q_0$, and $\xi = \tilde{\xi} + \xi_0$, while the projection step, Eq. (5.2), is now written as

$$\boldsymbol{u}^{n+1} = \boldsymbol{u}^* + \Delta t \left(-\nabla \tilde{q} + \delta(\phi)q_0 \nabla \phi + \delta(\phi)\|\nabla \phi\| \left(\nabla_s \tilde{\xi} - \tilde{\xi} H \nabla \phi - \xi_0 H \nabla \phi \right) \right). \ (5.11)$$

Noting that the time derivatives of the volume and area are to correct any accumulated errors in the solution, and using Eq. (5.11), the four conservation equations can be written in terms of the four unknowns ($\tilde{q}$, $\tilde{\xi}$, q_0, and ξ_0), the current area and volume, and the initial area and volume. Specifically, applying the local area

conservation equation requires that

$$-\nabla \cdot \boldsymbol{u}^* = \Delta t \nabla \cdot \left(-\nabla \tilde{q} + \delta(\phi) q_0 \nabla \phi + \delta(\phi) \|\nabla \phi\| \left(\nabla_s \tilde{\xi} - \tilde{\xi} H \nabla \phi + \xi_0 H \nabla \phi \right) \right), \quad (5.12)$$

while the total volume conservation requires that

$$\frac{V^0 - V^n}{\Delta t} - \int_\Gamma \boldsymbol{n} \cdot \boldsymbol{u}^* \, dA =$$
$$\Delta t \int_\Gamma \left(-\boldsymbol{n} \cdot \nabla \tilde{q} + \delta(\phi) q_0 \|\nabla \phi\| - \delta(\phi) \|\nabla \phi\|^2 \left(\tilde{\xi} H + \xi_0 H \right) \right) \, dA, \quad (5.13)$$

where V^n is the current volume and the time-derivative of the volume is chosen so that at the end of the time-step the volume equals the initial volume, V^0.

Conservation of local and global area results in the following two equations:

$$-\nabla_s \cdot \boldsymbol{u}^* = \Delta t \nabla_s \cdot \left(-\nabla \tilde{q} + \delta(\phi) q_0 \nabla \phi + \delta(\phi) \|\nabla \phi\| \left(\nabla_s \tilde{\xi} - \tilde{\xi} H \nabla \phi - \xi_0 H \nabla \phi \right) \right),$$
$$(5.14)$$

and

$$\frac{A^0 - A^n}{\Delta t} - \int_\Gamma H \boldsymbol{n} \cdot \boldsymbol{u}^* \, dA =$$
$$\Delta t \int_\Gamma H \left(-\boldsymbol{n} \cdot \nabla \tilde{q} + \delta(\phi) q_0 \|\nabla \phi\| - \delta(\phi) \|\nabla \phi\|^2 \left(\tilde{\xi} H + \xi_0 H \right) \right) \, dA, \quad (5.15)$$

where A^0 is the initial surface area and A^n is the current surface area.

Let $\tilde{\boldsymbol{q}}$ represent the vector holding the values of $\tilde{q}$ in the entire, discretized domain and $\tilde{\boldsymbol{\xi}}$ is the vector holding the values of $\tilde{\xi}$ in the entire, discretized domain. It is now possible to represent the conservation relationships, Eqs. (5.12)-(5.15), as linear operators acting on $\tilde{\boldsymbol{q}}$, q_0, $\tilde{\boldsymbol{\xi}}$, and ξ_0. Local volume conservation, Eq. (5.12), can be represented as

$$\boldsymbol{L} \tilde{\boldsymbol{q}} + \boldsymbol{l} q_0 + \boldsymbol{L}_\xi \tilde{\boldsymbol{\xi}} + \boldsymbol{l}_\xi \xi_0 = -\boldsymbol{D} \boldsymbol{u}^*, \quad (5.16)$$

where $\boldsymbol{D}$ is the discrete divergence operator and

$$\boldsymbol{L}\tilde{q} \approx -\Delta t\nabla \cdot \nabla\tilde{q}, \qquad\qquad\qquad lq_0 \approx q_0\Delta t\nabla \cdot (\delta(\phi)\nabla\phi),$$

(5.17)

$$\boldsymbol{L}_\xi\tilde{\boldsymbol{\xi}} \approx \Delta t\nabla \cdot \left(\delta(\phi)\|\nabla\phi\|\left(\nabla_s\tilde{\xi} - \tilde{\xi}H\nabla\phi\right)\right), \quad l_\xi\xi_0 \approx \xi_0\Delta t\nabla \cdot (\delta(\phi)\|\nabla\phi\|H\nabla\phi),$$

(5.18)

are the discretizations of the continuous operations. Note that $\boldsymbol{L}$ and $\boldsymbol{L}^\xi$ are a linear operator matrices while $\boldsymbol{l}$ and $\boldsymbol{l}_\xi$ are linear operator vectors.

The integrals over the vesicle interface can be approximated as summations over the discretized domain: $\int_\Gamma f\ dA \approx \sum \delta_{i,j,k}f_{i,j,k}\Delta V$, where $\delta_{i,j,k}$ is the Dirac delta function defined in Eq. (2.26) at a grid point, $f_{i,j,k}$ is the function value at that grid point, and $\Delta V = h_xh_yh_z$ is the volume of a cell. In linear operator form this calculated by taking the dot product between the integration vector and the vector containing the function values. Define the following linear operations:

$$\boldsymbol{s}^T\tilde{q} \approx -\Delta t\int_\Gamma (\boldsymbol{n} \cdot \nabla\tilde{q})\, dA, \qquad\qquad aq_0 \approx q_0\Delta t\int_\Gamma \delta(\phi)\|\nabla\phi\|dA, \qquad (5.19)$$

$$\boldsymbol{s}_\xi^T\tilde{\boldsymbol{\xi}} \approx -\Delta t\int_\Gamma \left(\delta(\phi)\|\nabla\phi\|^2\tilde{\xi}H\right) dA, \quad a_\xi\xi_0 \approx \xi_0\Delta t\int_\Gamma \left(\delta(\phi)\|\nabla\phi\|^2H\right) dA. \quad (5.20)$$

In this case $\boldsymbol{s}$ and $\boldsymbol{s}_\xi$ are linear operator vectors while a and a_ξ are scalar values. This results in the following linear equation:

$$\boldsymbol{s}^T\tilde{q} + aq_0 + \boldsymbol{s}_\xi^T\tilde{\boldsymbol{\xi}} + a_\xi\xi_0 = E_V, \qquad (5.21)$$

where $E_V \approx (V^0 - V^n)/\Delta t - \int_\Gamma (\boldsymbol{n} \cdot \boldsymbol{u}^*)\, dA$ is the discrete form of the global volume correction needed.

The surface-conservation equations are written in a similar manner:

$$\boldsymbol{L}^s \tilde{q} + \boldsymbol{l}^s q_0 + \boldsymbol{L}_\xi^s \tilde{\boldsymbol{\xi}} + \boldsymbol{l}_\xi^s \xi_0 = -\boldsymbol{D}_s \boldsymbol{u}^*, \qquad (5.22)$$

where $\boldsymbol{D}_s$ is the discrete surface-divergence operator and

$$\boldsymbol{L}^s \tilde{q} \approx -\,\Delta t \nabla_s \cdot \nabla \tilde{q}, \qquad\qquad\qquad \boldsymbol{l}^s q_0 \approx q_0 \Delta t \nabla_s \cdot \left(\delta(\phi) \nabla \phi \right),$$
$$(5.23)$$

$$\boldsymbol{L}_\xi^s \tilde{\boldsymbol{\xi}} \approx \Delta t \nabla_s \cdot \left(\delta(\phi) \|\nabla \phi\| \left(\nabla_s \tilde{\xi} - \tilde{\xi} H \nabla \phi \right) \right), \quad \boldsymbol{l}_\xi^s \xi_0 \approx \xi_0 \Delta t \nabla_s \cdot \left(\delta(\phi) \|\nabla \phi\| H \nabla \phi \right)$$
$$(5.24)$$

for the local surface-area conservation, Eq. (5.14) and

$$\boldsymbol{s}_H^T \tilde{q} + b q_0 + \boldsymbol{s}_{H\xi}^T \tilde{\boldsymbol{\xi}} + b_\xi \xi_0 = E_A, \qquad (5.25)$$

where $E_A \approx (A_0 - A^n)/\Delta t - \int_\Gamma (H \boldsymbol{n} \cdot \boldsymbol{u}^*) \, dA$ is the discrete form of the global area correction needed and

$$\boldsymbol{s}_H^T \tilde{q} \approx -\,\Delta t \int_\Gamma (H \boldsymbol{n} \cdot \nabla \tilde{q}) \, dA, \qquad b q_0 \approx q_0 \Delta t \int_\Gamma H \delta(\phi) \|\nabla \phi\| dA, \qquad (5.26)$$
$$\boldsymbol{s}_{H\xi}^T \tilde{\boldsymbol{\xi}} \approx -\,\Delta t \int_\Gamma \left(\delta(\phi) \|\nabla \phi\|^2 \tilde{\xi} H^2 \right) dA, \quad b_\xi \xi_0 \approx \xi_0 \Delta t \int_\Gamma \left(\delta(\phi) \|\nabla \phi\|^2 H^2 \right) dA. \quad (5.27)$$

Using the notation above the set of four linear equations can be written in matrix-vector form:

$$\begin{bmatrix} \boldsymbol{L} & \boldsymbol{l} & \boldsymbol{L}_\xi & \boldsymbol{l}_\xi \\ \boldsymbol{s}^T & a & \boldsymbol{s}_\xi^T & a_\xi \\ \boldsymbol{L}^s & \boldsymbol{l}^s & \boldsymbol{L}_\xi^s & \boldsymbol{l}_\xi^s \\ \boldsymbol{s}_H^T & b & \boldsymbol{s}_{H\xi}^T & b_\xi \end{bmatrix} \begin{bmatrix} \tilde{q} \\ q_0 \\ \tilde{\boldsymbol{\xi}} \\ \xi_0 \end{bmatrix} = \begin{bmatrix} -\boldsymbol{D}\boldsymbol{u}^* \\ E_V \\ -\boldsymbol{D}_s \boldsymbol{u}^* \\ E_A \end{bmatrix}. \qquad (5.28)$$

Note that the specific spatial discretization have not yet been specified, as the general concepts are discretization-independent.

While it is possible to form a globally-assembled matrix for Eq. (5.28), it would be computationally expensive. Not only would the size of the system be large, but it would also have to be re-formed every time step as many of the components, such as $\boldsymbol{L}_\xi^s$, $\boldsymbol{l}_\xi^s$ and $\boldsymbol{s}_H^T$ depend on the location of the interface, which changes over time. Instead, write the complete system in the following simplified notation,

$$
\begin{bmatrix} \mathbb{A} & \mathbb{B} \\ \mathbb{C} & \mathbb{D} \end{bmatrix} \begin{bmatrix} \boldsymbol{q} \\ \boldsymbol{\xi} \end{bmatrix} = \begin{bmatrix} \boldsymbol{e}_V \\ \boldsymbol{e}_A \end{bmatrix},
\tag{5.29}
$$

where

$$
\mathbb{A} = \begin{bmatrix} \boldsymbol{L} & \boldsymbol{l} \\ \boldsymbol{s}^T & a \end{bmatrix}, \qquad \mathbb{B} = \begin{bmatrix} \boldsymbol{L}_\xi & \boldsymbol{l}_\xi \\ \boldsymbol{s}_\xi^T & a_\xi \end{bmatrix},
$$

$$
\mathbb{C} = \begin{bmatrix} \boldsymbol{L}^s & \boldsymbol{l}^s \\ \boldsymbol{s}_H^T & b \end{bmatrix}, \quad \text{and} \quad \mathbb{D} = \begin{bmatrix} \boldsymbol{L}_\xi^s & \boldsymbol{l}_\xi^s \\ \boldsymbol{s}_{H\xi}^T & b_\xi \end{bmatrix},
\tag{5.30}
$$

with the combined vectors $\boldsymbol{q} = [\tilde{\boldsymbol{q}}, q_0]^T$, $\boldsymbol{\xi} = [\tilde{\boldsymbol{\xi}}, \xi_0]^T$, $\boldsymbol{e}_V = [-\boldsymbol{D}\boldsymbol{u}^*, E_V]^T$ and $\boldsymbol{e}_A = [-\boldsymbol{D}_s\boldsymbol{u}^*, E_A]^T$. Using a Schur Complement approach the solution is

$$
\begin{bmatrix} \boldsymbol{q} \\ \boldsymbol{\xi} \end{bmatrix} = \begin{bmatrix} \mathbb{I}_q & \boldsymbol{0} \\ -\mathbb{D}^{-1}\mathbb{C} & \mathbb{I}_\xi \end{bmatrix} \begin{bmatrix} \mathbb{S}^{-1} & \boldsymbol{0} \\ \boldsymbol{0} & \mathbb{D}^{-1} \end{bmatrix} \begin{bmatrix} \mathbb{I}_q & -\mathbb{B}\mathbb{D}^{-1} \\ \boldsymbol{0} & \mathbb{I}_\xi \end{bmatrix} \begin{bmatrix} \boldsymbol{e}_V \\ \boldsymbol{e}_A \end{bmatrix},
\tag{5.31}
$$

where $\mathbb{S}$ is the Schur Complement of the original partitioned matrix and is give by

$$
\mathbb{S} = \mathbb{A} - \mathbb{B}\mathbb{D}^{-1}\mathbb{C}.
\tag{5.32}
$$

The application of the Schur Complement is accomplished by a matrix-free iterative solver, such as GMRES.

Let the focus now turn to the calculation of $\mathbb{D}^{-1}$. This inverse is given implicitly through the solution of the following, generalized linear system:

$$\begin{bmatrix} \boldsymbol{L}_\xi^s & \boldsymbol{l}_\xi^s \\ \boldsymbol{s}_H^T & b_\xi \end{bmatrix} \begin{bmatrix} \boldsymbol{x}_0 \\ x_1 \end{bmatrix} = \begin{bmatrix} \boldsymbol{y}_0 \\ y_1 \end{bmatrix}. \tag{5.33}$$

Turning to the Schur Decomposition the solution can be written as

$$\begin{bmatrix} \boldsymbol{x}_0 \\ x_1 \end{bmatrix} = \begin{bmatrix} \boldsymbol{I} & 0 \\ b_\xi^{-1} \boldsymbol{s}_H^T & 1 \end{bmatrix} \begin{bmatrix} \boldsymbol{S}^{-1} & 0 \\ 0 & b_\xi^{-1} \end{bmatrix} \begin{bmatrix} \boldsymbol{I} & -b_\xi^{-1} \boldsymbol{l}_\xi^s \\ 0 & 1 \end{bmatrix} \begin{bmatrix} \boldsymbol{y}_0 \\ y_1 \end{bmatrix}, \tag{5.34}$$

where the Schur Complement is a rank-1 update on the matrix $\boldsymbol{L}_\xi^s$:

$$\boldsymbol{S} = \boldsymbol{L}_\xi^s - \frac{1}{b_\xi} \boldsymbol{l}_\xi^s \boldsymbol{s}_H^T. \tag{5.35}$$

Using the Sherman–Morrison formula the inverse of this Schur Complement is given by

$$\boldsymbol{S}^{-1} = \left(\boldsymbol{L}_\xi^s\right)^{-1} + \frac{\left(\boldsymbol{L}_\xi^s\right)^{-1} \boldsymbol{l}_\xi^s \boldsymbol{s}_H^T \left(\boldsymbol{L}_\xi^s\right)^{-1}}{b_\xi - \boldsymbol{s}_H^T \left(\boldsymbol{L}_\xi^s\right)^{-1} \boldsymbol{l}_\xi^s}. \tag{5.36}$$

So long as $b_\xi \neq \boldsymbol{s}_H^T \left(\boldsymbol{L}_\xi^s\right)^{-1} \boldsymbol{l}_\xi^s$ this inverse is defined. While this inequality will not be proven here, a check during the course of the simulations presented in Chapters 6 and 7 shows that this condition has never been violated.

Chapter 6

Results: Hydrodynamics of the Vesicle

To demonstrate the robustness and effectiveness of the hydrodynamic portion of the numerical method and for the purpose of the verification, sample results are presented in this chapter for a vesicle both in quiescent flow and under linear shear flow when the electric field is absent ($Mn = 0$). Note that as it was mentioned in Chap. 2 the characteristic time scale associated with for this case is $t_0 = t_\gamma = 1s$. Using the typical experimental values given in Sec. 2.6 the dimensionless parameters are found to be $Re = 0.001$ and $Ca = 10$. Unless otherwise stated, these parameters along with a dimensionless shear rate of $\chi = 1$ at the boundary are used for the hydrodynamic simulations.

The vesicle surface area is fixed to 4π in all the situations while the enclosed volume varies depends on the reduced volume. For all results presented here a collocated, Cartesian mesh with uniform grid spacing in each direction is used. Periodicity is assumed in the x- and z-directions while wall boundary conditions are given in the y-direction. Unless otherwise stated the domain is a box covering the domain $[-4.5, 4.5]^3$, the grid spacing is $h = 0.075$ and the time-step is chosen to

be $\Delta t = 0.05h \approx 0.00375$. A thorough investigation of grid-independence study, temporal-independence and confinement effect are carried out for the electrohydrodynamic simulation and the results will be presented in chapter 7. Since the electrohydrodynamics of the vesicle has much faster dynamics and significantly larger deformation than the hydrodynamic simulation, the same choice of grid spacing, time step and domain size are used for the hydrodynamic simulation as well.

6.1 The Equilibrium Biconcave Shape

In the first example, the behavior of the vesicle is investigated when no shear flow is imposed ($\chi = 0$). Therefore both hydrodynamic forces of the fluid and the elastic forces of the membrane will be reactive forces attempting to minimize the energy state of the vesicle. Due to the area and volume constraints and the nature of the forces acting on the membrane the equilibrium shape for an initially disk-like vesicle is expected to be a three-dimensional biconcave shape similar to the natural geometry of human red blood cells. Figure 6.1 shows this evolution over time using the present numerical model. The cross section of the vesicle in the final equilibrium shape clearly demonstrates the formation of the biconcave shape.

(a)   (b)

(c) $t = 0.0$ (d) $t = 1.2$
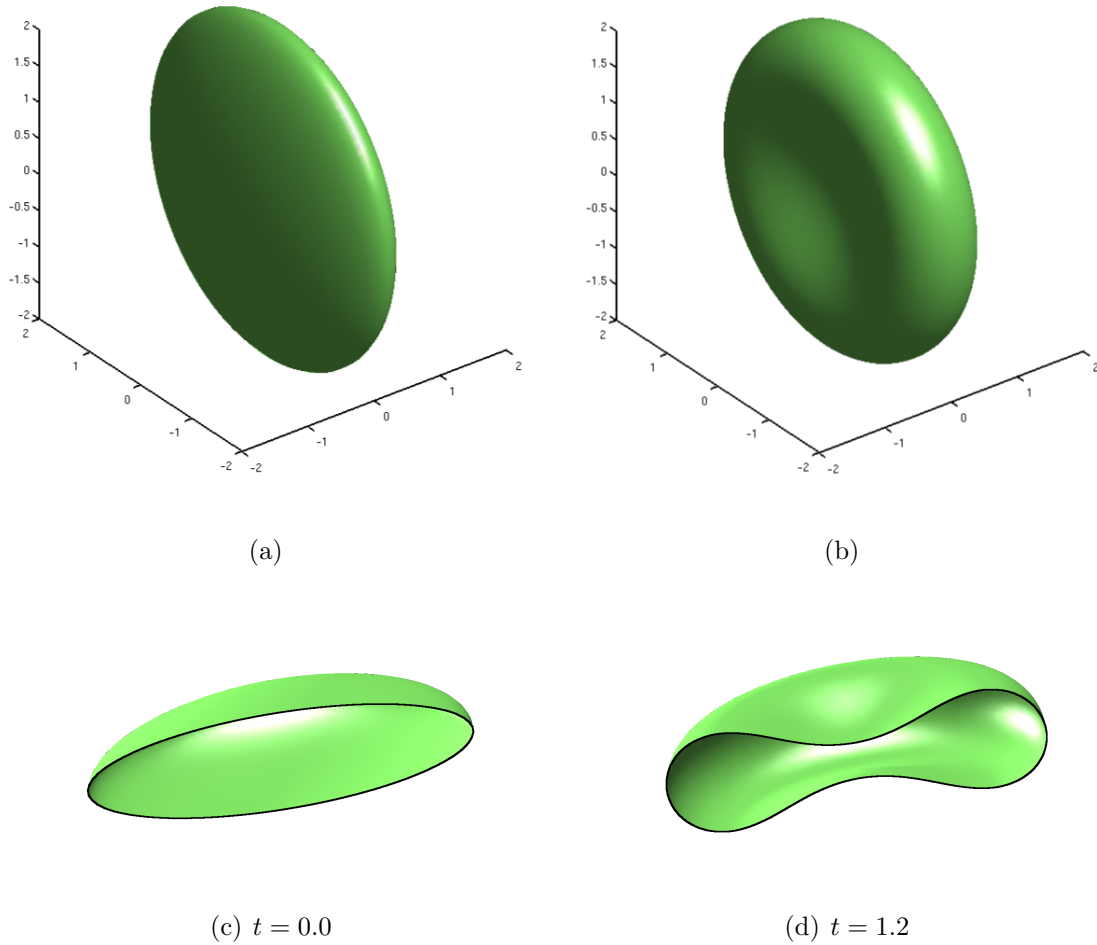
Figure 6.1: The equilibrium biconcave shape of a free vesicle with a reduced volume of $v = 0.6$ and $\eta = 1$ suspended in an initially quiescent flow. The non-dimensional parameters are $Ca = 1.0$ and $Re = 0.001$

6.2   Vesicle Dynamics Under Linear Shear Flow

Two major modes of motions for the vesicle in shear flow are investigated: tank-treading and tumbling. The tank-treading motion happens if the viscosity ratio, η, is less than a critical value η_c, which depends on the reduced volume of the vesicle [9]. In the tank-treading regime the vesicle reaches an equilibrium angle and stays at that position. When the viscosity ratio is above the critical viscosity the behavior of the vesicle changes, and it starts to tumble end-over-end. Studies have shown that

the dynamics depend primarily on the viscosity ratio, η and the reduced volume, v, with no remarkable dependence on the shear rate strength, χ [93].

Sample tank-treading results are illustrated in Fig. 6.2(a) for two initial conditions: a disk-like vesicle and an ellipsoidal vesicle. Both initial conditions have the same reduced volume of $v = 0.85$ and the dimensionless shear rate at the boundary is set to $\chi = 1$. The viscosity ratio is set to $\eta = 1.0$ and other dimensionless parameters are $Ca = 10$ and $Re = 0.001$. The inclination angle with respect to the shear-flow axis, θ, the semi-major axis L, semi-minor axis B, and the half axis length in the vorticity direction, Z, are reported. These values are computed through the use of the inertia matrix of the vesicle [37]. The eigenvalues of the inertia matrix correspond to the axis lengths, while the angle between the eigenvector associated with the largest eigenvalue and the $y-$axis is the inclination angle. It is clear from Fig. 6.2(a) that both initial conditions result in the same equilibrium shape and inclination angle. Figure 6.2(b) shows the fluid circulation being formed in the interior of the vesicle at the equilibrium state. The streamlines demonstrate that the fluid velocity is tangent to the membrane which indicates the tank-treading behavior.
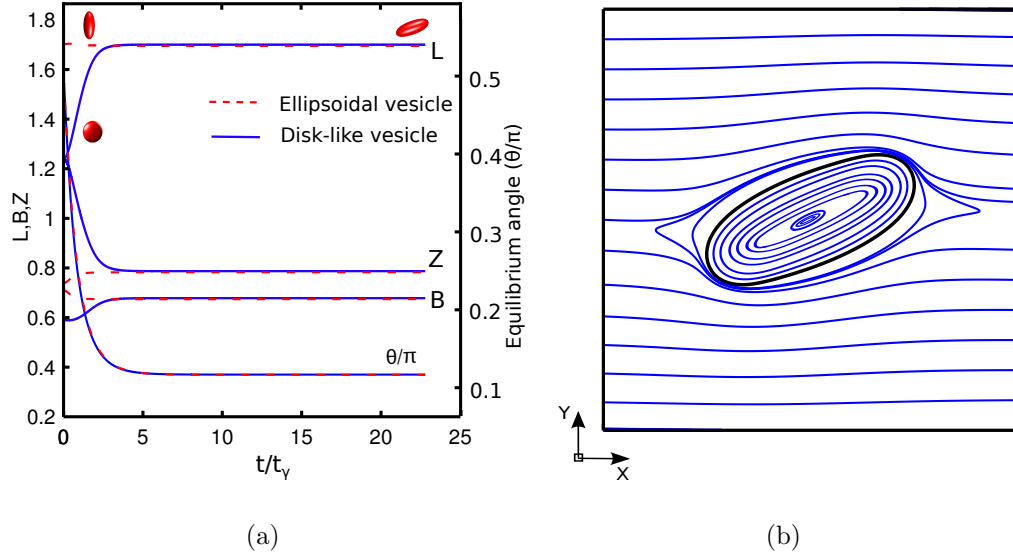
Figure 6.2: Sample result of tank treading vesicle with different initial shapes. Both vesicles have the same reduced volume ($v = 0.85$) and the viscosity ratio is $\eta = 1.0$. (a) The final equilibrium shape and angle are the same for both initially prolate and oblate vesicles. (b) Streamlines for the vesicle in the equilibrium condition. Notice the stable tank-treading configuration and formation of a vortex in the interior of the vesicle.

The snapshots of the three dimensional disk-like vesicle (previously given in Fig. 6.2) are shown in Fig. 6.3 at different times. The vesicle relaxes to an ellipsoid with an inclination angle θ with respect to the y axis. At the inclination angle the vesicle slightly stretches due to the effect of the external shear flow and then stays at that shape and position permanently.

(a) $t = 0$ (b) $t = 0.84$

(c) $t = 4.68$ (d) $t = 9.36$
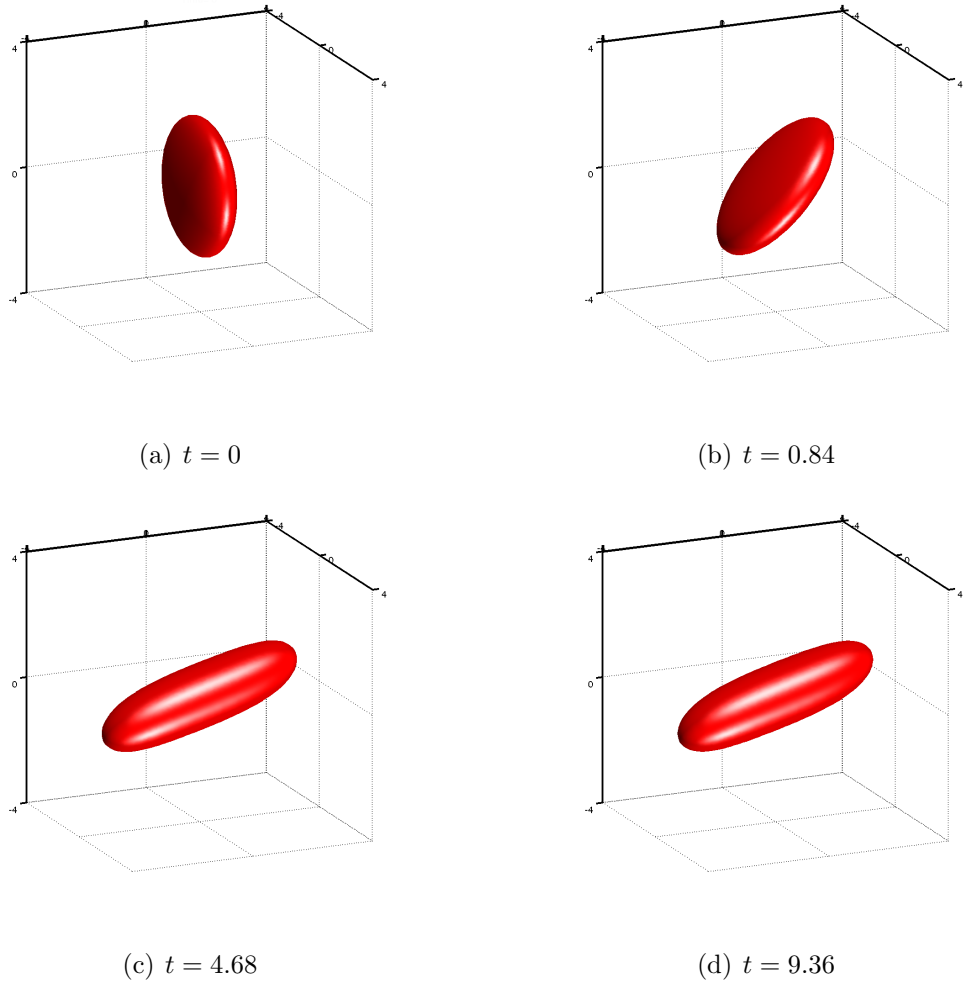
Figure 6.3: Snapshots of three-dimensional tank-treading vesicle in linear shear flow at different times. The vesicle is described by $v = 0.85$ and $\eta = 1.0$

The equilibrium inclination angle as a function of reduced volume and viscosity ratio is shown in Fig 6.4(a). A dimensionless shear rate of $\chi = 1$ is applied at the boundary and results are compared to experimental data from Ref. [103]. The angles from the numerical model are in good agreement with experimental measurements. Small discrepancies in the case of $\eta = 4.9$ could be related to the role of thermal fluctuations in the dynamics of vesicles with larger viscosity ratios [103]. This effect is absent in the proposed model and further investigation is needed to fully understand this phenomena.

The transition between tank-treading and tumbling happens at the critical viscosity ratio η_c. As v increases a larger η_c is required to transition from tank-treading to tumbling. This behavior is shown in Fig 6.4(b). The present method compares well to experimental data from [28], particularly for larger reduced volumes.
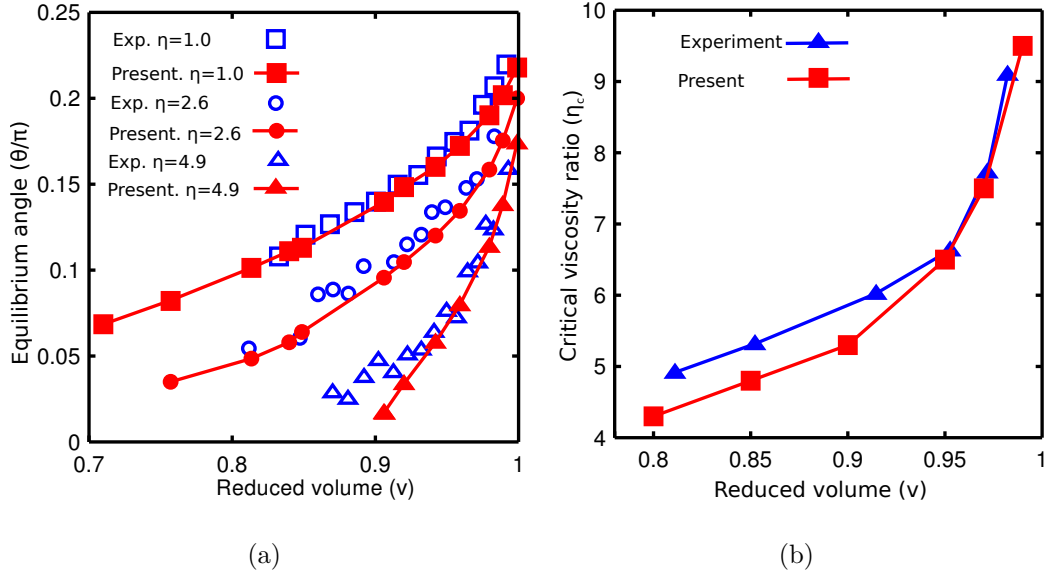
Figure 6.4: Comparison of vesicle hydrodynamics to experiments. (a) The effects of reduced volume and viscosity ratio on the inclination angle of a tank-treading vesicle. The results are compared against the experimental data from Ref. [103]. (b) The critical viscosity ratio for vesicles with various reduced areas. The results are compared to the experimental data in Ref. [28].

Three dimensional snapshots of the tumbling vesicle is shown in Fig. 6.5 at different times. The vesicle has a reduced volume of $v = 0.85$ and a viscosity ratio of $\eta = 8$ is used. In the tumbling regime the vesicle experiences a flipping periodic motion. The comparison of Figs. 6.3 and 6.5 clearly shows the importance of the viscosity contrast in the dynamics of the vesicle and switching from tank-treading regime to tumbling regime.

(a) $t = 0$ (b) $t = 8.4$

(c) $t = 12.6$ (d) $t = 21.6$
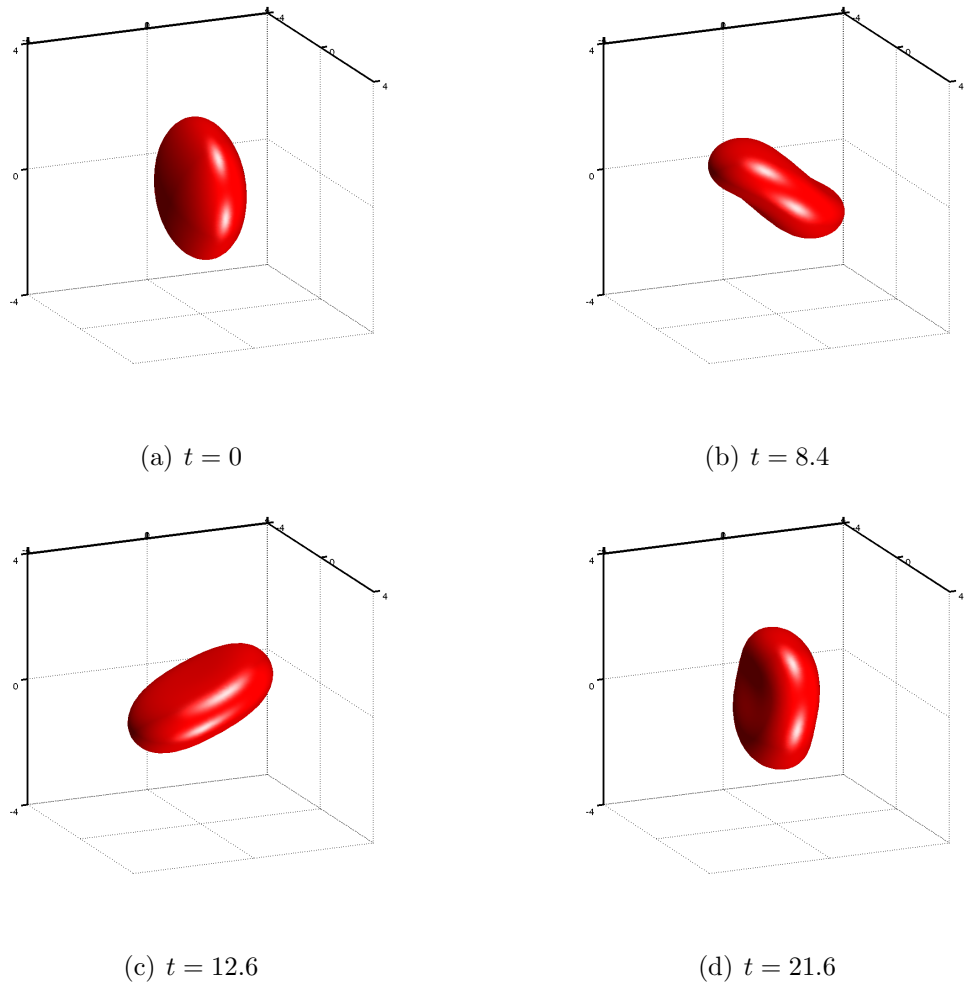
Figure 6.5: Snapshots of three-dimensional tumbling vesicle in linear shear flow at different times. The vesicle is described by $v = 0.85$ and $\eta = 8$.

Changes in volume and area of this tumbling vesicle are given in Fig. 6.6(a) as a percent error with regard to the initial area and volume. There is an excellent conservation of both area and volume, and the percent errors never exceed 0.01% over time. The inclination angle of the same vesicle in Fig. 6.6(b) distinctly illustrates the flipping periodic motion of the vesicle. Fig 6.6(c) shows the time evolution of the semi-major axis L, the semi-minor axis B and the half of the axis length in the vorticity direction Z. Starting from a vesicle with a shape of a disk (identical semi-major and minor axes at the beginning) the axis length in the vorticity direction

remains almost constant during the course of the simulation while there is a periodic change in the length of the other two axes.
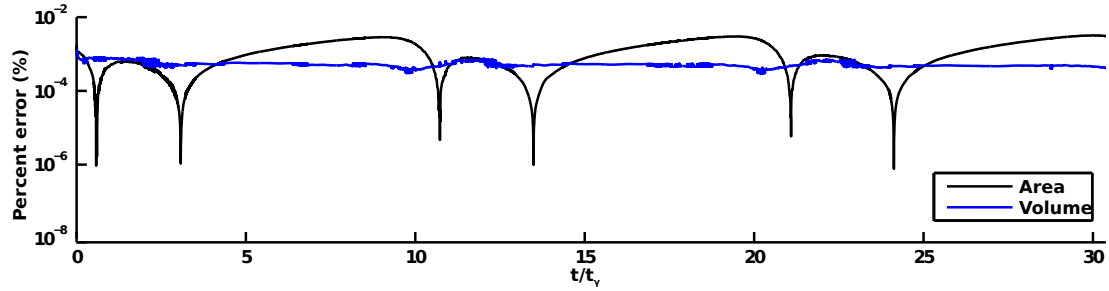
(a)
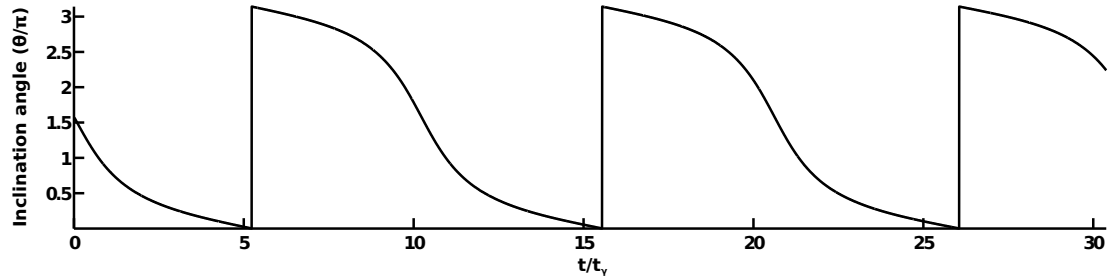
(b)
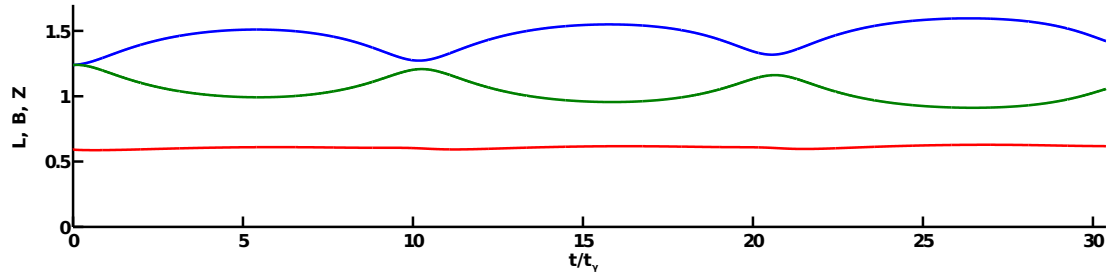
(c)

Figure 6.6: Tumbling of the initial disk-like vesicle described by $v = 0.85$, $\eta = 8$, $Re = 0.001$ and $Ca = 10$. (a) The errors of the volume and area of the vesicle as a percentage of the initial area and volume. (b) The inclination angle of the vesicle in the tumbling regime. The vesicle undergoes a periodic flipping motion over time. (c) The semi-major axis, semi-minor axis and the half of the axis length in the vorticity direction over time.

Chapter 7

Results: Electrohydrodynamics of the Vesicle

The response of a vesicle to an external electric field will depend on a number of factors, including the membrane properties, the viscosity ratio, the electrical properties of the fluids, and the applied electric field. The shape of the vesicles is described by the deformation parameter:

$$D = \frac{a_y}{a_x},$$ (7.1)

where a_y is the dimension of the vesicle in the direction parallel to the applied electric field (the y-direction) while a_x is the dimension of the vesicle in the direction perpendicular to the electric field, the x-direction. An oblate shape is given by $D < 1$ while a prolate shape has $D > 1$. Note that in this chapter these parameters are being calculated directly using the interface location and differ from the calculations of the semi-axis values in chapter 6.

Similar to chapter 6 the vesicle surface area is fixed to 4π in all the simulations. A periodic boundary condition is assumed in the x- and z-directions while wall boundary conditions are given in the y-direction. The computational domain is a box with the

size of $[-4.5, 4.5]^3$, the grid spacing is $h = 0.075$ and a time-step of $\Delta t = 0.0005$ is used in all the simulations. A grid sensitivity study, temporal convergence study and an analysis of the confinement effects are carried out in this chapter to ensure the deformations are consistent over time.

7.1   Vesicle suspended in a viscous fluid

In the absence of an external shear flow ($\chi = 0$) if the conductivity of the inner fluid is lower than the outer fluid ($\lambda < 1$) and the electric field is strong enough such that $t_{ehd} < t_m$, then an initially prolate vesicle will undergo a prolate-oblate-prolate (POP) transition [75, 79]. In an experimental setting, capturing the oblate-to-prolate transition is not trivial [75]. Membranes can easily porate along the way and short-circuit the capacitor. In fact, a precise control over the strength of the field seems to be crucial since a pulse could either be too weak to observe the oblate-prolate transition or lead to poration before the transition happens. To the best of the author's knowledge, no full prolate-oblate-prolate transition has been reported using a single pulse. Hence the deformations are compared to the analytic work of Schwalbe *et. al.* [79] which is based on small amplitude perturbation analysis using spherical harmonics and is developed to only model nearly spherical vesicles.

7.1.1   Comparison against theoretical models

Consider a vesicle with a reduced volume of $v = 0.98$. The initial shape is given by a second-order Spherical Harmonics parametric surface, see Ref. [79] for details. In Figs. 7.1-7.3 the influence of the time step, grid size, and domain size is explored and results are compared to Ref. [79]. Note that the membrane charging time is chosen as the characteristic time in these simulations. Recall that using the typical experimental values of the physical parameters discussed earlier in chapter 2 this

results in $t_0 = t_m = 2.1 \times 10^{-3}$ s, $\hat{C}_m = 0.095$, $\hat{G}_m = 0$, $Re = 0.19$, $Ca = 3.8 \times 10^4$, $Mn = 18$, $E_0 = 1$, and $\chi = 0$. Also a matched dielectric ratio is used in all the electrohydrodynamic simulations in this work.
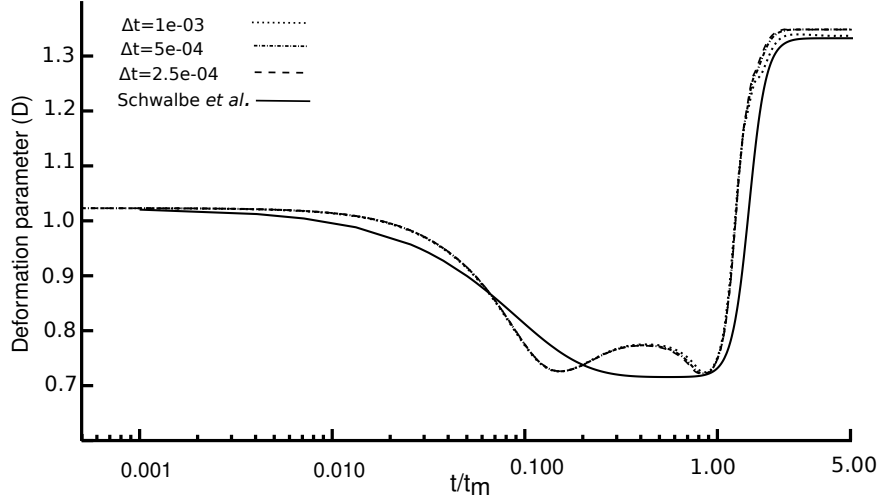
Figure 7.1: Comparison of the method against analytic solution of Schwalbe *et. al.* [79]. Convergence test is done for three different time steps to check the temporal independence. The domain size is $[-4.5, 4.5]$ with a grid spacing of $h = 0.075$. The analysis demonstrates that $\Delta t = 5 \times 10^{-4}$ is the maximum acceptable time-step.
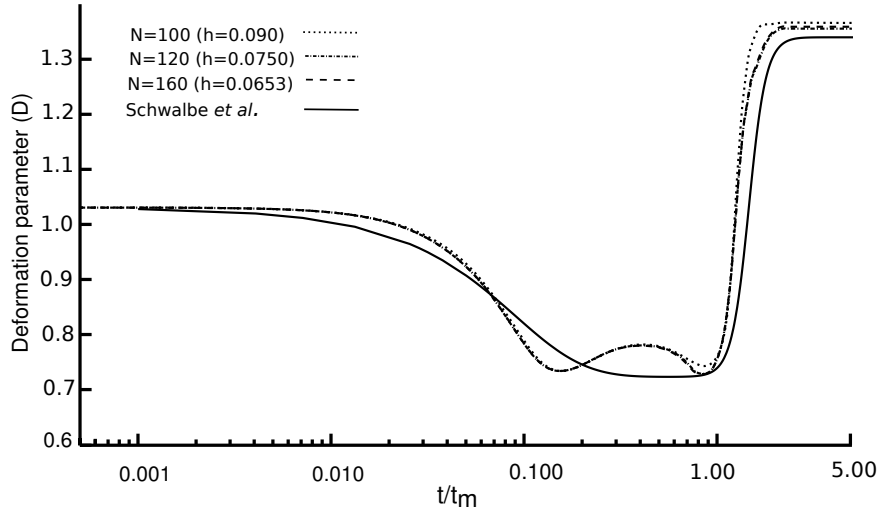
Figure 7.2: Comparison of the method against analytic solution of Schwalbe *et. al.* [79]. Convergence test is done for three different grid spacing to check the grid independence. The domain size is $[-4.5, 4.5]$ and the time step is set to $\Delta t = 5 \times 10^{-4}$. The investigation reveals that that $h = 0.075$ is the maximum acceptable grid spacing.
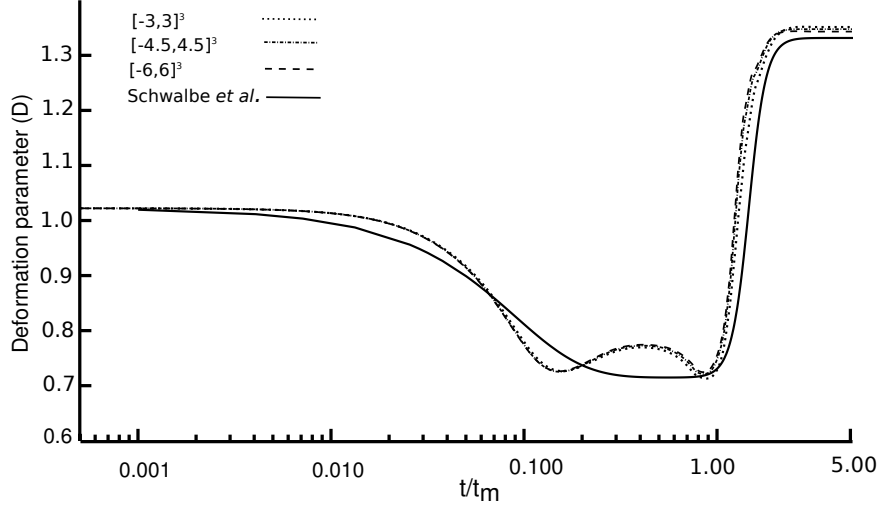
Figure 7.3: Comparison of the method against analytic solution of Schwalbe *et. al.* [79]. Convergence test is done for three different domain sizes to check the domain confinement effect. The grid spacing is $h = 0.075$ and the time step is set to $\Delta t = 5 \times 10^{-4}$. Numerical results shows that $[-4.5, 4.5]$ is the smallest acceptable domain size.

Several points need to be made about the results. First, the use of a time step of size $\Delta t = 5 \times 10^{-4}$, grid size of $N = 120^3$ with a domain of $[-4.5, 4.5]^3$ results in a converged solution and is therefore used in the following simulations. Second, there is a discrepancy between the simulation results and the analytic results of Schwalbe *et. al.* While the general results are similar, for example the approximate time at which the prolate-oblate transition occurs and the time in the oblate shape, there are important differences. The transition from the initial prolate to oblate shape is delayed and is sharper for the current simulation versus the analytic result. Also, the deformation parameter increases slightly during the oblate shape (at a time of $0.4t_m$) before decreasing again. Finally, the final equilibrium shape is slightly different between the two methods, as demonstrated by the difference in the final deformation parameter. This difference is most likely due to the use of a mode-2 spherical harmonic description of the interface in the analytic work. The current simulation has access to a wider range of vesicle shapes than the analytic work and thus additional deformation modes will be accessible. This can be seen by comparing the cross-section of the vesicle

96

in the $x - y$ plane for the two results, Fig. 7.4. The analytic works always remains ellipsoidal in shape while the numerical simulation developed here demonstrates the availability of additional shapes. The other possible explanation for the discrepancy between the two results would be related to the use of Stokes assumption in the analytic solution. The present method uses a full Navier-Stokes solver and therefore possible inertia effects are taken into account.

(a) $t/t_m = 0$ (b) $t/t_m = 0.06$ (c) $t/t_m = 0.14$ (d) $t/t_m = 0.50$

(e) $t/t_m = 0.90$ (f) $t/t_m = 1.20$ (g) $t/t_m = 2.90$ (h) $t/t_m = 5.00$
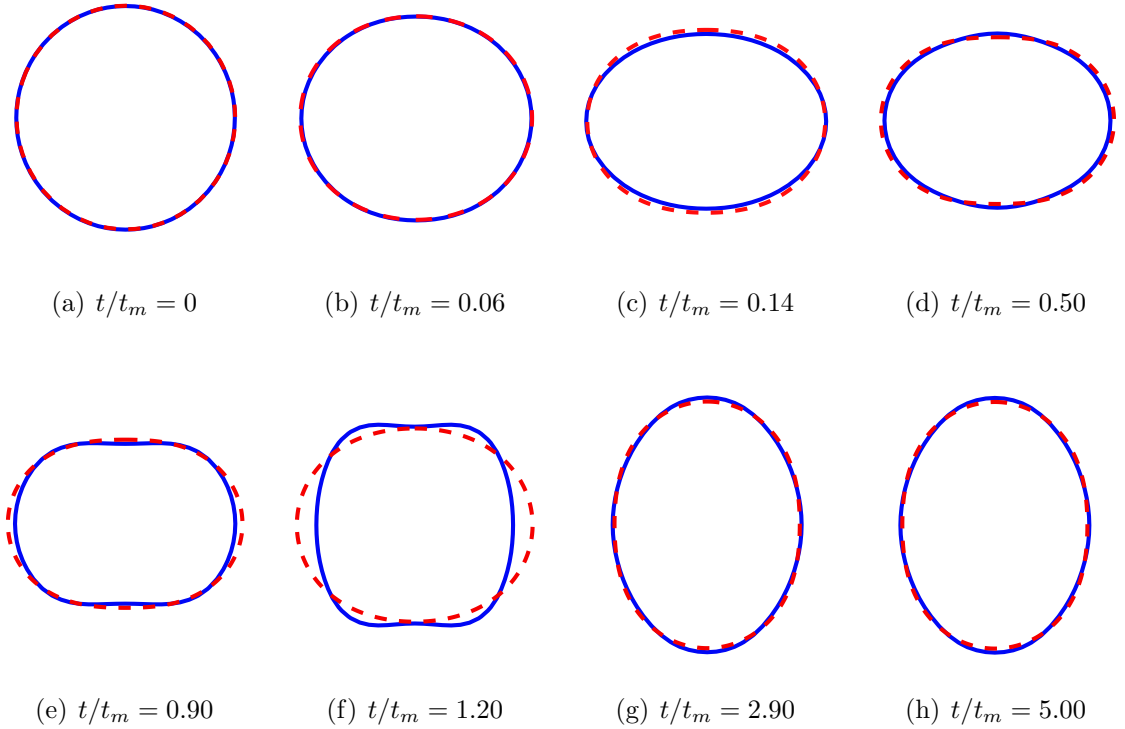
Figure 7.4: Contours of vesicle shape in the x-y plane over time. The solid blue line is the solution of the present method while the dashed red line shows the solution of Schwalbe *et. al.* [79]. A clear difference is observed in the oblate-prolate transition between the two solutions. While the analytic shape remains ellipsoidal during the evolution, the current method predicts a nearly cylindrical deformation for the vesicle.

7.1.2 Full analysis of the POP transition

To demonstrate the axisymmetric POP behavior for vesicles with smaller reduced volumes an initially prolate vesicle with reduced volume of $v = 0.93$ and matched

viscosity ($\eta = 1$) is placed in a strong electric DC field. All the dimensionless param-
eters except for the Mn are the same as before. To ensure the full POP transition for
the more deflected vesicle the Mason number is set to $Mn = 35$. The electrohydro-
dynamic time for this situation is computed as $t_{ehd} = 1.2 \times 10^{-4}s < t_m$ and therefore
the POP transition is expected. Three-dimensional results are shown in Fig. 7.5 at
various time during the evolution. The trans-membrane potential on the interface is
also shown, which demonstrates the charging process.

(a) $t/t_m = 0$ (b) $t/t_m = 0.25$ (c) $t/t_m = 0.35$ (d) $t/t_m = 0.65$

(e) $t/t_m = 1.00$ (f) $t/t_m = 1.40$ (g) $t/t_m = 2.50$ (h) $t/t_m = 5.00$
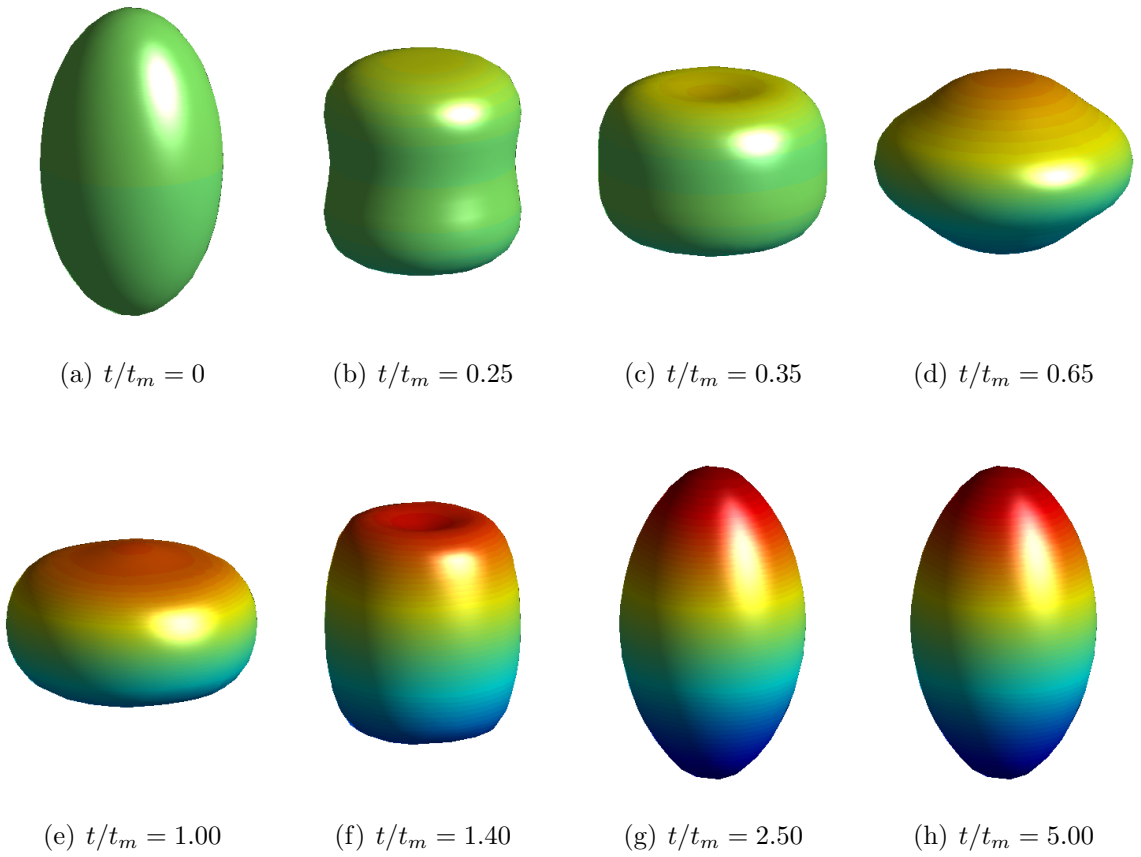
Figure 7.5: POP transition for the vesicle exposed to strong uniform DC electric field.
The vesicle has a reduced volume of $v = 0.93$, membrane capacitance of $\hat{C}_m = 0.095$
and conductance of $\hat{G}_m = 0$. The fluid conductivity ratio is $\lambda = 0.1$ with matched
viscosity and dielectric ratios. The dimensionless parameters are given as $Mn = 35$,
$Re = 0.19$ and $Ca = 38000$. The colors indicate the trans-membrane potential, with
blue (bottom of vesicle) indicating a membrane potential of $V_m = -1.6$ and red (top
of vesicle) indicating a membrane potential of $V_m = -1.6$.

The results clearly demonstrate the transition from a prolate shape to an oblate shape, and then back up to prolate. The initial prolate-oblate transition occurs at about the membrane charging time. This type of behavior has been previously predicted numerically [79, 53] and verified experimentally [75]. The cylindrical deformations observed in two-dimensional vesicle electrohydrodynamic simulations is also observed [53]. It is worth noting that the dimple at the center of the vesicle seen at times $0.35 \ t_m$ and $1.40 \ t_m$ are more pronounced than in the two-dimensional simulations. This could be due to the different parameters used here and the fact that three-dimensional vesicles are typically more flexible due to the additional curvatures and deformation modes.

The area and volume were also tracked during this symmetric POP simulation and the errors, as a percentage of the initial area and volume, is given in Fig. 7.6. As can be seen both the area and volume are conserved extremely well.
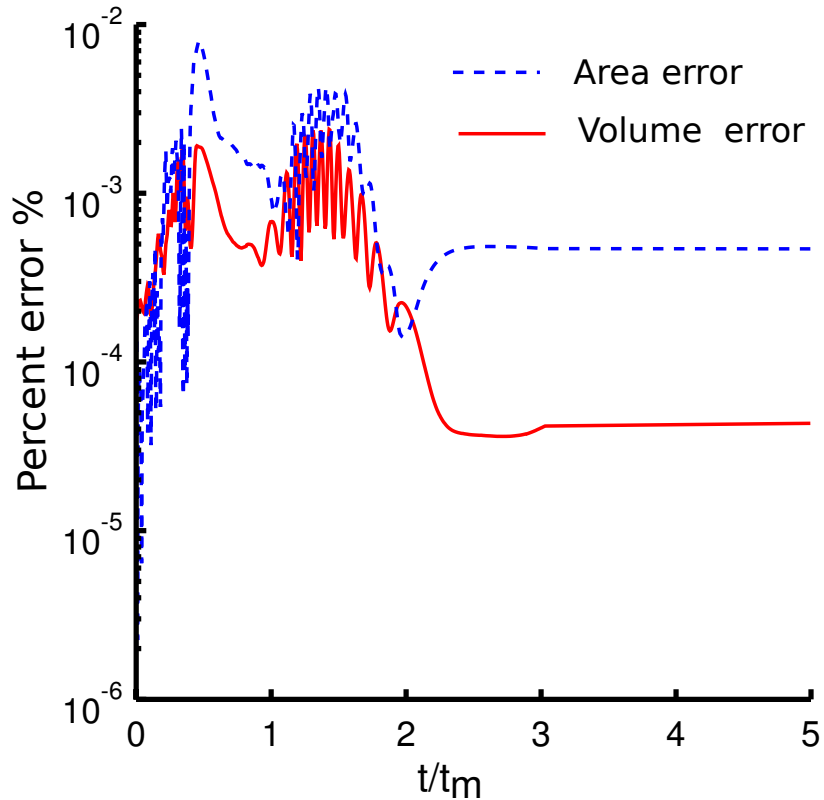
Figure 7.6: Conservation of the area and volume of the vesicle during the POP transition given in Fig. 7.5. The percent errors never exceed 0.01% over time.

The effect of the viscosity ratio

The methods developed here allow for differing viscosity between the inner and outer fluids. As has been demonstrated previously an increase in the viscosity ratio can dramatically change vesicle dynamics in the absence of electric fields. Here the result seen in Fig. 7.5 is compared to a vesicle with the same parameters except that the viscosity ratio is increased to $\eta = 2$. The resulting deformation parameter evolution is presented in Fig. 7.7. The increase in the viscosity ratio results in a vesicle which no longer undergoes a full prolate-oblate-prolate transition. Instead, the higher viscosity vesicle has a slight flattening, but never reaches an oblate shape. In both cases the final equilibrium shape is the same.
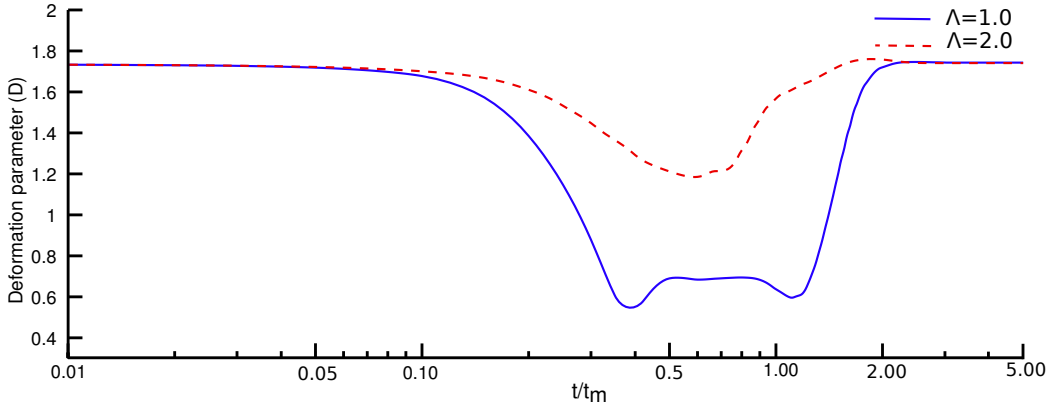
Figure 7.7: The effect of viscosity ratio on the dynamics of the vesicle. The solid line shows the deformation parameter for a vesicle with the parameter set given as $\hat{C}_m = 0.095$, $\hat{G}_m = 0$, $Mn = 35$, $Re = 0.19$, $Ca = 38000$ and $\lambda = 0.1$. This is compared against a vesicle with the same conditions but a viscosity ratio of $\eta = 2.0$. While a full POP transition is observed for the case with matched viscosity ratio, the vesicle with larger η never evolves into the oblate shape.

A wider range of viscosity ratios are used in Fig. 7.8 to investigate the effect of viscosity ratio on the dynamics of the POP transition. The results show the effect of increasing the viscosity ratio is consistent for larger values and almost a linear behavior is observed between the viscosity ratio and the critical Mn required to observe the full POP transition.
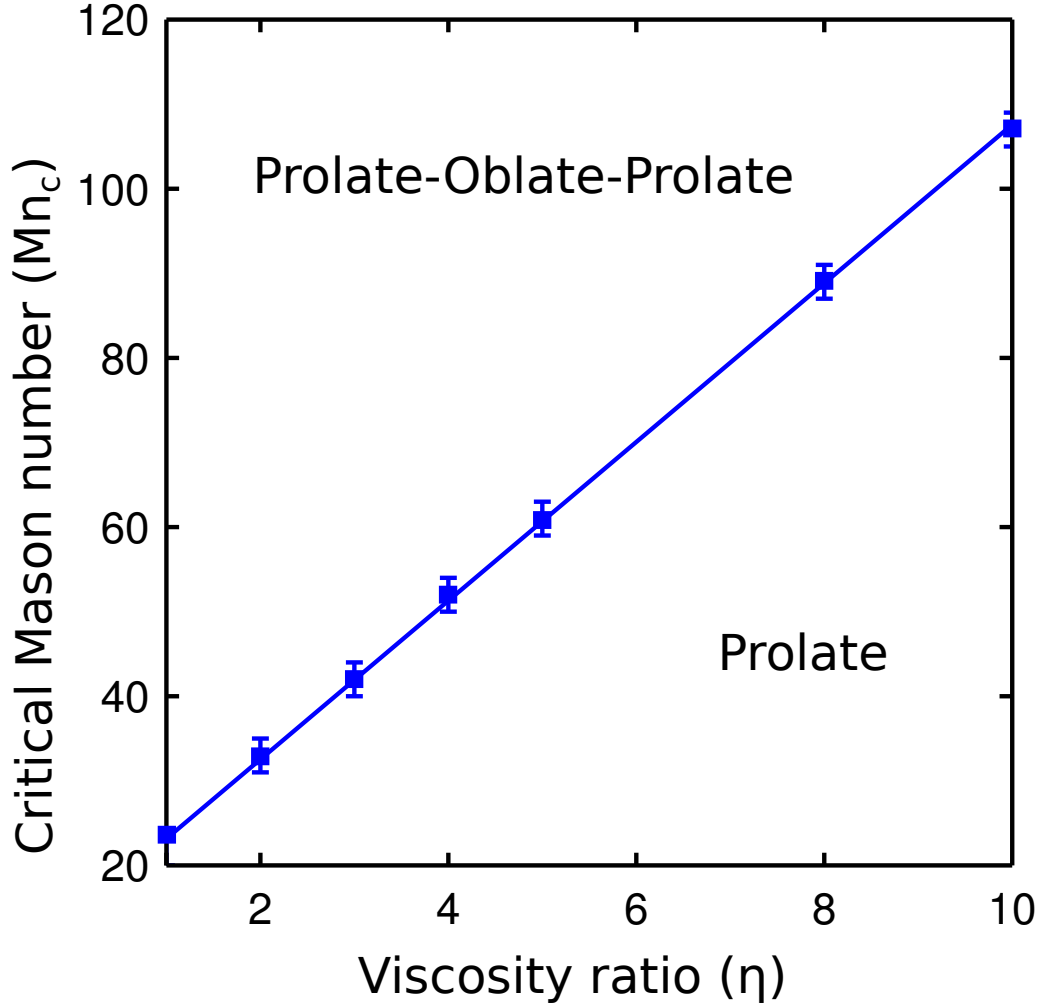
Figure 7.8: Sample parameter study for the effect of viscosity ratio on the dynamics of the vesicle in POP transition. The parameter set are $v = 0.93$, $\hat{C}_m = 0.1$, $\hat{G}_m = 0$, $Re = 0.19$, $Ca = 3.8 \times 10^4$, $E_0 = 1$, and $\chi = 0$. Below a critical electric field strength the vesicle does not undergo a prolate-oblate-prolate transition.

7.2 Vesicle dynamics in combination of shear flow and DC field

When both a shear flow and DC electric field are applied the forces will compete to determine the dynamics of the vesicle. Previous works have demonstrated that electric fields damp the tank-treading and tumbling motion of vesicles in shear flow [79, 53]. If the electric field and shear flow directions are perpendicular the vesicle will

have forces which act in perpendicular directions, leading to a competition between the two forces.

To demonstrate this consider a vesicle with matched viscosity, $\eta = 1$ and a reduced volume of $v = 0.93$ in a normalized shear flow of strength $\chi = 1$. The characteristic time is taken to be the shear flow timescale,$t_0 = t_{\dot{\gamma}} = 1$ s, and thus using standard membrane parameters the dimensionless coefficients become $\hat{C}m = 2 \times 10^{-4}$, $\hat{G}_m = 0$, $Re = 0.001$, and $Ca = 10$. The behavior of this vesicle under the influence of three electric field strengths, $Mn = 0$, $Mn = 3$ and $Mn = 15$ are shown in Fig. 7.9. Note that due to the membrane charging time, $t_m \approx 2.1 \times 10^{-3}$ s, being much faster than the characteristic time it is assumed that the vesicle membrane begins fully charged. During each time step the trans-membrane potential is updated using a sub-step iteration until a pseudo-steady state is reached. As expected the application of an electric field results in the equilibrium inclination angle increasing. A comparison in the $x - y$ plane for the vesicles with $Mn = 0$ and $Mn = 15$ are seen in Fig. 7.10, which clearly demonstrates the higher inclination angle.

Next consider the application of an electric field to a vesicle in the tumbling regime, $\eta = 10 > \eta_c$. The other parameters are the same as the tank-treading case: $v = 0.93$, $\chi = 1$, $\hat{C}m = 2 \times 10^{-4}$, $\hat{G}_m = 0$, $Re = 0.001$, and $Ca = 10$. As in the tank-treading case the trans-membrane potential is iterated until a pseudo-steady state is reached every time step.

In the absence of an electric field the vesicle will tumble end-over-end, with the inclination angle undergoing periodic repetition, Fig. 7.11. The application of a weak electric field, $Mn = 3$ results in periodic behavior more akin to trembling. The vesicle does not undergo a rigid-body-like rotation, but instead the vesicle poles retract and the vesicle reaches a nearly-spherical shape, see Fig. 7.12 for the three-dimensional representation of the vesicle over time. A comparison of the vesicles in the $x - y$ plane at the elevated viscosity ratio for the cases of $Mn = 0$ and $Mn = 3$ is shown in

102
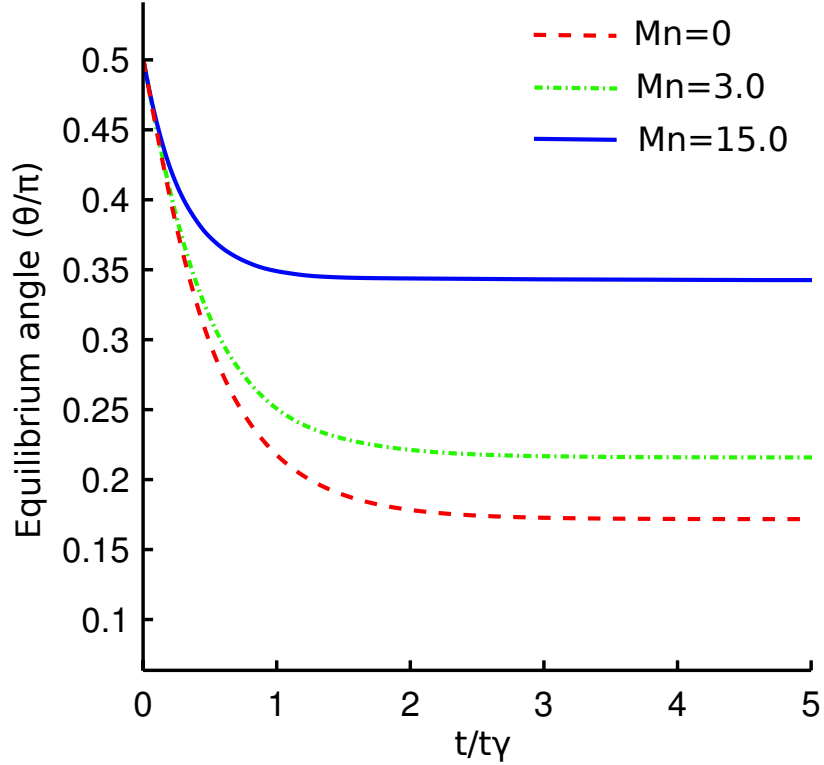
Figure 7.9: The comparison of inclination angle between standard tank-treading vesicle vs. vesicle in the presence of combined shear flow and weak electric fields. All the three cases use a matched viscosity ($\eta = 1$) and a reduced volume of $v = 0.93$. The rest of simulation parameters are $\hat{C}m = 2 \times 10^{-4}$, $Re = 0.001$, $Ca = 10$ and $\chi = 1$. The membrane of vesicles with $Mn \neq 0$ is initially charged. As the strength of the electric field increases the equilibrium vesicle angle increases.

Fig. 7.13. This figure clearly shows the the tumbling behavior is due to membrane deformation and not and end-over-end rotation. As the electric field strength is increases to $Mn = 15$ the vesicle no longer undergoes a tumbling behavior. Instead the vesicle reaches an equilibrium, tank-treading inclination angle.

(a) $t/t_{\dot\gamma} = 0.0$ (b) $t/t_{\dot\gamma} = 0.5$ (c) $t/t_{\dot\gamma} = 1.0$ (d) $t/t_{\dot\gamma} = 5.0$
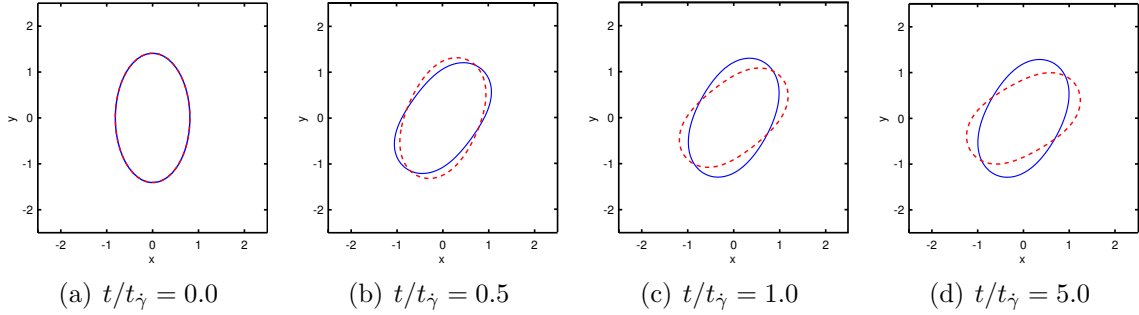
Figure 7.10: The x-y cross section of the vesicle with initially charged membrane, $v = 0.93$ and $\eta = 1$ under combined effect of shear flow and weak DC field with the strength of $Mn = 15$ (the solid blue line). The dynamics is compared against a tank-treading vesicle with no external field, $Mn = 0$ (dashed red line). The rest of the parameters are $\hat{C}m = 2 \times 10^{-4}$, $Re = 0.001$, $Ca = 10$ and $\chi = 1$. The presence of the electric field affects the inclination angle and causes the vesicle to reach the equilibrium condition at a smaller inclination angle. This behavior is due to the vertical alignment of the electric field in the y direction. The electric field force induces a resistance against any angular movement about the initial vertical position of the vesicle.
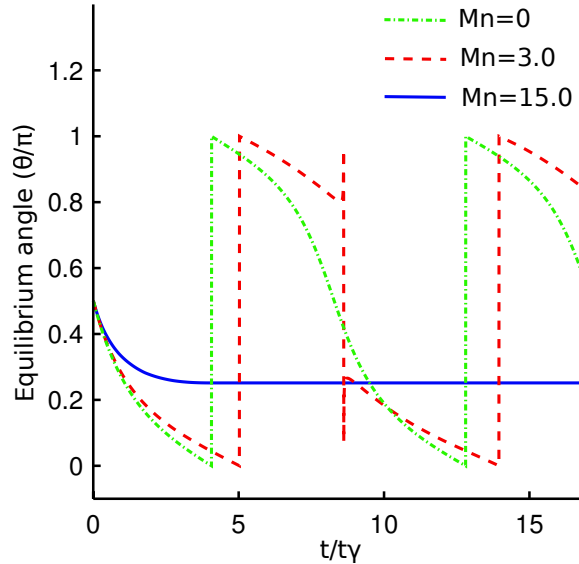
Figure 7.11: The comparison of dynamics between the standard tumbling vesicle vs. vesicle in the presence of combined shear flow and weak electric fields. All the three cases use a viscosity ratio of $\eta = 10$ and a reduced volume of $v = 0.93$. Other parameters are $\hat{C}m = 2 \times 10^{-4}$, $Re = 0.001$, $Ca = 10$ and $\chi = 1$. The membranes of vesicles with $Mn \neq 0$ are initially charged. Compared to the standard tumbling case, the simulation with $Mn = 3$ shows a lagged tumbling behavior and experiences a lot more topological changes during the transition as it will be illustrated below. An interesting observation has been made for the vesicle with $Mn = 15$. In this situation, the vesicle undergoes a tank-treading motion and stays at that position permanently.

104

(a) $t/t_{\dot{\gamma}} = 0.0$ (b) $t/t_{\dot{\gamma}} = 2.5$ (c) $t/t_{\dot{\gamma}} = 3.5$ (d) $t/t_{\dot{\gamma}} = 6.5$ (e) $t/t_{\dot{\gamma}} = 7.5$

(f) $t/t_{\dot{\gamma}} = 8.5$ (g) $t/t_{\dot{\gamma}} = 10.0$ (h) $t/t_{\dot{\gamma}} = 12.5$ (i) $t/t_{\dot{\gamma}} = 15.0$ (j) $t/t_{\dot{\gamma}} = 17.0$
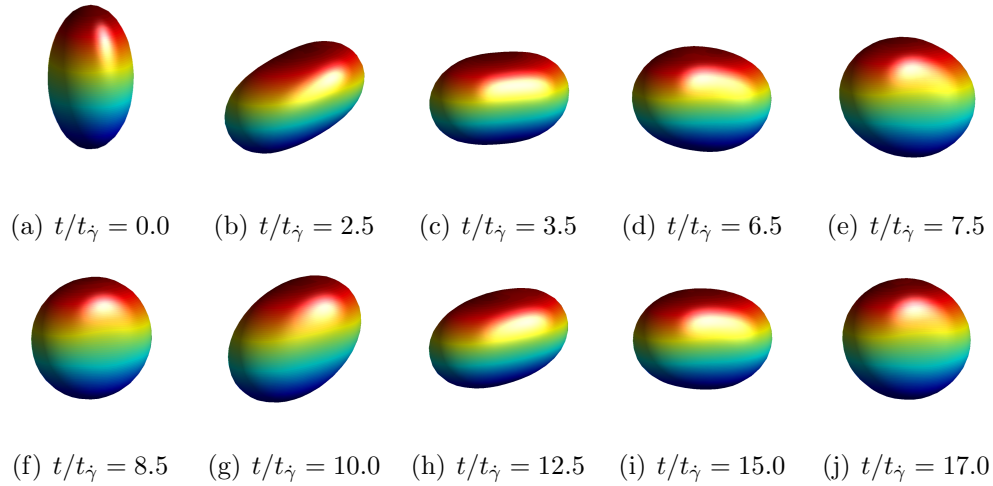
Figure 7.12: Simulation results on the dynamics of the vesicle with initially charged membrane, $v = 0.93$ and $\eta = 10$ under combined influence of shear flow and weak DC field. These results correspond to the case of $Mn = 3$ in Fig. 7.13. The presence of the electric field influences the normal flipping motion of the vesicle. The topological changes between time $t = 6.5$ to $t = 10.0$ show that the vesicle first retracts at the poles prior to getting to the vertical direction and reforms back into the ellipsoidal shape passed the vertical position.

(a) $t/t_{\dot{\gamma}} = 0.0$ (b) $t/t_{\dot{\gamma}} = 2.5$ (c) $t/t_{\dot{\gamma}} = 3.5$ (d) $t/t_{\dot{\gamma}} = 6.5$ (e) $t/t_{\dot{\gamma}} = 7.5$

(f) $t/t_{\dot{\gamma}} = 8.5$ (g) $t/t_{\dot{\gamma}} = 10.0$ (h) $t/t_{\dot{\gamma}} = 12.5$ (i) $t/t_{\dot{\gamma}} = 15.0$ (j) $t/t_{\dot{\gamma}} = 17.0$
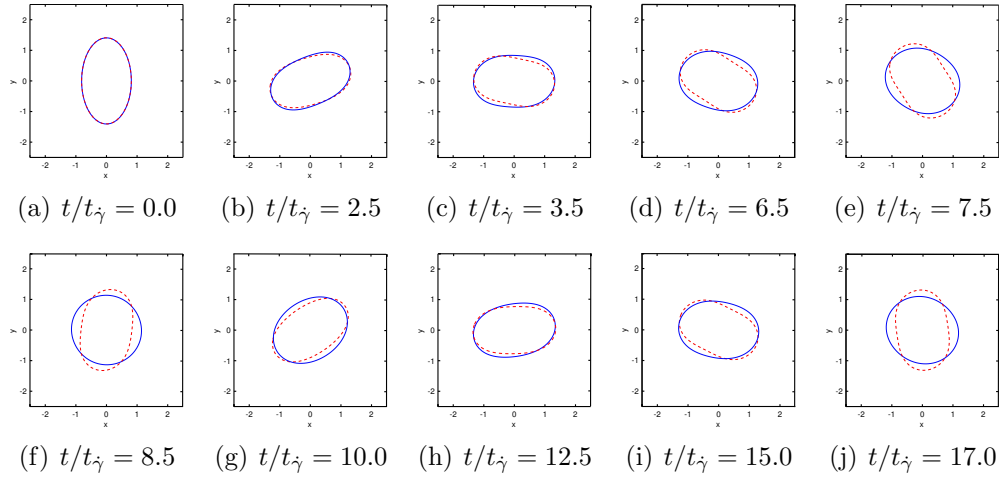
Figure 7.13: The x-y cross section of the vesicle with initially charged membrane and $\eta = 10$ under combined effect of shear flow and weak DC field with the strength of $Mn = 3$ (the solid blue line). The dynamics is compared against a tumbling vesicle with the same viscosity ratio and no external field, $Mn = 0$ (dashed red line). The rest of the parameters are $Re = 0.001$, $Ca = 10$ and $\chi = 1$. The presence of the electric field affects the inclination angle and causes the vesicle to reach the equilibrium condition at a smaller θ. This behavior is due to the vertical alignment of the electric field in the y direction. The electric field force induces a resistance against any angular movement about the initial vertical position of the vesicle.

Chapter 8

Summary and Outlook

In this work, a numerical method was developed to study the electrohydrodynamics of a three dimensional vesicle. This included the investigation of the dynamics in uniform DC electric field and under combined effects of linear shear flow and electric fields. To the best of the author's knowledge, this was the first attempt at numerical modeling of three-dimensional vesicles in the presence of electric fields.

First a physical picture was provided in Chapter 2 by discussing the reasonable assumptions, governing equations and development of a continuum surface force model. The membrane was modeled as a thin capacitive interface with bending and in-extension properties. The force balance between external hydrodynamic and electric field stresses and the membrane forces of bending and tension were modeled by deriving the appropriate body force terms in the Navier-Stokes. This is done by using the properties of the level set and Dirac delta functions.

The trans-membrane potential as a result of the capacitive membrane was implicitly computed along with the solution of domain potential using an Immersed Interface Method. This was achieved by derivation and inclusion of the implicit jump conditions for the electric potential, up to the second normal derivative. This topic

was thoroughly discussed in Chapter 2 and sample convergence results were presented to support the the robustness and accuracy of the method.

The interface location was tracked using a semi-implicit gradient augmented level set method. The method developed in this work is an extension of the original gradient augmented method [56] for nonlinear evolutions and combines the additional accuracy afforded by explicitly tracking gradient information with the stability properties of a semi-implicit scheme. The complete algorithm as well as comprehensive investigation of the method for two and three dimensional nonlinear problems were provided in Chapter 4.

Last but not least in the description of the numerical methodology is the discretization method to solve for the full Navier-Stokes equations including the incompressibility condition of the fluid and the inextensibility of the vesicle membrane. This goal was achieved by introducing a novel projection method which uses a a set of local and global Lagrange multipliers to enforce the necessary conditions in the domain and at the interface of the two fluids. The details of the algorithm and implementation considerations are discussed in Chapter 5.

To verify the hydrodynamic solution, numerical benchmark problems were used to investigate the dynamics of the vesicle in both quiescent and linear shear flows. The results were presented in Chapter 6. The method was found to successfully predict the equilibrium biconcave shape of the vesicle in the absence of imposed shear flow. The two major modes of the vesicle motion in the linear shear flow namely the tank-treading and tumbling regimes were studied as well and the validation of the model was examined in the light of experimental data and observations. Investigations showed that there are very good agreements between the present results and the experimental data.

Lastly, the simulation results of the vesicle electrohydrodynamics were provided in Chapter 7. The type of results presented in this chapter were split into three sections.

In the first section an analytic model developed by Schwalbe *et. al.* [79] was used to compare the deformation of the vesicle against the present results. This was accompanied by a grid sensitivity study, temporal convergence study and an analysis of the confinement effects to ensure the deformations are consistent over time. While a general agreement was found between the the present numerical method and the theoretical model, possible reasons for the discrepancies were discussed. The method developed in this work has the advantage of having access to all the deformation modes unlike the analytic solution. In addition, due to the fast dynamics of the vesicle in the presence of strong fields more accurate dynamics are being expected by employing the full Navier-Stokes equations rather than the Stokes assumption used in the analytical work.

In the second section the topological changes of the vesicle during the prolate-oblate-prolate transition was studied. The simulation was capable of capturing the full prolate-oblate-prolate dynamics observed experimentally and predicted by previous analytic and two-dimensional numeric works. The effect of the viscosity ratio in the occurrence of a full prolate-oblate-prolate transition was investigated as well. Work is currently underway to perform a broader parameter-space study in order to investigate the effects of different material properties of the liquids and the membrane on the prolate-oblate-prolate transition of the vesicle.

In section 7.2 of Chapter 7 the behavior of the vesicle under the combined effects of shear flow and weak DC electric fields were explored. The results showed the remarkable influence of the electric field in changing the standard behaviors of tank-treading and tumbling vesicles. If the electric field is strong enough the induced resistance caused by the electric field may alter the behavior of a tumbling vesicle into a tank-treading motion.

Future work will use the method developed here to perform a more detailed investigation on how electric fields, fluid flow, and material parameters can be used to

influence dynamics of the vesicle. Practical approximations of the critical parameter thresholds such as the strength of the field or applied shear rate can be used as a useful tool in the vesicle manipulation and sorting applications.

This research is a step in the path to understand the more complex physics of multicomponent lipid membranes and predict challenging interfacial phenomena such as electroporation in the context of their biological applications. Although the model presented in this research is restricted to closed-surface membranes, much information can be still extracted from mpresent results to gain insight into identifying regions with high prevalence of pore formation. When a strong electric field is applied to a vesicle, surface tension forces appear as the dominant resisting forces of the membrane against the external fluid flow and electric field stresses. Therefore, one would expect for the poration to happen in regions with higher tension values. This seems to be the case according to experimental observations [76]. However, as soon as the vesicle porates new considerations need to be taken into account including initiation of a line tension and inhomogeneous conductivity of the charge at the pore location.

Appendix A

Proof of the CSF formulation

Consider an arbitrary region Ω surrounding the vesicle. We decompose Ω into two regions Ω^- and Ω^+ for the surrounding and enclosed fluids respectively (Figure A.1). The standard integral forms of the momentum equation (2.15) is written for both fluids as

$$\int_{\Omega^-} \rho \frac{D\boldsymbol{u}^-}{Dt} d\boldsymbol{x} = \int_{\Omega^-} \nabla \cdot \boldsymbol{T}_{hd}^- d\boldsymbol{x} \quad in \quad \Omega^-. \tag{A.1}$$

$$\int_{\Omega^+} \rho \frac{D\boldsymbol{u}^+}{Dt} d\boldsymbol{x} = \int_{\Omega^+} \nabla \cdot \boldsymbol{T}_{hd}^+ d\boldsymbol{x} \quad in \quad \Omega^+. \tag{A.2}$$

$$\tag{A.3}$$

From the Divergence theorem

$$\int_{\Omega^-} \rho \frac{D\boldsymbol{u}^-}{Dt} d\boldsymbol{x} = \oint_{\delta\Omega^-} \boldsymbol{T}_{hd}^- \cdot \boldsymbol{dS}. \tag{A.4}$$

$$\int_{\Omega^+} \rho \frac{D\boldsymbol{u}^+}{Dt} d\boldsymbol{x} = \oint_{\delta\Omega_1^+} \boldsymbol{T}_{hd}^+ \cdot \boldsymbol{dS} + \oint_{\delta\Omega_2^+} \boldsymbol{T}_{hd}^+ \cdot \boldsymbol{dS}. \tag{A.5}$$

where $\delta\Omega_1^+$ and $\delta\Omega_2^+$ define the boundaries of Ω^+ while $\delta\Omega^-$ determines the single boundary for the inner region Ω^-. Now for the sake of this proof we make the following two definitions,

$$
\boldsymbol{T} = \begin{cases} \boldsymbol{T}^- & \text{if } \boldsymbol{x} \in \Omega^- \\ \boldsymbol{T}^+ & \text{if } \boldsymbol{x} \in \Omega^+ \end{cases} \qquad \boldsymbol{u} = \begin{cases} \boldsymbol{u}^- & \text{if } \boldsymbol{x} \in \Omega^- \\ \boldsymbol{u}^+ & \text{if } \boldsymbol{x} \in \Omega^+ \end{cases}
$$

From Fig. (A.1) it is clear that $\delta\Omega = \delta\Omega^+$. Using this along with the definition for $\boldsymbol{T}$ we find

$$
\oint_{\delta\Omega_1^+} \boldsymbol{T}_{hd}^+ \boldsymbol{dS} = \oint_{\delta\Omega} \boldsymbol{T}_{hd} \boldsymbol{dS} \tag{A.6}
$$

It should be noted that $\boldsymbol{T}$ is not continuous across the interface. However in the discrete sense we are able to make use of the divergence theorem again and write

$$
\oint_{\delta\Omega} \boldsymbol{T}_{hd} \boldsymbol{dS} = \int_\Omega \nabla \cdot \boldsymbol{T}_{hd} d\boldsymbol{x} \tag{A.7}
$$

Also as it is depicted in Fig. (A.1) one can easily show that

$$
\oint_{\delta\Omega_2^+} \boldsymbol{T}_{hd}^+ \boldsymbol{dS} = - \oint_{\delta\Omega^-} \boldsymbol{T}_{hd}^+ \boldsymbol{dS} \tag{A.8}
$$

Note that the direction of the contours are determined such that as we walk on the boundary the of the domain, the corresponding region falls on our right. Adding up (A.4) and (A.5) and substituting the corresponding terms from (A.7) and (A.8) we get

$$
\begin{aligned}
\int_{\Omega^-} \rho \frac{D\boldsymbol{u}^-}{Dt} d\boldsymbol{x} + \int_{\Omega^+} \rho \frac{D\boldsymbol{u}^+}{Dt} d\boldsymbol{x} &= \int_\Omega \nabla \cdot \boldsymbol{T}_{hd} d\boldsymbol{x} - \oint_{\delta\Omega^-} \boldsymbol{T}_{hd}^+ \boldsymbol{dS} + \oint_{\delta\Omega^-} \boldsymbol{T}_{hd}^- \boldsymbol{dS} \\
&= \oint_{\delta\Omega} \boldsymbol{T}_{hd} \boldsymbol{dS} - \oint_{\delta\Omega^-} [\boldsymbol{T}_{hd}] \cdot \boldsymbol{n} dS
\end{aligned} \tag{A.9}
$$

Since $\boldsymbol{u}^- = \boldsymbol{u}^+$ across the interface, $\boldsymbol{u}$ is a continuous function and we can write

$$
\int_{\Omega^-} \rho \frac{D\boldsymbol{u}^-}{Dt} d\boldsymbol{x} + \int_{\Omega^+} \rho \frac{D\boldsymbol{u}^+}{Dt} d\boldsymbol{x} = \int_\Omega \rho \frac{D\boldsymbol{u}}{Dt} d\boldsymbol{x} \tag{A.10}
$$

Using (A.9) and (A.10) the final integral form of the momentum equation is derived

as

$$\int_\Omega \rho \frac{D\boldsymbol{u}}{Dt} d\boldsymbol{x} = \oint_{\delta\Omega} \boldsymbol{T}_{hd} d\boldsymbol{S} - \oint_{\delta\Omega^-} [\boldsymbol{T}_{hd}] \cdot \boldsymbol{n} dS \qquad (A.11)$$

where as it was previously stated in Eq. (2.17) the term $\boldsymbol{n} \cdot [\boldsymbol{T}_{hd}]$ is given as

$$\boldsymbol{n} \cdot [\boldsymbol{T}_{hd}] = \boldsymbol{\tau}_{hd} = \boldsymbol{\tau}_m + \boldsymbol{\tau}_\gamma - \boldsymbol{\tau}_{el}$$

$$= -\kappa_c (\frac{H^3}{2} - 2HK + \nabla_s^2 H)\boldsymbol{n} + \gamma H \boldsymbol{n} - \nabla_s \gamma - \boldsymbol{n} \cdot [\epsilon(\boldsymbol{E}\boldsymbol{E} - \frac{1}{2}\boldsymbol{E} \cdot \boldsymbol{E}\boldsymbol{I})]$$

$$(A.12)$$

To continue with the proof, we make use of the following relation. Based on the

coarea formula for a continuous function f over the domain Ω we have [99]

$$\int_\Gamma \boldsymbol{f} dS = \int_\Omega | \nabla(\phi) | \delta(\phi) \boldsymbol{f} d\boldsymbol{x}. \qquad (A.13)$$

Now we are able to convert the line integrals in the right hand side of the (A.12) to

integrals over the area Ω by using (A.13) and (A.7) for the terms

$$\int_\Omega \rho \frac{D\boldsymbol{u}}{Dt} d\boldsymbol{x} = \int_\Omega \nabla \cdot \boldsymbol{T}_{hd} d\boldsymbol{x} - \int_\Omega | \nabla\phi | \delta(\phi) \Big(-\kappa_c (\frac{H^3}{2} - 2HK + \nabla_s^2 H)\boldsymbol{n} + \gamma H \boldsymbol{n} - \nabla_s \gamma$$

$$- \boldsymbol{n} \cdot [\epsilon(\boldsymbol{E}\boldsymbol{E} - \frac{1}{2}\boldsymbol{E} \cdot \boldsymbol{E}\boldsymbol{I})] \Big) d\boldsymbol{x} \quad (A.14)$$

Noting that $\boldsymbol{n} = \frac{\nabla\phi}{|\nabla\phi|}$ and rearranging the equation we find

$$\int_\Omega \Big(\rho \frac{D\boldsymbol{u}}{Dt} - \nabla \cdot \boldsymbol{T}_{hd} - \kappa_c \delta(\phi)(\frac{H^3}{2} - 2HK + \nabla_s^2 H)\nabla\phi - \delta(\phi)(| \nabla\phi | \nabla_s \gamma - \gamma H \nabla\phi)$$

$$- \delta(\phi) | \nabla\phi | \boldsymbol{n} \cdot [\epsilon(\boldsymbol{E}\boldsymbol{E} - \frac{1}{2}\boldsymbol{E} \cdot \boldsymbol{E}\boldsymbol{I})] \Big) d\boldsymbol{x} = 0. \quad (A.15)$$

This relation holds for the arbitrary domain Ω. Therefore we can write

$$
\begin{aligned}
\rho \frac{D\boldsymbol{u}}{Dt} = & -\nabla p + \nabla \cdot (\mu(\nabla \boldsymbol{u} + \nabla^T \boldsymbol{u})) \\
& + \delta(\phi)\left(\mid \nabla\phi \mid \nabla_s \gamma - \gamma H \nabla \phi \right) \\
& + \kappa_c \delta(\phi)\left(\frac{H^3}{2} - 2KH + \nabla_s^2 H \right) \nabla \phi \\
& + \delta(\phi) \mid \nabla\phi \mid \boldsymbol{n} \cdot \left[\epsilon(\boldsymbol{E}\boldsymbol{E} - \frac{1}{2}\boldsymbol{E} \cdot \boldsymbol{E}\boldsymbol{I}) \right]
\end{aligned}
\tag{A.16}
$$
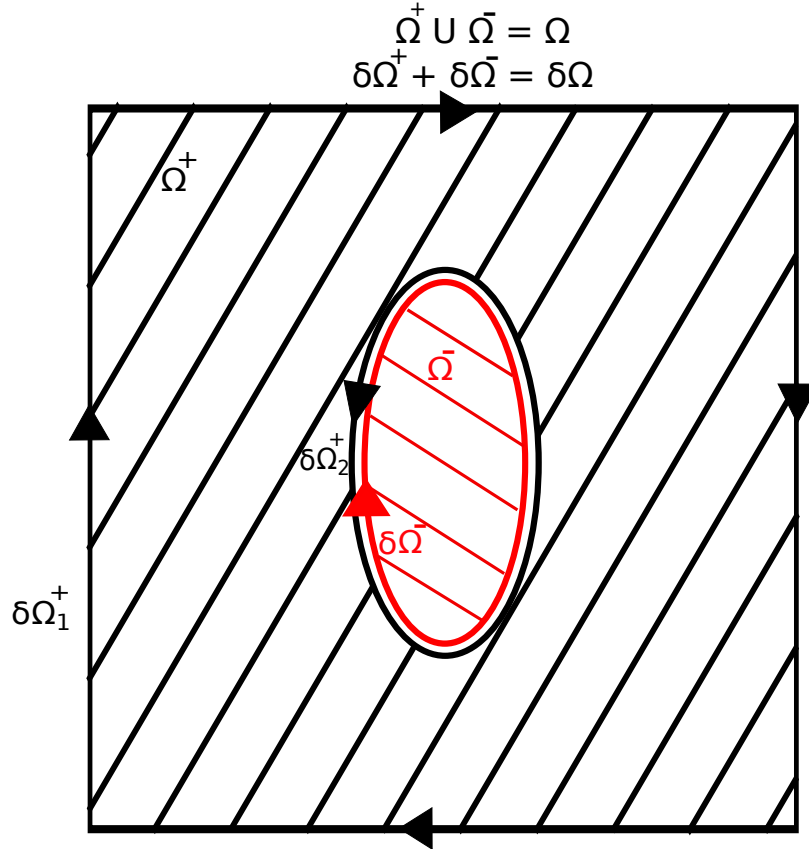
Figure A.1: Schematic of a portion of the fluid including the vesicle

Bibliography

[1] Manouk Abkarian, Colette Lartigue, and Annie Viallat. Tank treading and unbinding of deformable vesicles in shear flow: determination of the lift force. *Physical review letters*, 88(6):068103, 2002.

[2] Manouk Abkarian and Annie Viallat. Vesicles and red blood cells in shear flow. *Soft Matter*, 4(4):653, 2008.

[3] Loyce Adams and Zhilin Li. The immersed interface/multigrid methods for interface problems. *SIAM Journal on Scientific Computing*, 24(2):463–479, 2002.

[4] Sebastian Aland, Sabine Egerer, John Lowengrub, and Axel Voigt. Diffuse interface models of locally inextensible vesicles in a viscous fluid. 2013.

[5] Bruce Alberts, Alexander Johnson, Julian Lewis, Martin Raff, Keith Roberts, and Peter Walter. *Molecular biology of the cell*. Garland Science, forth edition, 2002.

[6] Theresa M. Allen and Pieter R. Cullis. Drug delivery systems: Entering the mainstream. *Science*, 303(5665):pp. 1818–1822, 2004.

[7] T Baumgart, S Das, WW Webb, and JT Jenkins. Membrane elasticity in giant vesicles with fluid phase coexistence. *Biophysical journal*, 89(2):1067–1080, 2005.

[8] J. Beaucourt, F. Rioual, T. Séon, T. Biben, and C. Misbah. Steady to unsteady dynamics of a vesicle in a flow. *Physical Review E*, 69(1):011906, January 2004.

[9] T Biben and C Misbah. Tumbling of vesicles under shear flow within an advected-field approach. *Physical Review E*, 67(3):031908, 2003.

[10] Thierry Biben, Alexander Farutin, and Chaouqi Misbah. Three-dimensional vesicles under shear flow: Numerical study of dynamics and phase diagram. *Physical Review E*, 83(3):031921, March 2011.

[11] Thierry Biben, Klaus Kassner, and Chaouqi Misbah. Phase-field approach to three-dimensional vesicle dynamics. *Physical Review E*, 72(4):041921, 2005.

[12] Givaat Ram Campus. Irreversible electroporation: a new ablation modality–clinical implications. *Technology in cancer research & treatment*, 6(1), 2006.

[13] Y.C. Chang, T.Y. Hou, B. Merriman, and S. Osher. A level set formulation of eulerian interface capturing methods for incompressible fluid flows. *Journal of Computational Physics*, 124(2):449 – 464, 1996.

[14] Prince Chidyagwai, Jean-Christophe Nave, Rodolfo Ruben Rosales, and Benjamin Seibold. A Comparative Study Of The Efficiency Of Jet Schemes. *Int.J. Numer. Anal. Model.-B*, 3(3):297–306, 2012.

[15] David L Chopp. Some improvements of the fast marching method. *SIAM Journal on Scientific Computing*, 23(1):230–244, 2001.

[16] D.L. Chopp and J.A. Sethian. Motion by Intrinsic Laplacian of Curvature. *Interfaces and Free Boundaries*, 1:1–18, 1999.

[17] Sune M Christensen and Dimitrios Stamou. Surface-based lipid vesicle reactor systems: fabrication and applications. *Soft Matter*, 3(7):828–836, 2007.

[18] KH De Haas, C Blom, D Van den Ende, MHG Duits, and J Mellema. Deformation of giant lipid bilayer vesicles in shear flow. *Physical Review E*, 56(6):7132, 1997.

[19] K a DeBruin and W Krassowska. Modeling electroporation in a single cell. I. Effects Of field strength and rest potential. *Biophysical journal*, 77(3):1213–24, September 1999.

[20] Rumiana Dimova, Karin A Riske, Said Aranda, Natalya Bezlyepkina, Roland L Knorr, and Reinhard Lipowsky. Giant vesicles in electric fields. *Soft matter*, 3(7):817–827, 2007.

[21] Vincent Doyeux, Yann Guyot, Vincent Chabannes, Christophe Prudhomme, and Mourad Ismail. Simulation of two-fluid flows using a finite element/level set method. application to bubbles and vesicle dynamics. *Journal of Computational and Applied Mathematics*, 246:251–259, 2013.

[22] Björn Engquist, Anna-Karin Tornberg, and Richard Tsai. Discretization of Dirac delta functions in level set methods. *Journal of Computational Physics*, 207(1):28–51, 2005.

[23] Prerna Gera and David Salac. The three-dimensional jump conditions for the stokes equations with discontinuous viscosity, singular forces and an incompressible interface. 2013.

[24] Wolfgang Helfrich. Elastic properties of lipid bilayers: theory and possible experiments. *Zeitschrift für Naturforschung. Teil C: Biochemie, Biophysik, Biologie, Virologie*, 28(11):693, 1973.

[25] W F Hu, M C Lai, and Y N Young. Numerical simulation for a leaky dielectric drop under DC electric field. 2014 SIAM Annual Meeting.

[26] Aldo Jesorka and Owe Orwar. Liposomes: technologies and analytical applications. *Annual review of analytical chemistry (Palo Alto, Calif.)*, 1:801–32, January 2008.

[27] Vasiliy Kantsler and Victor Steinberg. Orientation and dynamics of a vesicle in tank-treading motion in shear flow. *Physical review letters*, 95(25):258101, 2005.

[28] Vasiliy Kantsler and Victor Steinberg. Transition to tumbling and two regimes of tumbling motion of a vesicle in shear flow. *Physical review letters*, 96(3):036001, 2006.

[29] Badr Kaoui, Jens Harting, and Chaouqi Misbah. Two-dimensional vesicle dynamics under shear flow: Effect of confinement. *Physical Review E*, 83(6):066319, June 2011.

[30] Charles R Keese, Joachim Wegener, Sarah R Walker, and Ivar Giaever. Electrical wound-healing assay for cells in vitro. *Proceedings of the National Academy of Sciences of the United States of America*, 101(6):1554–1559, 2004.

[31] K Kinosita, I Ashikawa, N Saita, H Yoshimura, H Itoh, K Nagayama, and a Ikegami. Electroporation of cell membrane visualized under a pulsed-laser fluorescence microscope. *Biophysical journal*, 53(6):1015–9, 1988.

[32] Ebrahim M Kolahdouz and David Salac. A semi-implicit gradient augmented level set method. *SIAM Journal on Scientific Computing*, 35(1):231–254, 2013.

[33] Ebrahim M Kolahdouz and David Salac. A numerical model for the transmembrane voltage of vesicles. *Applied Mathematics Letters*, 2014.

[34] Wanda Krassowska and Petar D Filev. Modeling electroporation in a single cell. *Biophysical journal*, 92(2):404–17, January 2007.

[35] A. Kumar. Isotropic Finite-Differences. *Journal of Computational Physics*, 201(1):109–118, November 2004.

[36] Aymen Laadhari, Pierre Saramito, and Chaouqi Misbah. Vesicle tumbling inhibited by inertia. *Physics of Fluids (1994-present)*, 24(3):031901, 2012.

[37] Aymen Laadhari, Pierre Saramito, and Chaouqi Misbah. Computing the dynamics of biomembranes by combining conservative level set and adaptive finite element methods. *Journal of Computational Physics*, 263:328–352, 2014.

[38] Ming-Chih Lai and Hsiao-Chieh Tseng. A simple implementation of the immersed interface methods for Stokes flows with singular forces. *Computers & Fluids*, 37(2):99–106, February 2008.

[39] Danilo D Lasic. The mechanism of vesicle formation. *Biochemical Journal*, 256(1):1, 1988.

[40] D.V. Le, B.C. Khoo, and J. Peraire. An immersed interface method for viscous incompressible flows involving rigid and flexible boundaries. *Journal of Computational Physics*, 220(1):109–138, December 2006.

[41] VV Lebedev, KS Turitsyn, and SS Vergeles. Dynamics of nearly spherical vesicles in an external flow. *Physical review letters*, 99(21):218101, 2007.

[42] Randall J. LeVeque and Zhilin Li. The immersed interface method for elliptic equations with discontinuous coefficients and singular sources. *SIAM Journal on Numerical Analysis*, 31(4):1019–1044, 1994.

[43] Randall J. LeVeque and Zhilin Li. Immersed interface methods for Stokes flow with elastic boundaries or surface tension. *SIAM Journal on Scientific Computing*, 18(3):709–735, May 1997.

[44] Zhilin Li. A fast iterative algorithm for elliptic interface problems. *SIAM Journal on Numerical Analysis*, 35(1):230–254, February 1998.

[45] Zhilin Li. An overview of the immersed interface method and its applications. *Taiwanese journal of mathematics*, 7(1):pp–1, 2003.

[46] Zhilin Li, Kazufumi Ito, and Ming-Chih Lai. An augmented approach for Stokes equations with a discontinuous viscosity and singular forces. *Computers & Fluids*, 36(3):622–635, 2007.

[47] Zhilin Li and Ming-Chih Lai. The immersed interface method for the navier–stokes equations with singular forces. *Journal of Computational Physics*, 171(2):822–842, August 2001.

[48] C. Macdonald and S. Ruuth. The Implicit Closest Point Method for the Numerical Solution of Partial Differential Equations on Surfaces. *SIAM Journal on Scientific Computing*, 31(6):4330–4350, 2010.

[49] Colin B Macdonald and Steven J Ruuth. The implicit closest point method for the numerical solution of partial differential equations on surfaces. *SIAM Journal on Scientific Computing*, 31(6):4330–4350, 2009.

[50] ColinB. Macdonald and StevenJ. Ruuth. Level Set Equations on Surfaces via the Closest Point Method. *Journal of Scientific Computing*, 35(2-3):219–240, 2008.

[51] M A Mader, V Vitkova, M Abkarian, A Viallat, and T Podgorski. Dynamics of viscous vesicles in shear flow. *The European Physical Journal E: Soft Matter and Biological Physics*, 19(4):389–397, 2006.

[52] Emmanuel Maitre, Chaouqi Misbah, Philippe Peyla, and Annie Raoult. Comparison between advected-field and level-set methods in the study of vesicle dynamics. *Physica D: Nonlinear Phenomena*, 241(13):1146–1157, 2012.

[53] Lane C McConnell, Michael J Miksis, and Petia M Vlahovska. Vesicle electrohydrodynamics in dc electric fields. *IMA Journal of Applied Mathematics*, 78(4):797–817, 2013.

[54] JR Melcher and GI Taylor. Electrohydrodynamics: a review of the role of interfacial shear stresses. *Annual Review of Fluid Mechanics*, 1(1):111–146, 1969.

[55] Ling Miao, Udo Seifert, Michael Wortis, and Hans-Günther Döbereiner. Budding transitions of fluid-bilayer vesicles: the effect of area-difference elasticity. *Physical Review E*, 49(6):5389, 1994.

[56] Jean-Christophe Nave, Rodolfo Ruben Rosales, and Benjamin Seibold. A Gradient-Augmented Level Set Method With an Optimally Local, Coherent Advection Scheme. *Journal of Computational Physics*, 229(10):3802–3827, May 2010.

[57] D Needham and RM Hochmuth. Electro-mechanical permeabilization of lipid vesicles. Role of membrane tension and compressibility. *Biophysical journal*, 55(5):1001–1009, 1989.

[58] Eberhard Neumann, M Schaefer-Ridder, Y Wang, and PH Hofschneider. Gene transfer into mouse lyoma cells by electroporation in high electric fields. *The EMBO journal*, 1(7):841, 1982.

[59] Vincent Noireaux and Albert Libchaber. A vesicle bioreactor as a step toward an artificial cell assembly. *Proceedings of the National Academy of Sciences of the United States of America*, 101(51):17669–74, December 2004.

[60] S Osher and S Chakravathy. Very High Order Accurate TVD Schemes. *IMA Volumes in Mathematics and Its Applications*, pages 229–274, 1986.

[61] S Osher and JA Sethian. Fronts Propagating with Curvature-Dependent Speed - Algorithms Based on Hamilton-Jacobi Formulations. *Journal of Computational Physics*, 79(1):12–49, NOV 1988.

[62] Stanley Osher and Ronald P. Fedkiw. *Level set methods and dynamic implicit surfaces*, volume 153; 153. Springer, New York, 2003.

[63] Michael Patra and Mikko Karttunen. Stencils with Isotropic Discretization Error for Differential Operators. *Numerical Methods for Partial Differential Equations*, 01794, 2006.

[64] D Peng. A PDE-Based Fast Local Level Set Method. *Journal of Computational Physics*, 155(2):410–438, November 1999.

[65] Charles S Peskin. The immersed boundary method. *Acta numerica*, 11:479–517, 2002.

[66] Karin a Riske and Rumiana Dimova. Electro-deformation and poration of giant vesicles viewed with high temporal resolution. *Biophysical journal*, 88(2):1143–55, February 2005.

[67] Karin a Riske and Rumiana Dimova. Electric pulses induce cylindrical deformations on giant vesicles in salt solutions. *Biophysical journal*, 91(5):1778–86, September 2006.

[68] Boris Rubinsky, Gary Onik, and Paul Mikus. Irreversible electroporation: a new ablation modality–clinical implications. *Technology in cancer research & treatment*, 6(1):37–48, February 2007.

[69] Yousef Saad. *Iterative Methods for Sparse Linear Systems, Second Edition.* Society for Industrial and Applied Mathematics, 2 edition, April 2003.

[70] Mohamed M Sadik, Jianbo Li, Jerry W Shan, David I Shreiber, and Hao Lin. Vesicle deformation and poration under strong dc electric fields. *Physical Review E*, 83(6):066316, 2011.

[71] D Salac and Ebrahim M Kolahdouz. A mass-preserving projection method for incompressible multiphase flows. In Preparation.

[72] D Salac and M Miksis. A level set projection model of lipid vesicles in general flows. *Journal of Computational Physics*, 230(22):8192–8215, 2011.

[73] David Salac and Wei Lu. A Local Semi-Implicit Level-Set Method for Interface Motion. *Journal of Scientific Computing*, 35(2-3):330–349, February 2008.

[74] David Salac and Michael J Miksis. Reynolds number effects on lipid vesicles. *Journal of Fluid Mechanics*, 711:122–146, 2012.

[75] Paul F Salipante and Petia M Vlahovska. Vesicle deformation in dc electric pulses. *Soft matter*, 2014.

[76] Paul Salipnate. *Electrohydrodynamics of simple and complex interfaces.* Ph.d dissertation, Brown University, 2013.

[77] D A Saville. Electrohydrodynamics: The Taylor-Melcher leaky dielectric model. *Annual Review of Fluid Mechanics*, 29(1962):27–64, 1997.

[78] Jonathan T Schwalbe, Petia M Vlahovska, and Michael J Miksis. Lipid membrane instability driven by capacitive charging. *Physics of Fluids (1994-present)*, 23(4):041701, 2011.

[79] Jonathan T Schwalbe, Petia M Vlahovska, and Michael J Miksis. Vesicle electrohydrodynamics. *Physical Review E*, 83(4):046309, 2011.

[80] Benjamin Seibold, Jean-Christophe Nave, and Rodolfo Ruben Rosales. Jet Schemes For Advection Problems. *Discrete and Continuous Dynamical Systems - Series B*, 17(4):1229–1259, JUN 2012.

[81] Benjamin Seibold, Rodolfo Ruben Rosales, and Jean-Christophe Nave. Jet schemes for advection problems. *Discrete and Continuous Dynamical Systems - Series B*, 17(4):1229 – 1259, 2012.

[82] Udo Seifert. Configurations of fluid membranes and vesicles. *Advances in Physics*, 46(1):13–137, 1997.

[83] Udo Seifert, Karin Berndl, and Reinhard Lipowsky. Shape transformations of vesicles: Phase diagram for spontaneous-curvature and bilayer-coupling models. *Physical Review A*, 44(2):1182, 1991.

[84] Jacopo Seiwert, Michael J Miksis, and Petia M Vlahovska. Stability of biomimetic membranes in dc electric fields. *Journal of Fluid Mechanics*, 706:58–70, 2012.

[85] Jacopo Seiwert and Petia M. Vlahovska. Instability of a fluctuating membrane driven by an ac electric field. *Physical Review E*, 87(2):022713, February 2013.

[86] Johan Skog, Tom Würdinger, Sjoerd van Rijn, Dimphna H Meijer, Laura Gainche, William T Curry, Bob S Carter, Anna M Krichevsky, and Xandra O Breakefield. Glioblastoma microvesicles transport rna and proteins that promote tumour growth and provide diagnostic biomarkers. *Nature cell biology*, 10(12):1470–1476, 2008.

[87] Peter Smereka. Semi-implicit level set methods for curvature and surface diffusion motion. *Journal of Scientific Computing*, 19:439–456, 2003.

[88] Peter Smereka. The numerical approximation of a delta function with application to level set methods. *Journal of Computational Physics*, 211(1):77–90, 2006.

[89] M. Sussman and E. Fatemi. An Efficient, Interface-Preserving Level Set Redistancing Algorithm and Its Application to Interfacial Incompressible Fluid Flow. *SIAM Journal on Scientific Computing*, 20(4):1165–1191, 1999.

[90] John D Towers. A convergence rate theorem for finite difference approximations to delta functions. *Journal of Computational Physics*, 227(13):6591–6597, 2008.

[91] Tian Y Tsong. Electroporation of cell membranes. *Biophysical journal*, 60(2):297–306, 1991.

[92] H. A. van der Vorst. Bi-CGSTAB: A Fast and Smoothly Converging Variant of Bi-CG for the Solution of Nonsymmetric Linear Systems. *SIAM Journal on Scientific Computing*, 13(2):631–644, 1992.

[93] Shravan K Veerapaneni, Denis Gueyffier, Denis Zorin, and George Biros. A boundary integral method for simulating the dynamics of inextensible vesicles suspended in a viscous fluid in 2d. *Journal of Computational Physics*, 228(7):2334–2353, 2009.

[94] Shravan K. Veerapaneni, Abtin Rahimian, George Biros, and Denis Zorin. A fast algorithm for simulating vesicle flows in three dimensions. *Journal of Computational Physics*, 230(14):5610–5634, June 2011.

[95] Petia M Vlahovska and Ruben Serral Gracia. Dynamics of a viscous vesicle in linear flows. *Physical Review E*, 75(1):016313, 2007.

[96] Petia M Vlahovska, Ruben Serral Gracia, Said Aranda-Espinoza, and Rumiana Dimova. Electrohydrodynamic model of vesicle deformation in alternating electric fields. *Biophysical journal*, 96(12):4789–4803, 2009.

[97] Petia M. Vlahovska, Thomas Podgorski, and Chaouqi Misbah. Vesicles and red blood cells in flow: From individual dynamics to rheology. *Comptes Rendus Physique*, 10(8):775–789, November 2009.

[98] Zhenyu Wang, Ning Hu, Li-Hsien Yeh, Xiaolin Zheng, Jun Yang, Sang W Joo, and Shizhi Qian. Electroformation and electrofusion of giant vesicles in a microfluidic device. *Colloids and Surfaces B: Biointerfaces*, 110:81–87, 2013.

[99] Chunlin Wu and Xuecheng Tai. A level set formulation of geodesic curvature flow on simplicial surfaces. *Visualization and Computer Graphics, IEEE Transactions on*, 16(4):647–662, 2010.

[100] Sheng Xu and Z. Jane Wang. Systematic derivation of jump conditions for the immersed interface method in three-dimensional flow simulation. *SIAM Journal on Scientific Computing*, 27(6):1948–1980, January 2006.

[101] Alireza Yazdani and Prosenjit Bagchi. Three-dimensional numerical simulation of vesicle dynamics using a front-tracking method. *Physical Review E*, 85(5):056308, May 2012.

[102] Qingshan Yang Yugang Tang, Ying Liu. Liquid crystal model of vesicle deformation in alternating electric fields. *Theoretical and Applied Mechanics Letters*, 3(5):11, 2013.

[103] Norman J Zabusky, Enrico Segre, Julien Deschamps, Vasiliy Kantsler, and Victor Steinberg. Dynamics of vesicles in shear and rotational flows: Modal dynamics and phase diagram. *Physics of Fluids (1994-present)*, 23(4):041905, 2011.

[104] Hong Zhao and Eric S. G. Shaqfeh. The dynamics of a vesicle in simple shear flow. *Journal of Fluid Mechanics*, 674:578–604, March 2011.

[105] Falko Ziebert and David Lacoste. A planar lipid bilayer in an electric field: membrane instability, flow field and electrical impedance. *Advances in planar lipid bilayers and liposomes*, 14:63–95, 2011.